

GEOLOGY AND PETROLOGY OF SOUTH SISTER VOLCANO,  
HIGH CASCADE RANGE, OREGON

by

JAMES GREGORY CLARK

A DISSERTATION

Presented to the Department of Geology  
and the Graduate School of the University of Oregon  
in partial fulfillment of the requirements  
for the degree of  
Doctor of Philosophy

March 1983

VITA

NAME OF AUTHOR: James Gregory Clark

PLACE OF BIRTH: Youngstown, Ohio

DATE OF BIRTH: October 30, 1948

UNDERGRADUATE AND GRADUATE SCHOOLS ATTENDED:

Miami University, Oxford, Ohio  
Ohio State University, Columbus  
Oregon State University, Corvallis  
University of Oregon

DEGREES AWARDED:

Bachelor of Science, 1971, Ohio State University  
Master of Science, 1975, Oregon State University

AREAS OF SPECIAL INTEREST:

Igneous Petrology and Geochemistry  
Volcanology  
Economic Geology

PROFESSIONAL EXPERIENCE:

Research Assistant in Oceanography, Oregon State  
University, Corvallis, 1972-1976

Assistant Geologist, Noranda Exploration, Inc.,  
Reno, Nevada, 1976

Geologist, Cominco American, Inc., Spokane, Washington,  
1977

Graduate Teaching Fellow, University of Oregon,  
Eugene, 1976-1981

Geologist, Molycorp, Inc., Englewood, Colorado,  
1980-present

PUBLICATIONS:

Isaacson, L. B., Heinrichs, D. F., Blakely, R., and  
Clark, J. G., 1973. Paleosecular variation at  
Easter Island. EOS Abstract, 54, 1074.

Clark, J. G. and Dymond, J., 1974. Age, chemistry,  
and tectonic significance of Easter Island. EOS  
Abstract, 55(4), 300.

Clark, J. G., 1975. K-Ar ages and major element  
chemistry of volcanic rocks from Easter and Sala y  
Gomez Islands and their bearing on the origin of  
the Sala y Gomez Ridge. Geol. Soc. Amer. Ann.  
Mtg. 1975, Abstracts with Programs, 7(7), 1029.

Clark, J. G. and Dymond, J. R., 1977. Geochronology  
and petrochemistry of Easter and Sala y Gomez  
Islands: Implications for the origin of the Sala y  
Gomez Ridge. J. Volcan. Geotherm. Res., 2, 20-48.

Clark, J. G., 1983. Petrogenesis of divergent magmas  
at South Sister volcano, High Cascade range, Oregon.  
Geol. Soc. Amer. Abstracts with Programs (in press).

## ACKNOWLEDGMENTS

I am indebted to Dr. Alexander McBirney for providing patience, encouragement, and analytical support throughout the course of this work. Critical reviews of the manuscript by Dr. Alexander McBirney and Dr. Mark Reed improved greatly its form and content. I wish also to acknowledge the other members of my committee, Dr. Brian Baker and Dr. Gordon Goles, for their comments and suggestions.

Financial assistance for field and analytical work was supplied by Dr. Alexander McBirney, the Mazamas, the Oregon Department of Geology and Mineral Industries, Sigma Xi, and a GSA Penrose Research Grant. E. A. Mathez of the University of Washington provided microprobe time and instruction, and Christine McBirney did the atomic absorption analyses. I would like to thank Ben Ross, Bill Niemi, Matt Davidson, Barbara John, and Simon for assistance in the field, and N. S. MacLeod of the U.S.G.S. for providing color air photos of the South Sister area. Through the years a variety of students helped to make graduate school seem less like Jim Hoover's cheese grater, in particular, Jim, Ellie, Carl, Jim, Helen, Shirley, Cal,

Melanie, Marcia, and Cheri. Thanks and appreciation are also extended to Cal Barnes for numerous discussions of the fine points of Oregon geology, and to Carl Hering and Henry Rainier, with whom many of the ideas presented in this manuscript were initiated and developed. I also owe large debts of gratitude to W. Glen Zinn of Molycorp, Inc. for his patience, understanding and perspective during the last two years, to Allen Mayhew for the drafting, and to Lou Ann Gilbert-Molling and Sonja Scott for the typing. Finally, the greatest appreciation is owed to Kristina for her Herculean patience and support, and to Jessie, whose birth accelerated the completion of this work.

## TABLE OF CONTENTS

Chapter	Page
1. GEOLOGY OF SOUTH SISTER VOLCANO.....	1
Introduction.....	1
Regional Geology and Structure.....	4
South Sister Volcano.....	8
2. CHEMICAL VARIATION.....	40
Major and Trace Element Abundance Patterns.....	40
Mineral Composition and Variation.....	56
3. PETROLOGY AND GEOCHEMISTRY.....	65
Phase Relations.....	65
Trace Element Variations.....	70
Fractional Crystallization.....	73
Partial Melting.....	98
4. ORIGIN OF THE DIVERGENT SUITE.....	110
Geology and Petrography.....	111
Major and Trace Element Geochemistry.....	130
Petrogenesis.....	132
Basalt-Crust Interaction.....	154
Physical Model.....	169
APPENDICES	
A. Modal Abundances of Phenocrysts in Lavas from South Sister Volcano.....	188
B. Bulk Rock Chemical Analyses.....	190
C. Mineral Analyses.....	206
REFERENCES.....	225

## LIST OF TABLES

Table	Page
1. Ranges of Distribution Coefficients.....	75
2. $Ps_{ad}$ Major and Trace Element Fractionation Models.....	80
3. $Ps_{ba}$ Major and Trace Element Fractionation Models.....	88
4. Temperature, Density and Viscosity of Representative Samples from Main ( $Ps_{ad}$ ) and Summit ( $Ps_{ba}$ ) Lavas.....	96
5. Physical Parameters Calculated for Post- glacial Rhyodacitic Lavas ( $Ho_{rda}$ ).....	143
6. Major and Trace Element Fractionation Models - Silicic Rocks.....	145
7. Magma Mixing - Fractionation Model for Basaltic Rocks from Le Conte Crater.....	164
8. Calculated Physical and Fluid Dynamic Properties for the $Ho_{rda}$ Magma Chamber.....	178

## LIST OF FIGURES

Figure	Page
1. Regional geology.....	2
2. Generalized map of High Cascade and Basin and Range structures.....	6
3. Location map of the study area.....	9
4. Cognate xenolith in Ps <sub>rda</sub> lava.....	17
5. Post-glacial basalt (Ho <sub>bs</sub> ) from Le Conte Crater.....	30
6. Post-glacial rhyodacite (Ho <sub>rda</sub> ).....	35
7. Time-Volume-Composition relationships at Souty Sister volcano.....	38
8. Harker variation diagrams for lavas from the South Sister volcanic complex.....	41
9. AFM diagram for lavas from the South Sister volcanic complex.....	45
10. Total alkalis versus silica.....	47
11. Al <sub>2</sub> O <sub>3</sub> versus normative plagioclase composition.....	48
12. Peacock index for lavas from the South Sister volcanic complex.....	48
13. FeO*/FeO* + MgO versus SiO <sub>2</sub> .....	50
14. Trace element variations versus D.I.....	51

Figure	Page
15. Variation of Ni and Cr with D.I. in basaltic rocks from the South Sister volcanic complex.....	55
16. Generalized paragenetic sequences for the South Sister volcanic suite.....	57
17. Mafic phenocryst compositions in lavas from the South Sister volcanic complex.....	58
18. Plagioclase phenocryst compositions in lavas from the South Sister volcanic complex.....	62
19. $XO \cdot R_2O_3 - YO - ZO_2$ projection from clinopyroxene.....	67
20. Th versus Rb for lavas from the South Sister volcanic complex.....	72
21. Compositional variation of main cone lavas ( $Ps_{ad}$ ) with stratigraphic position....	77
22. Compositional variation of summit cone lavas ( $Ps_{ba}$ ) with stratigraphic position....	84
23. Trace element concentration trends versus F.....	92
24. Rb versus Ni in main ( $Ps_{ad}$ ) and summit ( $Ps_{ba}$ ) cone lavas from South Sister.....	100
25. H/M versus H element plots.....	104
26. Geological sketch map of South Sister volcano and vicinity.....	112
27. Post-glacial Le Conte basalt ( $HO_{bS}$ ).....	121
28. Post-glacial Le Conte basalts ( $HO_{bS}$ ).....	123
29. South Sister rhyodacites.....	127
30. Phenocryst compositions from divergent lavas.....	131

Figure	Page
31. T-f <sub>O<sub>2</sub></sub> relations of post-glacial rhyodacites...	138
32. H/M versus H diagrams for divergent suites from South Sister and Crater Lake.....	149
33. Fused granitic xenolith from the Collier basalt flow.....	159
34. Proportions of resorbed and total plagioclase in the Le Conte basalt flow versus distance from the vent.....	162
35. Schematic representation of the sequential geological evolution of the South Sister volcanic complex.....	171
36. Schematic view of a compositionally- stratified magma chamber.....	180
37. Variations of trace element ratios in post-glacial rhyodacitic domes with structural height.....	186

LIST OF PLATES

Plate

1. Geologic map of South Sister Volcano..... in pocket
2. Sample Location Overlay..... in pocket

## CHAPTER 1

### GEOLOGY OF SOUTH SISTER VOLCANO

#### Introduction

Quaternary volcanic activity in the High Cascade range is concentrated along a north to north-northeast trending belt extending from Mt. Lassen in the south to Mt. Garibaldi in the north (Figure 1). Most of the major composite cones were formed within the last 700,000 years, and all have been attributed to continental margin volcanism above a descending lithospheric slab. Despite these common features, major differences exist among the major volcanic centers with regard to chemical composition, compositional range and temporal evolution. The Quaternary High Cascade volcanoes of Oregon erupted onto a platform of voluminous basaltic lava flows. The cones are of three general types: 1) those composed of uniform flows of basaltic andesite, such as North Sister and Mt. Thielsen, 2) those composed of uniform andesites, and which have erupted minor volumes of dacite as activity declined (Mt. Hood, Mt. Jefferson), and 3) those composed predominantly of silicic andesite

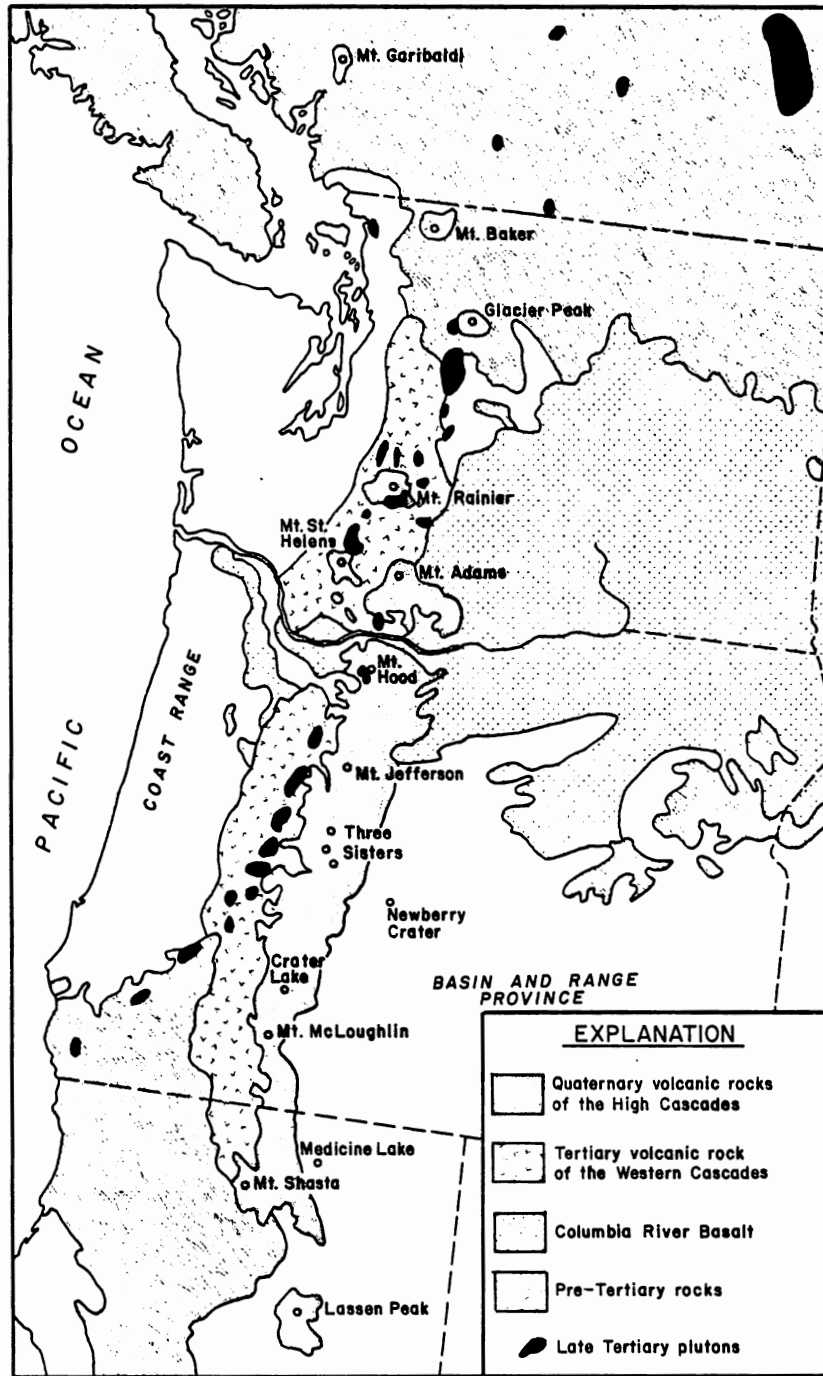


Figure 1. Regional geology (after McBirney, 1968).

and dacite, and which have erupted late-stage magmas of strongly contrasting composition (Mazama, South Sister). McBirney (1968) termed the first two suites coherent and the latter divergent.

The full range of Quaternary calc-alkaline volcano types is found in the Three Sisters Wilderness in the central Oregon High Cascade range. Four major volcanoes and numerous subsidiary volcanic centers exhibit a complete assortment of lava flows, domes and pyroclastic deposits. Large composite volcanoes of both the coherent and divergent types precede monogenetic satellite volcanoes which can show strong compositional gradients within single lava flows. In the Three Sisters area, as elsewhere in the High Cascade Range, divergent-type volcanoes, such as the South Sister tend to be younger and to erupt magmas of more silicic composition than do volcanoes of the coherent type. This observation suggests that the early eruptive history of the host volcano may play a significant part in the development of the late-stage divergence. The following study documents the multi-stage geological and petrological evolution of the South Sister volcanic complex, with specific emphasis on the origin of the divergent, basalt-rhyodacite suite.

## Regional Geology and Structure

### Cascade Range

High Cascade volcanism represents only the latest major episode in a Cascade Range volcanic history that began in Eocene time. This history has been summarized by McBirney (1978). Significant calc-alkaline volcanism began from widespread Western Cascade vents during the early Oligocene as predominantly andesitic and rhyolitic eruptions (Peck et al, 1964). With the discharge of voluminous andesitic lavas of the Sardine formation (Thayer, 1937) during the Middle Miocene, the volcanic centers were concentrated into a linear belt, just west of and slightly oblique to the present High Cascade Axis (Figure 1). The transition to more fundamentally basaltic activity began during the Pliocene with the eruption of the Outerson formation (Thayer, 1937). Overlying the Outerson formation is a thick sequence of basaltic lavas from numerous, coalescing Plio-Pleistocene shield volcanoes which form the base of the High Cascades. The shield lavas are capped by the quasi-linear belt of Quaternary andesitic High Cascade volcanoes. Rocks from the High Cascades were deposited unconformably upon those of the Western Cascades. Volcanoes of the southern and northern ends of the chain erupted onto a pre-Tertiary plutonic-metamorphic basement, but the central part of the Cascade Range may be underlain by thinner,

oceanic-type crust (Hamilton and Meyers, 1966; Johnson and Couch, 1970). The crustal differences along the chain may be reflected in the preponderance of basalts relative to differentiated rocks in the central part of the range.

The dominant structures in the High Cascades strike approximately north-south (Figure 2). This trend is apparent in the alignment of major cones along the chain, in the alignment of cinder cones and minor vents adjacent to major centers, and in the orientation of the boundary faults of the subsiding graben into which the High Cascade volcanoes erupted. The normal faults of the High Cascade graben have as much as 600 meters of vertical displacement (E. M. Taylor, personal communication, 1979), and are best documented by steep gravity gradients west of the High Cascade axis (Pitts and Couch, 1978). The eastern margin of the graben fault occurs as the Hood River and Green Ridge faults, north-northwest of Sisters, Oregon (Allen and Beau-lieu, 1976). The eastern graben fault is not recognized south of the town of Sisters, apparently owing to the disturbance of Cascade structures by intersecting faults of the Basin and Range province.

#### Basin and Range Province

The Basin and Range province of southeastern Oregon abuts the eastern margin of the High Cascade chain from near Black Butte south across the California border

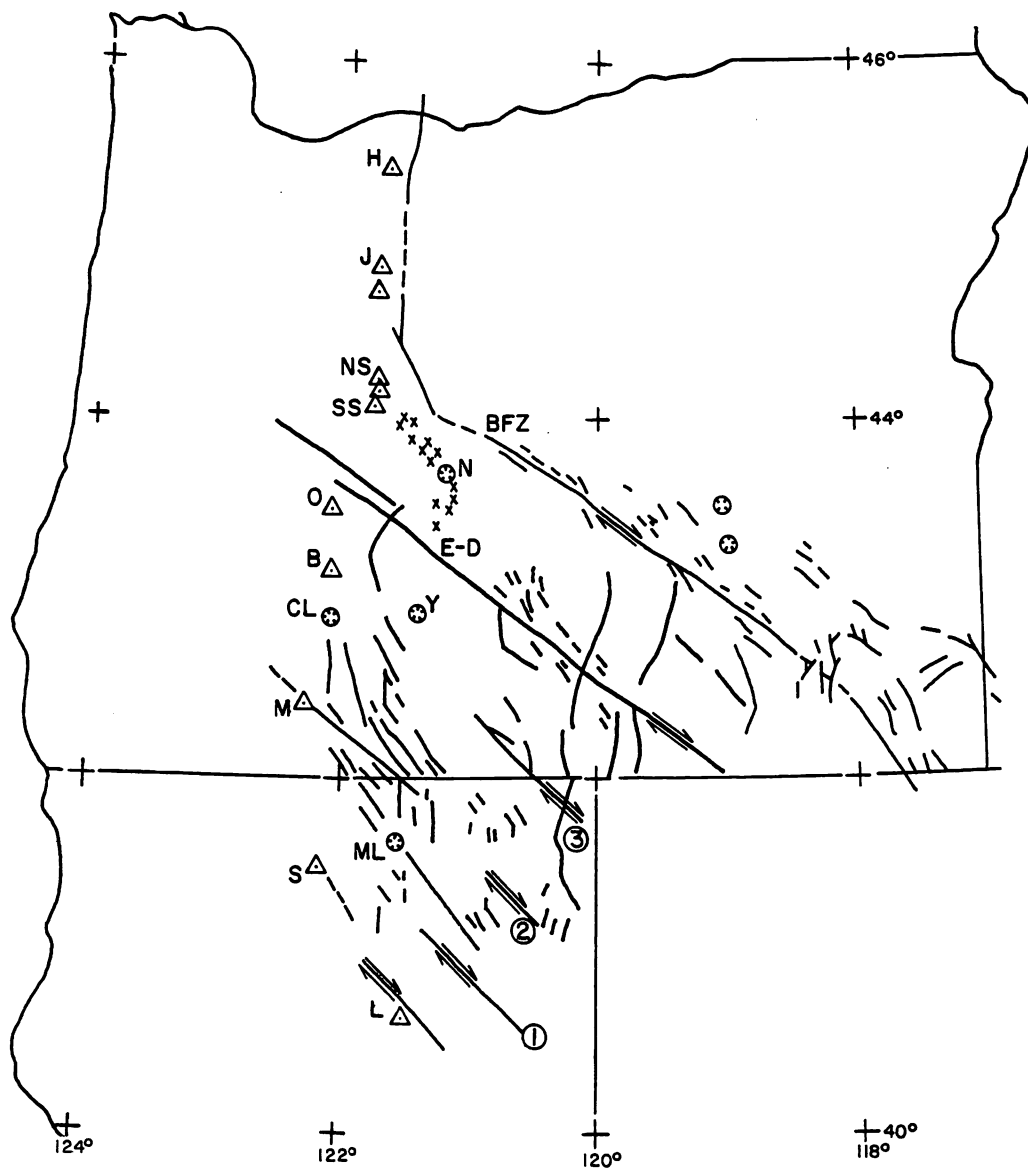


Figure 2. Generalized map of High Cascade and Basin and Range structures. Data are from Hering (1981), Allen and Beaulieu (1976), and Pease (1969). Symbols are: H, Mt. Hood; J, Mt. Jefferson; NS, North Sister; SS, South Sister; D, Diamond Peak; B, Mt. Bailey; CL, Crater Lake; M, Mt. McLaughlin; S, Mt. Shasta; L, Mt. Lassen; N, Newberry Caldera; Y, Yamsay Mtn.; ML, Medicine Lake Caldera; BFZ, Brothers Fault Zone; E-D, Eugene-Denio Fault Zone; ①, Eagle Lake Fault; ②, Likely Fault; ③, Fandango-Sprague Fault; \* Cinder cones near Newberry Caldera.

(Figure 2). The province is marked by conjugate N10-30°E and N20-40°W normal and oblique-slip faults which reflect general east-west extension (Stewart, 1978). Faulting in the Basin and Range province in Oregon may have begun as early as the Late Miocene (Wells, 1975; Larson, 1965) and was accompanied by bimodal basaltic and rhyolitic volcanic activity. Near the western margin of the Basin and Range are situated large shield complexes that erupted high-alumina basalt and dacitic to rhyolitic differentiated rocks. Some shield complexes are capped by summit calderas, such as those of Newberry (Higgins, 1973; Macleod et al, 1980), Yamsay Mountain (Hering, 1981) and Medicine Lake (Anderson, 1941; Mertzman, 1977) centers of Pliocene to Recent age. Eastward from the western margin of the Basin and Range, the basaltic rocks tend to be more alkaline, rather than high-alumina basalts (Waters, 1962).

The northwest-trending faults in the Basin and Range province of southeastern Oregon form discontinuous, "en echelon" segments which define extensive fault zones (Lawrence, 1976). Conspicuous among these zones are the Brothers fault zone, the Eugene-Denio fault zone, and the Mt. McLaughlin lineament (Figure 2; Lawrence, 1976), all of which may have right-lateral strike-slip movement.

### South Sister Volcano

South Sister volcano straddles the boundary between the Willamette and Deschutes National Forests in the central Oregon High Cascade Range. It is located near the southern limit of the Three Sisters Wilderness, about 25 miles west of Bend, Oregon (Figure 3).

Geologic mapping and sampling were done during parts of the summers of 1978 and 1979. The mapping was done on U. S. Forest Service aerial photos at a scale of 1:12000 and transferred to a base map compiled from the Three Sisters SE and Broken Top SW 7½' U. S. Geological Survey quadrangle maps.

Previous geological investigations of the Three Sisters area were those of Williams (1944), Taylor (1978), and Wozniak and Taylor (1981). They showed that the imposing composite cone of South Sister was constructed during Pleistocene time of basaltic-andesitic to rhyodacitic flows, domes and very minor pyroclastic material which overlie voluminous basaltic lavas erupted from several coalescing shield volcanoes. Post-glacial flows and cinder cones of olivine basalt ring the southern base of the volcano, and were followed closely in time by extrusion of rhyodacitic domes, flows and attendant pumice eruptions. The geology of South Sister volcano is summarized in Plate 1.

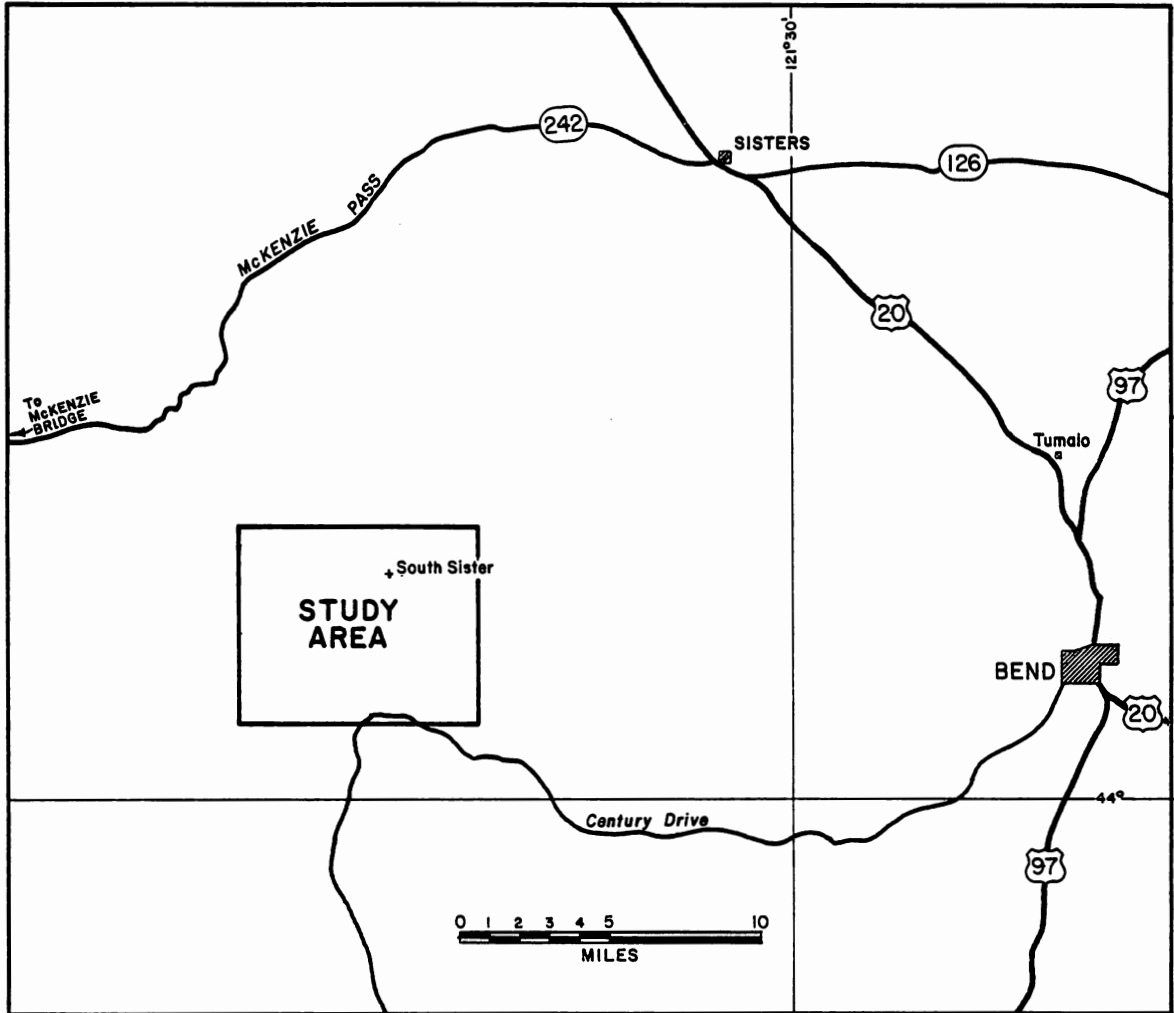


Figure 3. Location map of the study area.

Basaltic Shield ( $Ps_{bs}$ )

South Sister is underlain by more than 650 meters of lava flows of basaltic-andesite erupted from at least two and perhaps as many as four different centers. Rocks with reversed magnetic polarity in the vicinity of the Sphinx Butte center are indicated by a large negative aeromagnetic anomaly centered just southwest of the Sphinx (Couch et al, 1978). However, several flows exposed in the north wall of Separation Creek Canyon have northerly dips and normal polarity. Their probable source was the Sphinx Butte vent, and they intertongue with basaltic lavas from the Husband. It seems likely that activity at Sphinx Butte volcano spanned the Brunhes-Matuyama paleomagnetic boundary, about 690,000 years ago. Basaltic lavas from the Wife and Husband may also extend beneath the main cone of South Sister, and all appear to be normally polarized. Williams (1944) presented evidence for a fourth shield center to the east; he noted that westerly dips on lava flows between Mesa Creek and James Creek, below an elevation of 2100 meters, may indicate a source vent now buried beneath the main cone of South Sister. The contact between lavas derived from the older shield centers (e.g. the Husband or subsidiary vents at Proxy and Substitute Points) and those from the postulated "ancestral South Sister" may lie along James Creek, between about 1300 and 1950 meters of elevation.

Where James Creek runs parallel to the Separation Creek trail, basaltic lava flows on opposite sides cannot be correlated across the creek. The flows south of the creek have filled an earlier glaciated valley, and have in turn been eroded during glaciation.

Lava flows from all the shield centers are lithologically similar olivine basalt and basaltic andesite. The best exposures are in the steep walls of Separation Creek canyon, where a 600-meter section of lavas has been excavated by glacial erosion. The flows range from one to ten meters in thickness, and most are between two and five meters thick. A few thin volcanic mudflows interbedded with the lavas contain angular clasts of basalt and rounded glacial erratics up to thirty centimeters in diameter set in a fine, reddish-brown to yellow matrix.

Late Pleistocene glaciation has exposed the interiors of capping cones and central conduits of both the Sphinx Butte and Wife centers. The central conduit of the Sphinx dominates the steep canyon wall south of the intersection between James and Mesa Creeks (Plate 1). The cone was constructed of interbedded scoria and lapilli tuff, and remnants are exposed at the top of the canyon wall. It apparently occupied a central crater at the summit of Sphinx Butte volcano (Williams, 1944). Numerous dikes cut the cone and may have fed the surrounding basaltic lava flows.

The Wife erupted basaltic to andesitic lavas and tephra. Its cone was constructed predominantly of red and yellow lapilli tuff and scoria cut by andesitic dikes ranging from 10 cm to 5 m in thickness.

As shield activity declined, andesitic lavas, possibly from the main cone of South Sister, erupted essentially contemporaneously with the basaltic shield lavas. Andesitic lavas interfinger with shield basalts south of Indian Holes and Separation Creek.

The basalts and basaltic andesites of the pre-cone shield are ubiquitously olivine-phyric. Olivine phenocrysts ( $Fo_{85-80}$ ) are subhedral to resorbed, 1 to 2 mm in length, and make up 3 to 10 volume percent of the rock. The olivines commonly contain inclusions of glass and/or cubic to octahedral, red-brown spinel. The glass inclusions may represent trapped magmatic liquid (Anderson, 1976), and rare pyroxene and plagioclase inclusions in the olivines can probably be attributed to post-entrapment crystallization of this trapped melt. Olivine phenocrysts in more evolved shield lavas have rims of granular pyroxene. Plagioclase phenocrysts and microphenocrysts make up less than 5% of the rock and are generally less than 1 mm in length. The plagioclase crystals display weak patchy to concentric compositional zonation and range from  $An_{75}$  to  $An_{55}$  in composition. Trapped melt inclusions are also common in

plagioclase phenocrysts, and have minor post-entrapment pyroxene. Plagioclase and olivine phenocrysts occasionally form glomerocrysts. The fine-grained, holocrystalline to glassy groundmass includes plagioclase, pyroxene (augite ± pigeonite ?), olivine, titanomagnetite, apatite and brown glass. Most shield lavas are porphyritic and vesicular, but a wide variety of groundmass textures may be found. Observed textures include pilotaxitic, intergranular with minor intersertal glass, intersertal with minor intergranular pyroxene and olivine, intergranular with minor ophitic pyroxene, and rarely, seriate plagioclase laths. Groundmass plagioclase laths range from  $An_{55}$  to  $An_{45}$  in composition and commonly contain tiny needles of apatite. Groundmass glass may contain minute, acicular crystals of clinopyroxene.

#### Early Rhyodacites ( $Ps_{rda}$ )

Apart from occasional andesitic flows which interfinger with the shield basalts west of South Sister, the earliest main cone activity was dominated by copious rhyodacitic lavas and attendant pumice. Rhyodacitic lavas were discharged along north-northeast striking fractures extending from Devil's Hill and Kaleetan Butte on the south to as far north as Demaris Lake. Devil's Hill (7100') caps a thick plateau of rhyodacitic lava which is exposed down to an elevation of 5450 feet (1760 meters) without intervening

andesite. Rhyodacite also makes up a large part of the southern and eastern slopes of the South Sister, as well as a prominent plateau, about 4.5 km northeast of Carver Lake, constructed of at least 120 meters of rhyodacitic lava. South of Lewis Glacier on South Sister, rhyodacitic lava crops out up to an elevation of approximately 8600 feet. Though initial eruptions were spread along the north-northeast-striking fracture system, it seems likely that, at a slightly later time, the eruptive centers were localized beneath South Sister. Rhyodacitic lava probably underlies the southeastern third of the volcano.

Minor pre-cone andesites interfinger with shield basalts west of South Sister. However, the contact relations on the cone itself, between the rhyodacites ( $Ps_{rda}$ ) and the andesites and dacites making up the bulk of the cone ( $Ps_{ad}$ ), suggest that most of the rhyodacitic lava was erupted prior to the advent of significant andesitic activity. Andesitic dikes cut glaciated rhyodacite on the south and southeast flanks of the volcano, and on the elongate ridge north of Devil's Hill. The remnant of a thick rhyodacitic dome is exposed at the base of the east flank of South Sister, just west of Green Lake basin. The dome is more than 100 meters thick and was inundated by andesitic and dacitic lavas ( $Ps_{ad}$ ) of the main cone before being excavated by glacial erosion. Only at higher levels on the south flank of the

cone do sporadic  $Ps_{ad}$  lavas interfinger with the rhyodacites. These exposures appear to represent a transitional phase from rhyodacitic to predominantly andesitic activity.

The early rhyodacitic lavas occur as pale-gray pumiceous, medium-gray lithoidal, and dense, black obsidian varieties, some of which have contorted flow banding. The glassy obsidian is somewhat perlitic and commonly contains pink to gray spherulites and/or lithophysae up to several centimeters in diameter. Lavas similar to the early rhyodacites are also exposed at Obsidian Cliffs, northwest of Middle Sister.

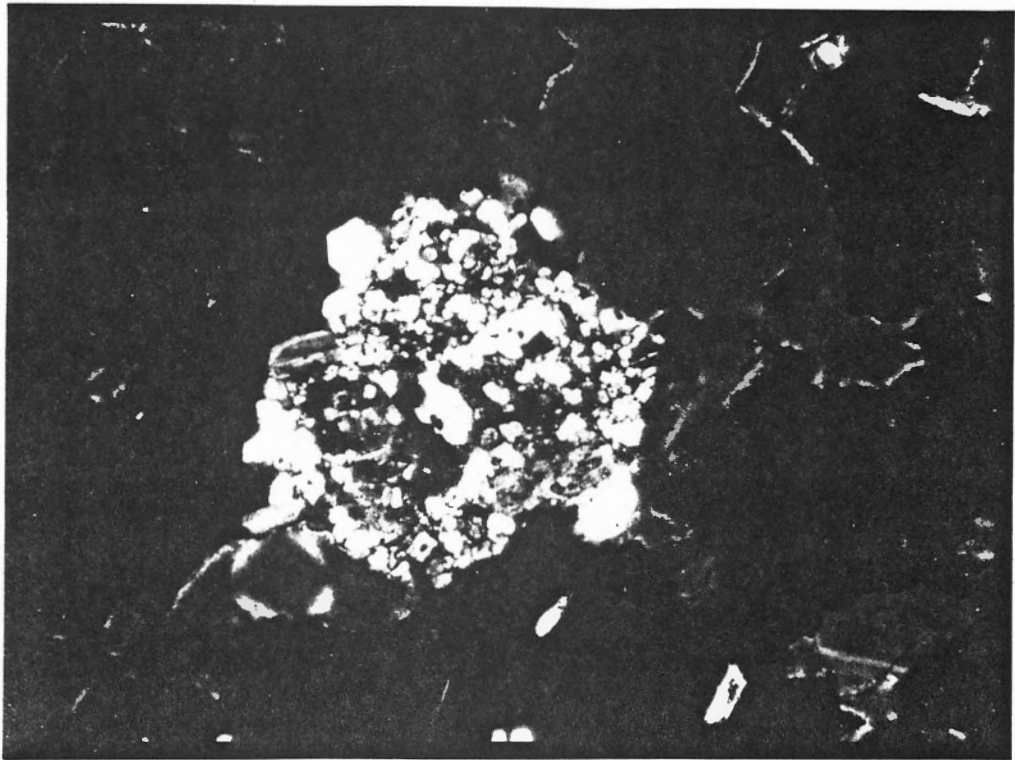
The early rhyodacitic lavas contain less than 15 volume percent phenocrysts of plagioclase, orthopyroxene, Fe-Ti oxides, and rare hornblende set in a glassy to microcrystalline groundmass. Modal abundances are given in Appendix A. Plagioclase phenocrysts and microphenocrysts are euhedral to subhedral laths up to 3 mm in length. Zonation is oscillatory-normal or patchy, and the total compositional range is from  $An_{35}$  to  $An_{22}$ . Most zonation is in phenocrysts, while microphenocrysts are relatively unzoned. Inclusions of clear glass, pyroxene, magnetite, or apatite are rare. Marginal resorption of plagioclase phenocrysts is not common. Orthopyroxene microphenocrysts are euhedral to subhedral and less than 0.5 mm in diameter. They range

in composition from  $En_{65}$  to  $En_{55}$  and commonly have thin, reversely-zoned rims. The orthopyroxene microphenocrysts are generally dispersed throughout the matrix, but also occur as monomineralic glomerocrysts, or in conjunction with plagioclase and/or magnetite. Magnetite and ilmenite are present as microphenocrysts less than 0.2 mm in length. Rare zircon occurs as a microphenocryst phase and is less than 0.15 mm in length. Holocrystalline, cognate xenoliths occur as rare polycrystalline aggregates of plagioclase, orthopyroxene, and magnetite up to 1 cm in diameter. One inclusion has a peculiar "hornfelsic" texture (Figure 4). The xenoliths may represent the products of crystallization at the walls of the magma chamber. The dark, glassy groundmass shows contorted flow banding and radial, spherulitic devitrification, and contains microlites of orthopyroxene and sodic plagioclase. Vesicles are commonly filled with a silica mineral, perhaps cristobalite.

#### Main Cone Andesites and Dacites ( $Ps_{ad}$ )

Stubby, viscous flows and plug domes of andesite and dacite make up the bulk of the main cone of South Sister.  $Ps_{ad}$  lavas cover almost the entire western flank of the cone below an elevation of 8800 feet (Plate 1). On the western side of the volcano the contact with the underlying shield coincides approximately with a sharp discontinuity in slope

Figure 4. Cognate xenolith in Ps<sub>rda</sub> lava.



angle, from the 3 to 4° westerly slopes characteristic of the flank of the shield to the 13 to 24° slope of the lower part of the main cone. Andesitic lavas from South Sister have also filled parts of the glaciated valley between Sphinx Butte and Honey Lakes, down to an elevation of about 5000 feet. On the eastern side of the volcano the distribution of the Ps<sub>ad</sub> lavas is controlled in part by the glaciated topography of earlier units erupted from the Broken Top complex (Taylor, 1978). Andesitic lavas from South Sister extend nearly to Park Meadow, east of South Sister and north of Broken Top. Above Park Meadow, South Sister andesites overlie basaltic andesites from Broken Top. Similar Ps<sub>ad</sub> lavas were traced two kilometers north of Red Meadow, where they disappear beneath a cover of glacial debris. Volcanic activity may have been interrupted during the construction of the main cone. Below an elevation of approximately 7600 feet, flows from both the Ps<sub>rda</sub> and Ps<sub>ad</sub> units have been polished and striated by Late Pleistocene glaciers. Above that level andesitic and dacitic flows cap ridges which radiate from the summit. The ridges have been carved into greater relief by glacial erosion, but their blocky, spired flow tops could not have been completely overridden by ice. The 7600 foot level is also marked by an abrupt change in slope angle, from an average of about 22° in the lower part to 29° in the upper part. The bound-

ary between completely and incompletely glaciated lavas suggests that the rate of glacial denudation exceeded that of volcanic deposition midway during construction of the main cone.

Few  $Ps_{ad}$  flows originated at summit vents. Glacial erosion has exposed  $Ps_{ad}$  dikes which probably fed flank eruptions. On the flanks of the cone proper, these dikes radiate from the summit, but those cutting rhyodacitic lavas north of Devil's Hill strike N50E to N60E.

The andesitic and dacitic lavas of the main cone range from 10 to 30 meters thick. Rubbly flow bottoms pass upward into the thin, platy jointing characteristic of siliceous andesites. The varied orientation of the joints may result from complex cooling patterns associated with eruption beneath snow or ice. The interiors of thick flows are massive, but unglaciated flow tops are rubbly with irregular spires. Ramp structures and zones of internal autobrecciation are well-exposed in some of the thicker flows. While minor laharic breccias are interbedded with andesitic and dacitic flows, the most striking feature of the main cone  $Ps_{ad}$  flow sequences is the scarcity of accompanying pyroclastic material. A few thin flows of porphyritic basalt are interbedded with the volumetrically dominant sequence of andesitic and dacitic flows.

The andesitic and dacitic lavas of the  $Ps_{ad}$  unit are

similar in appearance and cannot be differentiated in the field. They are medium to dark gray porphyritic rocks containing up to 30% phenocrysts of plagioclase, orthopyroxene, clinopyroxene and Fe-Ti oxides set in a vitrophyric to finely holocrystalline groundmass. Modal abundances are given in Appendix A. Plagioclase phenocrysts and microphenocrysts are euhedral to subhedral, up to 4 mm in length, and range in composition from  $An_{57}$  to  $An_{39}$ . Plagioclase microphenocrysts are relatively unzoned, but the phenocrysts display moderate to strong, concentric oscillatory-normal and patchy zonation. Some have inclusions of glass, apatite, and, more rarely, pyroxene and magnetite. The glassy inclusions probably represent trapped magmatic liquid, while the apatite, pyroxene, and magnetite are most likely the products of post-entrapment crystallization. Rare, small plagioclase phenocrysts have corroded margins and are charged with abundant glass inclusions. Orthopyroxene ( $En_{70-85}$ ) is the next most abundant phenocryst and occurs as euhedral to subhedral crystals up to 1 mm in length. The orthopyroxene phenocrysts also exhibit rare inclusions of magnetite, glass and apatite. Augite phenocrysts are euhedral to subhedral, up to 1.5 mm in diameter, and commonly twinned. Magnetite or glass inclusions in augite are rare. Magnetite and, more rarely, ilmenite form subhedral microphenocrysts up to 0.3 mm in

length. Glomerocrystic aggregates of phenocrysts include the following assemblages:

Plagioclase + orthopyroxene + clinopyroxene +  
magnetite ± brown glass

Orthopyroxene + magnetite

Plagioclase + orthopyroxene + magnetite

Fine plagioclase and apatite, and lesser magnetite and pyroxene join the brown glass in the groundmass.

The porphyritic basalts interbedded with the andesitic and dacitic flows are similar petrographically to those which make up the summit cone and are described in the following section.

#### Basaltic Andesites of the Summit Cones (Ps<sub>ba</sub>)

The main cone of South Sister is capped by two summit cones of basaltic andesite lava flows and tephra. The earliest flows were from vents just east of the summit and built a cone similar in structure and composition to the present summit cone. The older summit cone has since been ravaged by Prouty and Lewis Glaciers, so that its internal structure is well-exposed. Like the younger summit cone, the older one consists of layers of red, black and yellow basaltic scoria, cinders and lapilli tuff interbedded with thin lava flows and cut by dikes. Two cols west of the older cone appear to mark the contact between products

erupted from the older cone and those from the present summit cone. Volcanic activity must have shifted abruptly to the west, for there is no evidence that both cones were active simultaneously.

Fragmental ejecta and lava flows from the younger cone buried much of the older lavas. The outer flanks of the cone are mantled by a veneer of cinders, scoria, and volcanic bombs up to a meter or more in diameter. The 400 meter wide summit crater is rimmed with a crust of agglutinate and holds a small lake. According to Williams (1944) two small depressions on the crater floor mark the surface expression of the central conduits. Within the crater and above the bergschrunds of Lewis, Clark, Lost Creek, and Prouty Glaciers, thick flows of dark, scoriaeous lava are interbedded with tephra and cut by thin dikes. Within the Clark Glacier section sampled for this study a dacitic lava flow similar to those forming the bulk of the main cone is interbedded with the basaltic andesites.

The lava flows of basaltic andesite are two to ten meters thick and have rubbly bases, massive centers, and scoriaceous tops. They are porphyritic, vesicular and contain up to 20% phenocrysts of plagioclase, olivine, clinopyroxene and, rarely, orthopyroxene in a fine-grained groundmass with pilotaxitic, intergranular, or intersertal textures. Modal abundances are given in Appendix A. Pla-

gioclase occurs as euhedral to subhedral phenocrysts and microphenocrysts ranging from 0.3 mm to 3.0 mm in length and from  $An_{53}$  to  $An_{39}$  in composition. The size range is nearly seriate from groundmass to phenocryst plagioclase. Two basic types of plagioclase phenocrysts are present. The first,  $Pl_I$ , shows extensive resorption and abundant glass inclusions, while the second,  $Pl_{II}$ , shows no resorption or glass inclusions. Plagioclase phenocrysts with inclusion zones ( $Pl_I$ ) are gradational between two extremes. The  $Pl_{Ia}$  variety has a central, inclusion-rich core with fine, granular brown glass, pyroxene, and plagioclase. The core is surrounded by a clear rim which can be either more calcic, or more sodic, than the interior. The  $Pl_{Ib}$  variety is similar to  $Pl_{Ia}$  except that the inclusion-rich zone encloses a clear, irregular core. The  $Pl_{II}$  plagioclase phenocrysts tend to be smaller than their  $Pl_I$  counterparts, and they have weak normal zoning. Inclusions of apatite needles are common in all plagioclase types. Olivine ( $Fo_{80-70}$ ) phenocrysts are up to 0.6 mm in diameter. They often contain inclusions of red-brown chromian spinel, and all show a reaction relationship with the liquid to produce thin coronas of fine, granular orthopyroxene. The clinopyroxene is augite and occurs as euhedral to subhedral crystals to 0.7 mm in diameter. The augite phenocrysts rarely contain tiny inclusions of glass, magnetite or

apatite. Orthopyroxene is present as a stable microphenocryst phase in the more evolved basaltic andesites. The crystals are euhedral and reach 0.4 mm in length. The orthopyroxene is commonly found with magnetite, and both minerals apparently came on a liquidus at the same time.

Basalts interbedded with the main cone andesites and dacites are texturally similar to the summit cone flows, but have more anorthite-rich plagioclase ( $An_{82-76}$ ) and more magnesian clinopyroxene than do basaltic andesites of the summit cone.

#### Post-glacial Basalts ( $Ho_{bs}$ )

Shortly after the basaltic andesite activity at the summit of South Sister, flank eruptions of olivine basalt were discharged from flank vents at and near Le Conte Crater. Taylor (1978) mapped coeval basalts and basaltic andesites which erupted from vents southwest of Todd Lake and at the northern base of Mt. Bachelor. All of the basaltic vents are peripheral to later rhyodacitic activity, which took place several thousand years after the decline of basaltic volcanism.

Le Conte Crater stands adjacent to Rock Mesa, southwest of South Sister. It rises about 100 meters above Wickiup Plain and is about 500 meters in diameter. An almost perfect conical shape attests to its youth. The cone is

constructed of red and black basaltic scoria that peeks from beneath a veneer of ejecta from the Rock Mesa vent in only a few places. It is capped by a bowl-shaped crater, and a small ridge protrudes from its southern flank.

Williams (1944) suggested that the ridge may be a buried basaltic lava flow erupted from a tear in the flank of the cone. The basaltic flows erupted from Le Conte Crater, and perhaps from vents now hidden beneath the Rock Mesa rhyodacite, can be traced northwest to the Mesa Creek valley down to an elevation of 5500 feet. Other flows surround Kokostick Butte and apparently dammed Devil's Lake before terminating northeast of Elk Lake. Along Wickiup Plain the basalts are covered by a veneer of pumice and other debris from the later eruption of the Rock Mesa flow. Likewise, Le Conte Crater is also covered by a layer of pumice and admixed blocks of andesite, basalt, and glacial debris torn from the conduit of the Rock Mesa vent.

Cayuse Crater lies at the base of Broken Top volcano, southeast of South Sister. The cone, about 200 meters high and 800 meters in diameter, has been breached on its southwestern side by two lobes of lava, the longest of which is buried at its terminus beneath the alluvium of Sparks Lake Basin, just south of Century Drive (Taylor, 1978). Two small scoria cones are aligned along a fracture extending N40W from Cayuse Crater. A small basaltic lava flow issued

from the most northwesterly cone.

The Le Conte and Cayuse basalts are probably roughly equivalent in age. Taylor (1978) noted that the Cayuse flows are overlain by both Mazama Ash and pumice from the chain of rhyodacitic domes on the south flank of South Sister. Thus the age of eruption of these basalts can be bracketed between 12,000 years ago, the age of the Late Pleistocene glacial episode, and 6600 years ago, the age of the climactic eruption of Mount Mazama.

Lavas from the Cayuse and Le Conte vents consist of blocky to aa flows in which the scoriaceous, rubbly top grades rapidly downward, first into highly vesicular lava and then to less vesicular, dark gray to black olivine basalt in the interior. The flows are from two to five meters thick at their termini.

The olivine basalts from the Cayuse flows contain phenocrysts of olivine in a pilotaxitic network of plagioclase laths, granular pyroxene and olivine, and intersertal glass. Olivine phenocrysts and microphenocrysts ( $\text{Fo}_{85}$ ) are subhedral and up to 1.5 mm in length. The olivines occur as discrete phenocrysts and aggregates of from two to four crystals. Inclusions of cubic, red-brown, chromian spinel are common. Several olivine phenocrysts show marginal resorption and thin, granular reaction coronas of pyroxene. Groundmass plagioclase may range to microphenocryst size (0.5 mm) and ranges in composition between  $\text{An}_{70}$  and  $\text{An}_{60}$ .

Quench crystals of magnetite occur within the intersertal glass pools.

The olivine and plagioclase-phyric basalts from Le Conte Crater were studied in more detail because of their location immediately adjacent to vents which discharged rhyodacitic magmas. The olivine and plagioclase phenocrysts are set in a fine, hyalopilitic to intergranular-intersertal groundmass of plagioclase laths ( $An_{65}$ ), black glass, and olivine. Fasciculate groundmass textures are rarely present. Olivine ranges in composition from  $Fo_{85}$  to  $Fo_{80}$  and occurs as euhedral to subhedral phenocrysts and microphenocrysts up to 3 mm in length. The olivines are found either as discrete phenocrysts or in clots of up to four crystals. Inclusions of cubic, red-brown, chromian spinel are common. Plagioclase inclusions are rare and appear to have crystallized from liquid which migrated along cracks in the grains. A few of the larger olivine phenocrysts are strongly resorbed, with thin rims of granular pyroxene and glass.

Plagioclase phenocrysts and microphenocrysts are up to 2.5 mm in length, and fall into two major categories. The first type,  $Pl_I$ , has a subhedral, clear rim of approximately  $An_{65-70}$  composition, and an inner zone charged with inclusions of vermiform glass, calcic plagioclase, and, occasionally, pyroxene. The inner zone may or may not have

an irregular, clear core of more sodic plagioclase ( $An_{55}$ ) (Figure 5). The second type,  $Pl_{II}$ , occurs as euhedral to subhedral microphenocrysts and lesser phenocrysts up to 1.5 mm in length. The  $Pl_{II}$  grains are clear and rarely show concentric compositional zonation from  $An_{70}$  to  $An_{65}$ . Minor marginal resorption is occasionally present.

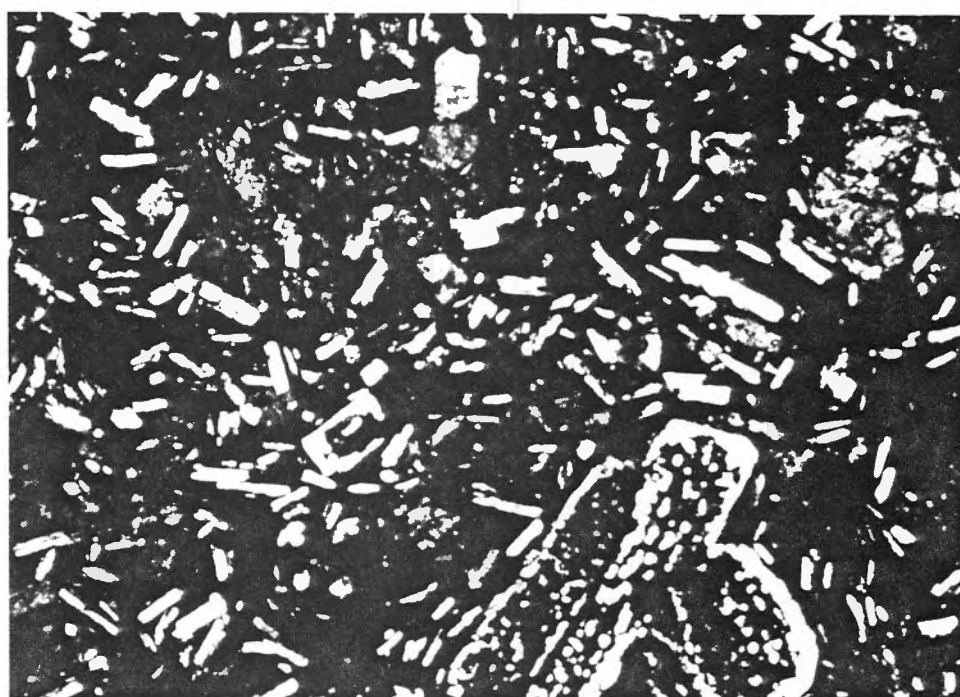
Sample SS-192, taken from a Le Conte flow adjacent to Devil's Lake, contains strongly resorbed quartz xenocrysts up to 1.5 mm in diameter. The quartz xenocrysts are enclosed by partial to complete reaction coronas of granular clinopyroxene and brown glass.

Modal phenocryst abundances for the Le Conte and Cayuse basalts are given in Appendix A. The modal abundance data for the Le Conte basalts show smooth variations of phenocryst proportions and abundances as a function of distance from the vent. The significance of these observations is discussed in a later section.

#### Post-glacial Rhyodacites ( $Ho_{rda}$ )

Several thousand years after basaltic activity ended in this area, small volumes of explosive pumice burst from vents now buried beneath Rock Mesa. The initial eruptions took place between 2300 and 1900 years ago (Taylor, 1978) and were precursors to the large, viscous Rock Mesa flow of pumiceous obsidian. The pumice eruption brought with it

Figure 5. Post-glacial basalt ( $\text{Ho}_{\text{bs}}$ ) from  
Le Conte Crater.



large quantities of fragmental material torn from the underlying bedrock. Accidental ejecta include blocks of andesite, basalt and glacial erratics.

The Rock Mesa flow is a mass of rhyodacitic obsidian 80 to 100 meters thick at its edge. Expanding gas frothed parts of the flow into light gray pumice. The steep sides of the flow are ringed with talus, and its top is marked by arcuate pressure ridges. The domical mound atop the northeastern part of the flow formed as the lava became too viscous to flow and accumulated directly over the vent. The top of the flow is a rubbly mass of shattered glass and pumice topped by irregular, jagged spires of obsidian.

Rock  
MESA

A series of rhyodacitic domes and flows extends down from about the 7850 foot level on the south flank of South Sister and ends abruptly at Century Drive, near Devil's Lake. This chain of domes developed shortly after the eruption of Rock Mesa (Taylor, 1978) along an approximately north-south-striking fracture, just east of Devil's Hill. The fracture is exposed between two domes east of Devil's Hill. The chain displays a slight change in strike, from N3W south of Goose Creek, to N10W north of Goose Creek. The flows are somewhat more voluminous in the section north of the creek. The largest and uppermost flow in this section is the Newberry flow. Pumice expelled during the eruption of the Newberry flow built a rampart west of the

DOME  
CHAIN

?

flow which buried an older, glaciated rhyodacitic dome (Ps<sub>rda</sub>). Part of the rampart is constructed of well-bedded, poorly-sorted, and partly-welded air fall pumice lapilli. Most of the domes congealed directly over their vents. Both these domes and the Rock Mesa flow are lithologically similar. Flow banding is common, and spherulitic structures have developed, though they are not nearly so common as in the older rhyodacite unit (Ps<sub>rda</sub>).

The post-glacial rhyodacites (Ho<sub>rda</sub>) contain up to 20% phenocrysts and microphenocrysts of plagioclase and orthopyroxene, plus minor Fe-Ti oxides and rare amphibole and zircon microphenocrysts, set in a vitrophyric to pumiceous groundmass of dark brown glass and plagioclase micro-lites. Modal abundances are listed in Appendix A.

As in the Holocene basalts of Le Conte Crater, the plagioclase phenocrysts in the post-glacial rhyodacites fall into two groups. Most of the microphenocrysts (<0.5 mm length) and some of the phenocrysts (0.5 mm to 3 mm in length) occur as euhedral to subhedral crystals with minor concentric-normal zonation and a narrow compositional range between An<sub>43</sub> and An<sub>36</sub>. The second group consists primarily of plagioclase phenocrysts which show moderate to strong resorption and abundant glass inclusions. The orientation of the glass inclusions within the plagioclase phenocrysts appears to be crystallographically

controlled, and the inclusions are of either brown or clear glass. Phenocrysts of the second textural variety exhibit a much broader range of anorthite contents than do the first group, from  $An_{52}$  to  $An_{34}$ . Normal and reverse concentric zonation and patchy zonation are common. Resorption intensity ranges from minor rounding of the phenocrysts to strongly fritted phenocrysts (Figure 6). Similar textures in plagioclase phenocrysts have been interpreted by Larsen and Switzer (1939) and Sigurdsson (1968) to represent partial melting of crystals derived from the source rocks. Both plagioclase phenocryst types contain common inclusions of euhedral, rod-like apatite, and rare inclusions of magnetite or orthopyroxene. Orthopyroxene occurs as euhedral microphenocrysts up to 1 mm diameter. These microphenocrysts exhibit a narrow compositional range ( $En_{63}$  to  $En_{59}$ ) and commonly have narrow, reversely-zoned rims. The orthopyroxenes contain rare inclusions of apatite or magnetite, and a single orthopyroxene microphenocryst was observed to encompass a tiny, rounded inclusion of pleochroic amphibole. Minor magnetite and ilmenite microphenocrysts are euhedral to subhedral and less than 0.2 mm in length. The magnetite is also found as inclusions in orthopyroxene or, more rarely, in plagioclase. Hornblende is present occasionally as either corroded microphenocrysts to 0.3 mm in length, euhedral micropheno-

Figure 6. Post-glacial rhyodacite (Hordá). Note euhedral and resorbed plagioclase phenocrysts and microphenocrysts of orthopyroxene and magnetite.

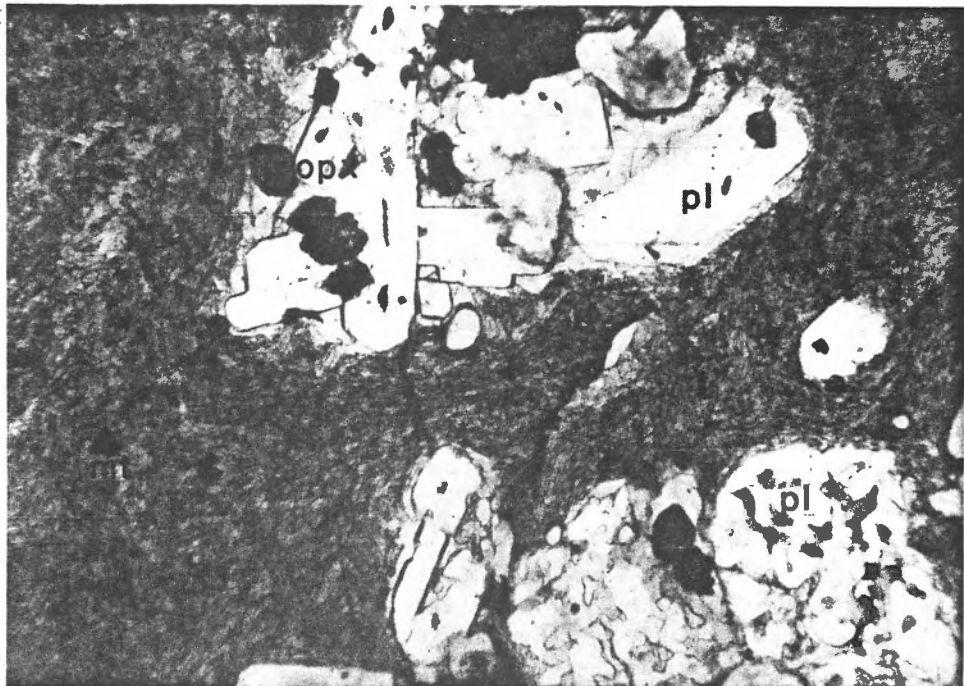
a. Crossed nicols.

b. Plane-polarized light.

a.



b.



crysts less than 0.1 mm in length (quench crystallization?), or as an inclusion in orthopyroxene (one example observed). Euhedral zircon microphenocrysts are rare and up to 0.15 mm in length. Glomerocrysts are common and consist of the following assemblages:

Plagioclase

Plagioclase + Orthopyroxene + Magnetite

Orthopyroxene + Magnetite

Orthopyroxene

The groundmass is predominantly dark brown to black glass with microlitic needles of plagioclase and, less commonly, fine granular orthopyroxene. Magnetite dusting is sometimes present within the glass. Shearing and folding are common within the flow bands.

#### Time-Volume-Composition Relationships

The temporal petrological evolution of South Sister volcano is summarized in Figure 7. The stages in the construction of the volcanic complex are: I - Shield basalts ( $Ps_{bs}$ ); II - Early rhyodacites ( $Ps_{rda}$ ); III - Main cone andesites and dacites ( $Ps_{ad}$ ); IV - Summit basaltic andesites ( $Ps_{ba}$ ); V - Post-glacial basalts ( $Ho_{bs}$ ); and VI - Post-glacial rhyodacites ( $Ho_{rda}$ ). The volumes of lavas erupted in each unit were estimated from the available field data, and only for the map area in Plate 1. The

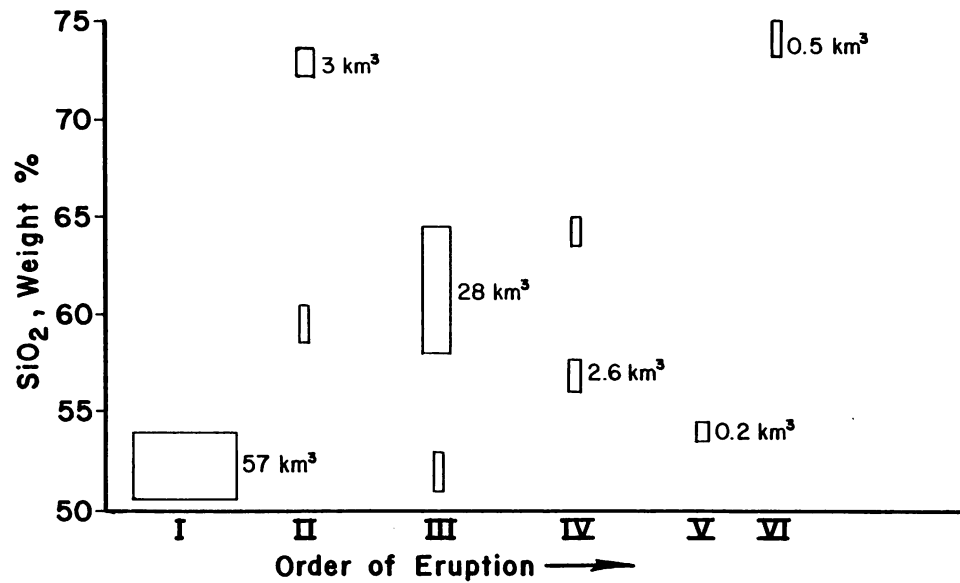
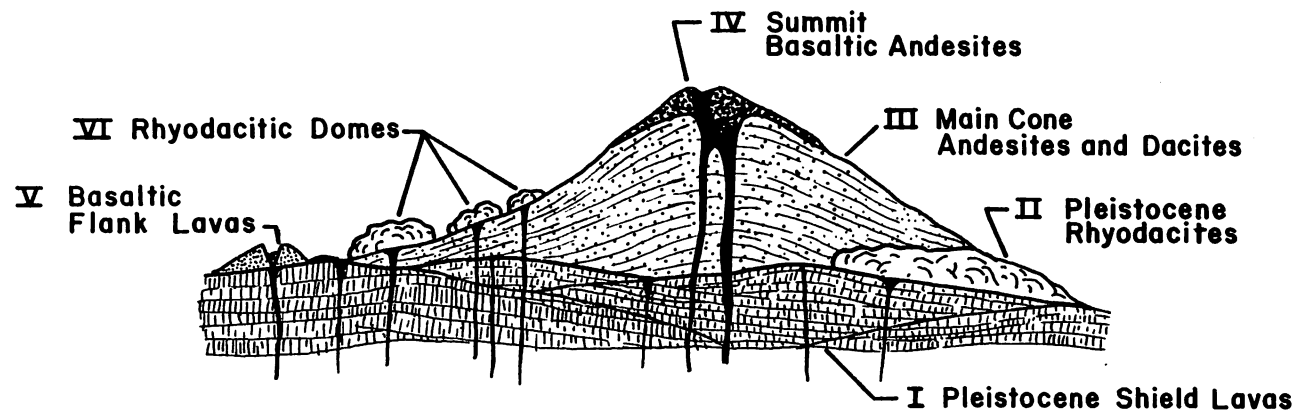


Figure 7. Time-Volume-Composition Relationships at South Sister volcano.

total proportion of shield basalt to later eruptive rocks is believed to be higher, both in the Three Sisters area and in the Oregon High Cascade range. The total volume of post-glacial basaltic rocks would also be substantially larger if the area surrounding Mt. Bachelor were considered. Rough calculations indicate that the volume of post-glacial basalts and basaltic andesites, within a 10 km radius from the Newberry rhyodacitic flow on the south flank of South Sister, is in excess of 30 km<sup>3</sup>. As documented in Figure 7, minor andesitic and dacitic lavas were erupted during stages II and IV, and minor basalts were erupted during stage III. The most notable features of the data are:

1. The large change in the composition of the dominant eruptive products between stages I and II (from basalt to rhyodacite).
2. The smooth temporal transition during construction of the main cone from rhyodacite to basaltic andesite (stages II, III and IV).
3. The bimodality of composition in the post-glacial eruptive rocks (stages V and VI).
4. A compositional gap in the overall rock suite. No samples occur within the compositional range of from 65% SiO<sub>2</sub> to 72% SiO<sub>2</sub>.

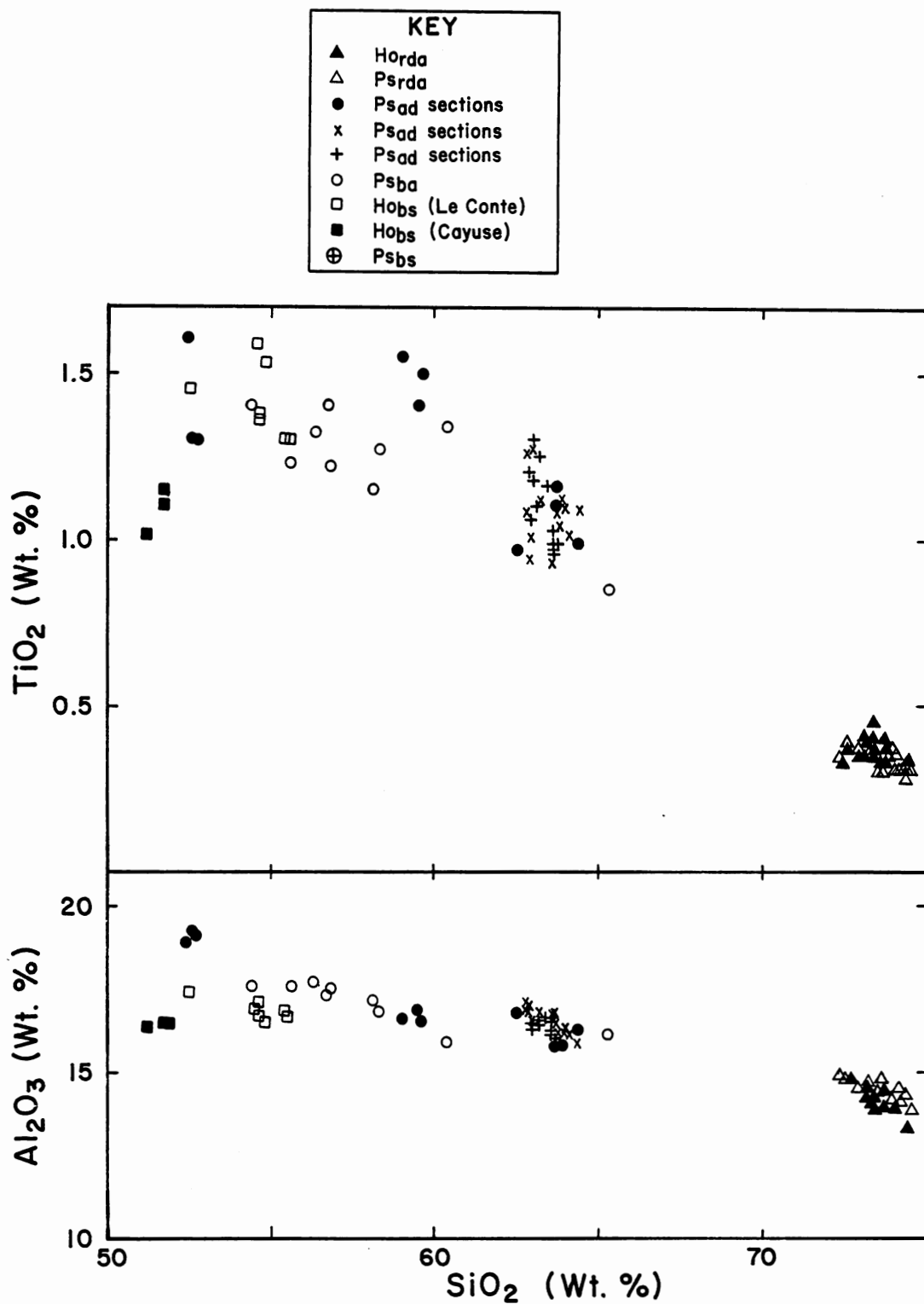
## CHAPTER 2

## CHEMICAL VARIATION

Major and Trace Element Abundance Patterns

Major and trace element abundances were obtained for 107 samples from South Sister volcano. The samples are representative of the major eruptive units, and include three stratigraphically-controlled sections from the main cone (Ps<sub>ad</sub>) and one from the summit cone (Ps<sub>ba</sub>). Sample locations are plotted on Plate 2. Ten major elements and the trace elements, Rb, Sr, Ba, Ni, and Cr were analyzed by atomic absorption spectrophotometry (AAS). Rb, Sr, and Zr were analyzed by X-ray fluorescence (XRF). Rb and Sr analyses by XRF and AA were in close agreement. The major element analyses used in this chapter have been recalculated to 100% on a volatile-free basis to minimize effects of hydration and oxidation. All Fe was calculated as FeO (FeO\*). Analyses are tabulated in Appendix B.

Silica covariance (Harker) diagrams for volcanic rocks from South Sister are plotted in Figure 8. The analyses exhibit the smooth, linear variations typical of calc-



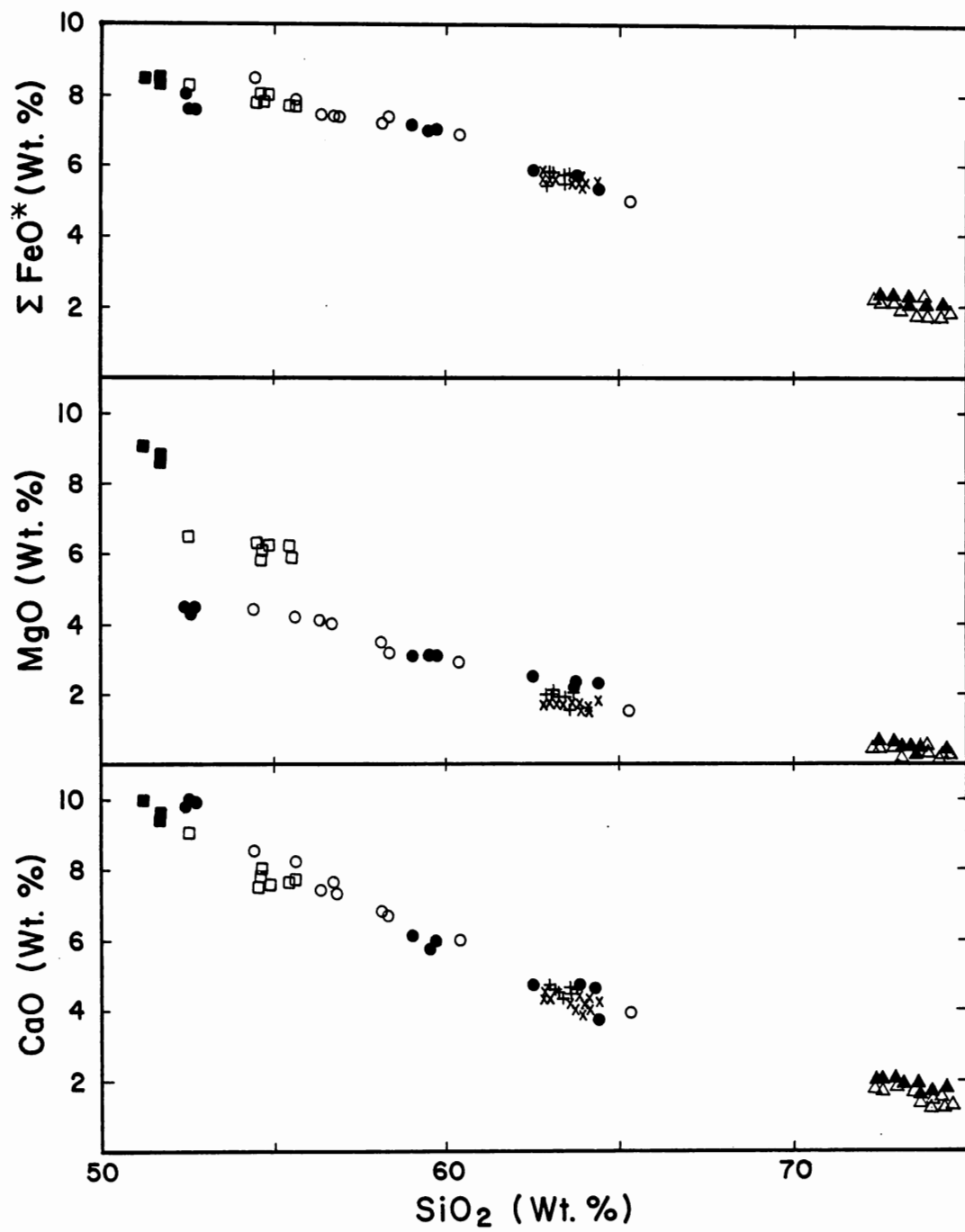


Figure 8. (Continued)

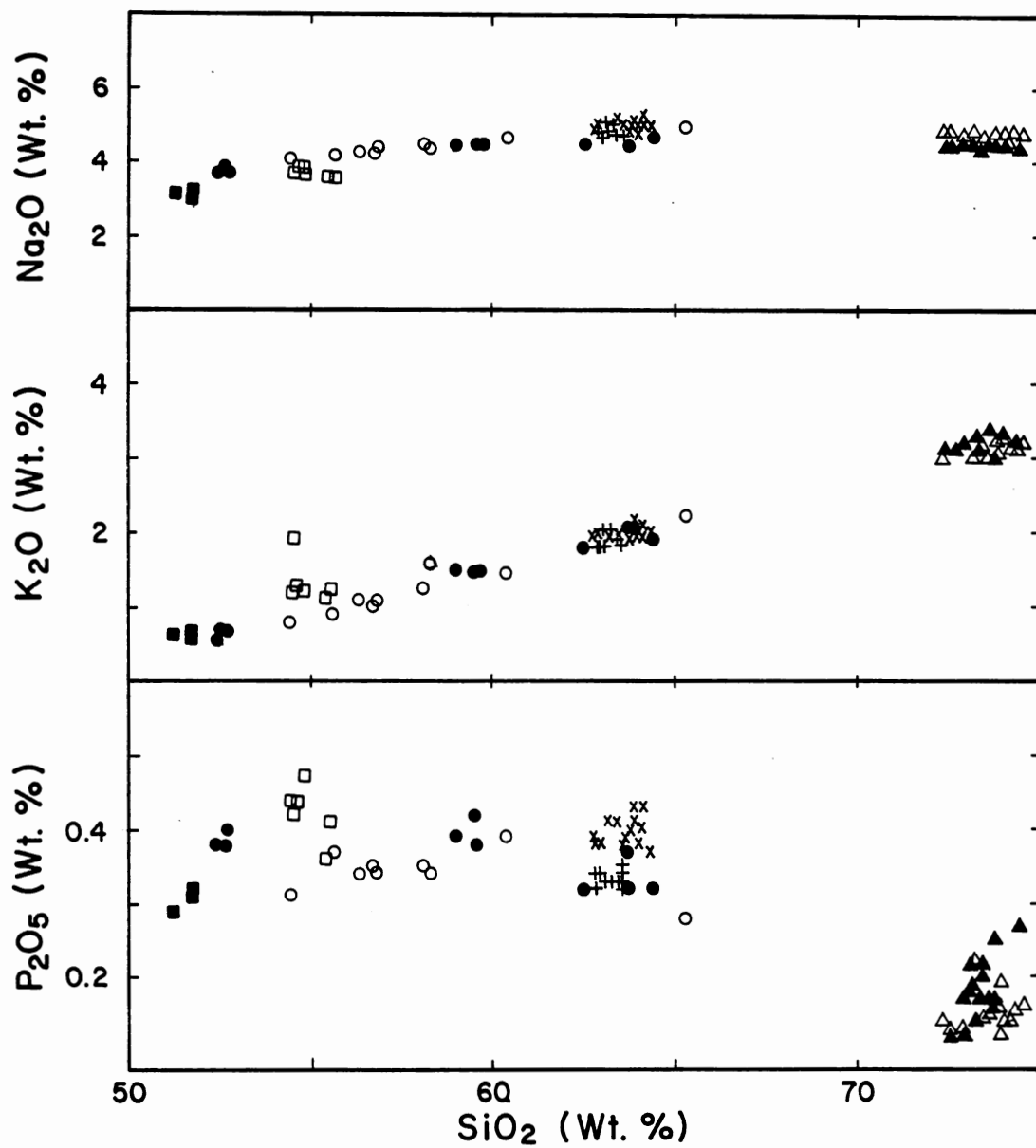


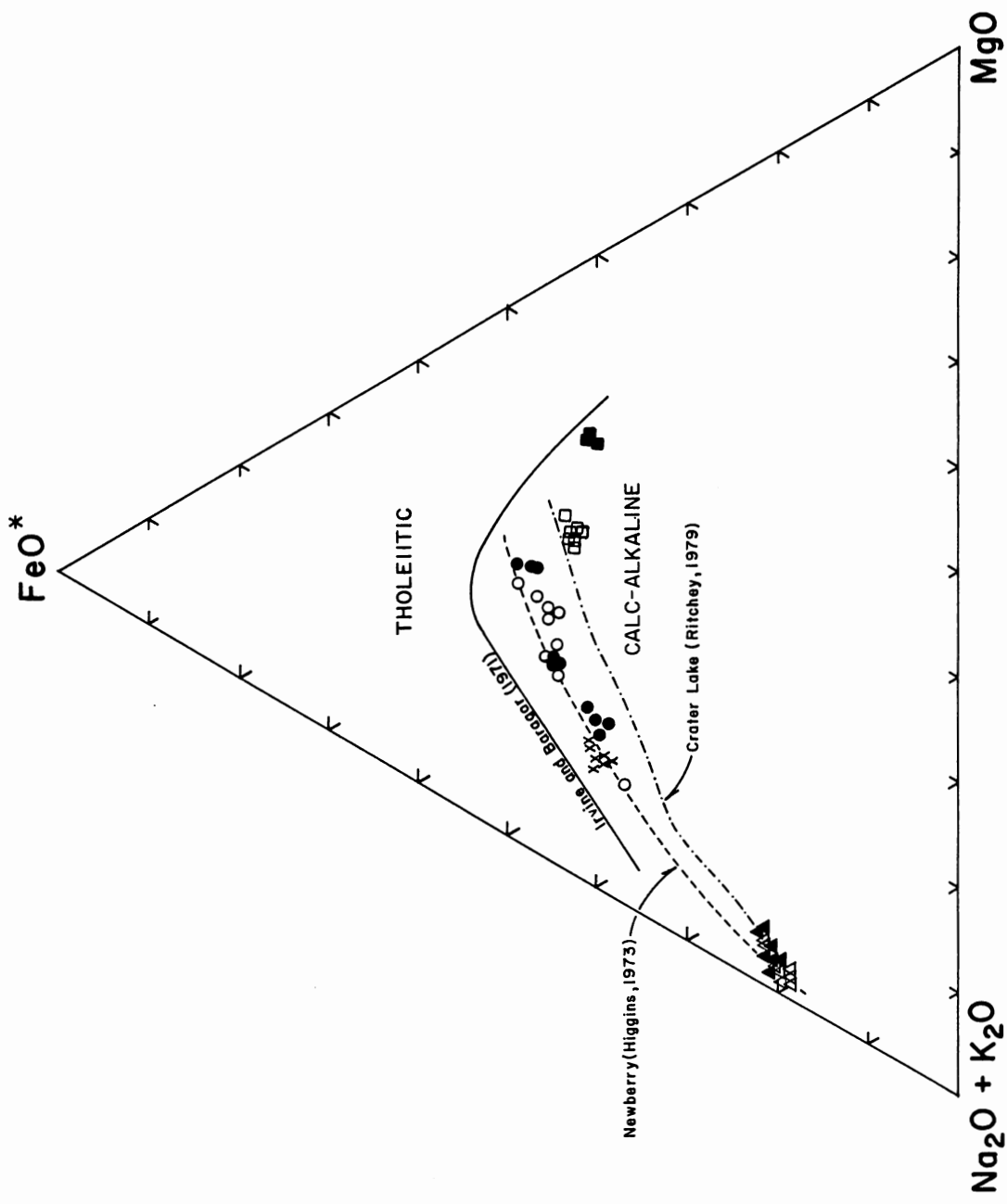
Figure 8. (Continued)

alkaline suites from a single volcanic complex. Only  $\text{TiO}_2$  and  $\text{P}_2\text{O}_5$  show significant scatter. The post-glacial basalts ( $\text{Ho}_{\text{BS}}$ ) have the highest MgO abundances. The subalkaline and calc-alkaline nature of the South Sister rocks is evident from inspection of Figures 9, 10, 11 and 12.

Volcanic rocks from South Sister have a wide range of  $\text{SiO}_2$  contents, from about 51%  $\text{SiO}_2$  to 74.5%  $\text{SiO}_2$ , and a compositional gap between about 65%  $\text{SiO}_2$  and 72%  $\text{SiO}_2$ . Even more striking is the compositional gap between the post-glacial, divergent magmas, between 55.5%  $\text{SiO}_2$  and 72%  $\text{SiO}_2$ . In contrast, bulk rock analyses from Mount Mazama range from 50%  $\text{SiO}_2$  to 72%  $\text{SiO}_2$  with no pronounced compositional gap (Ritchey, 1979; Williams, 1942). Products of the climactic eruption of Mount Mazama have a compositional gap between 55%  $\text{SiO}_2$  and 70%  $\text{SiO}_2$ , while the residual glasses change more gradually, with a smaller gap between 65%  $\text{SiO}_2$  and 74%  $\text{SiO}_2$  (Ritchey, 1979). Except for the compositional gaps, silica covariance with other major elements is similar for Mount Mazama and South Sister. The South Sister series is slightly higher in  $\text{K}_2\text{O}$  and lower in  $\text{Na}_2\text{O}$ , but the abundances of total alkalis are similar.

Several other features stand out in the major element data.  $\text{Na}_2\text{O}$  decreases slightly in the rhyodacitic rocks, a characteristic common also to silicic rocks from Newberry (Beyer, 1973), Yamsay Mountain (Hering, 1981), and Medi-

Figure 9. AFM diagram for lavas from the South Sister volcanic complex. Symbols as in Figure 8. Trends for Newberry (Higgins, 1973) and Crater Lake (Ritchey, 1979) shown by dashed lines. Solid line separating calc-alkaline and tholeiitic fields from Irvine and Baragar (1971).



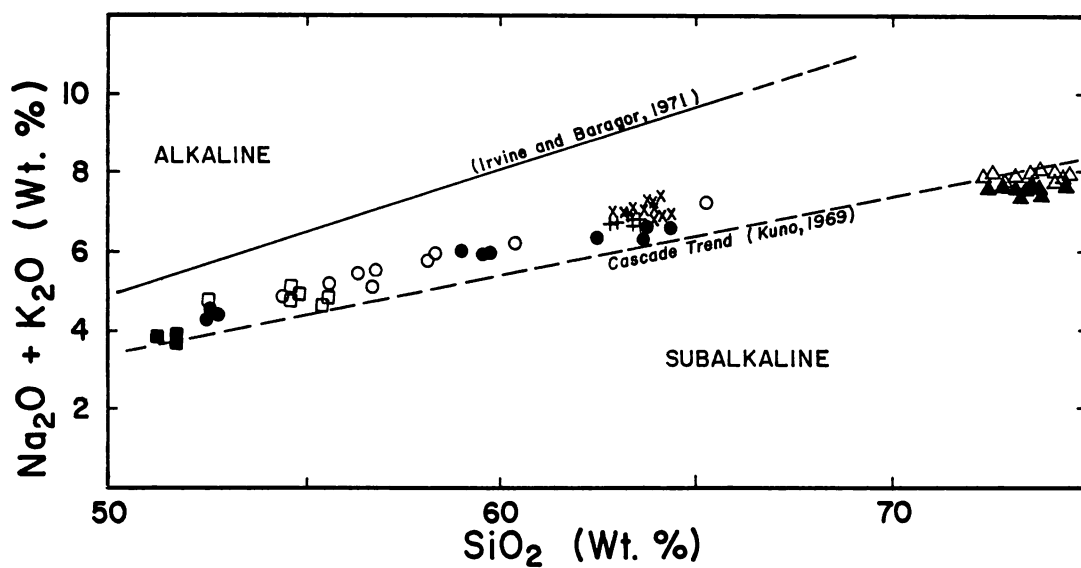


Figure 10. Total alkalies versus silica. Solid line separating alkaline and subalkaline fields after Irvine and Baragar (1971); dashed Cascade trend after Kuno (1969).

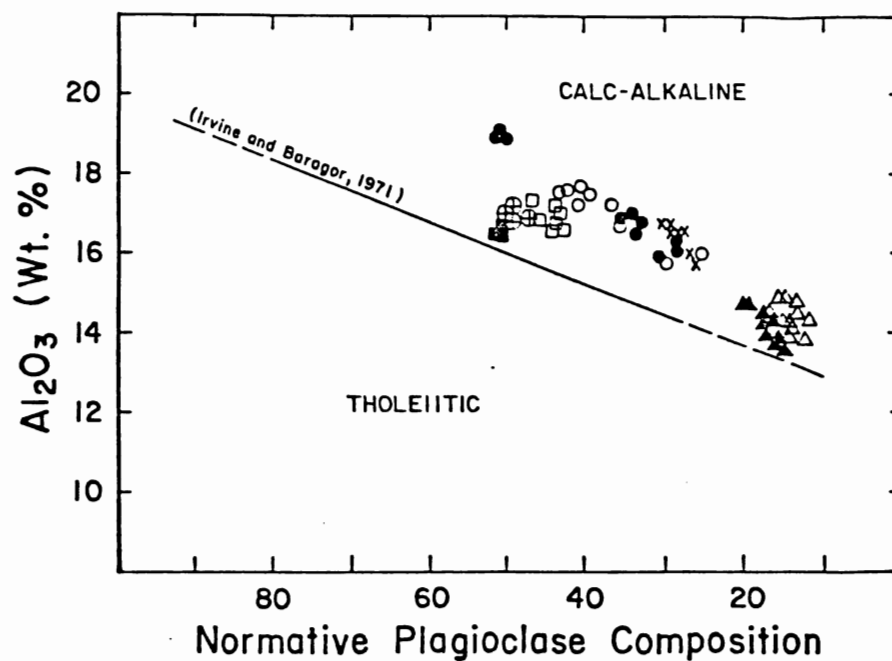


Figure 11.  $\text{Al}_2\text{O}_3$  versus normative plagioclase composition for lavas from the South Sister volcanic complex. Solid line separating calc-alkaline and tholeiitic fields after Irvine and Baragar (1971). Symbols as in Figure 8.

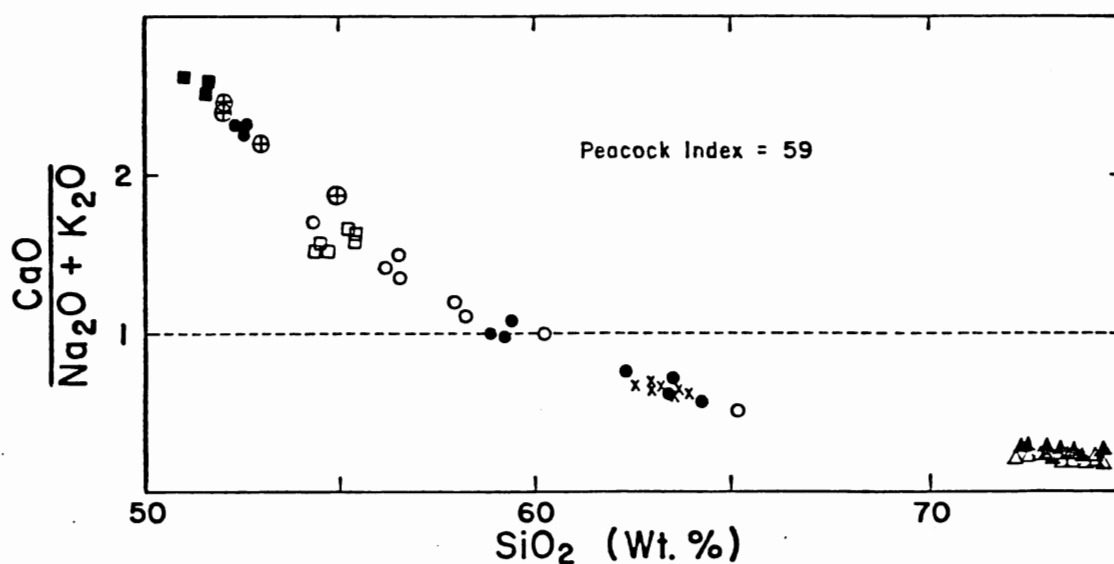


Figure 12. Peacock index (silica value at which  $\text{CaO}/\text{Na}_2\text{O} + \text{K}_2\text{O}$  is equal to 1.0) for lavas from the South Sister volcanic complex. Symbols as in Figure 8.

cine Lake (Condie and Hayslip, 1975). Slight inflections in the  $\text{TiO}_2$  and  $\text{P}_2\text{O}_5$  trends are approximately coincident with the appearance of ilmenite and apatite, respectively, on the liquidus. Early rhyodacites ( $\text{Ps}_{\text{rda}}$ ) are distinct from post-glacial rhyodacites ( $\text{Ho}_{\text{rda}}$ ) in that they have higher abundances of  $\text{Na}_2\text{O}$  and total alkalies, and lower abundances of  $\text{K}_2\text{O}$ .

$\text{FeO}^*/\text{FeO} + \text{MgO}$  ratios are plotted versus  $\text{SiO}_2$  in Figure 13. The ratios increase from 0.48 in the most basic rocks to 0.94 in the rhyodacites. The trends of the main cone rocks ( $\text{Ps}_{\text{ad}}$ ,  $\text{Ps}_{\text{ba}}$ ) show smooth variations and slopes which are distinct from either of the post-glacial eruptive units ( $\text{Ho}_{\text{bs}}$ ,  $\text{Ho}_{\text{rda}}$ ) or the early rhyodacites ( $\text{Ps}_{\text{rda}}$ ). The rhyodacitic rocks as a group display the strongest variation of  $\text{FeO}^*/\text{FeO} + \text{MgO}$  with increasing  $\text{SiO}_2$ . Hering (1981) noted that the  $\text{FeO}^*/\text{FeO} + \text{MgO}$  ratios at South Sister are anomalously high compared to other High Cascade volcanoes, but are similar to those at Newberry caldera and Yamsay Mountain, the large, differentiated shield complexes at the western margin of the Basin and Range province of Oregon.

The trace elements, Ba, Rb, Zr, Sr and Ni are plotted versus a modified Larsen index in Figure 14. The data define generally smooth variations with increasing DI but have significant scatter for Ni and Sr at low values of DI.

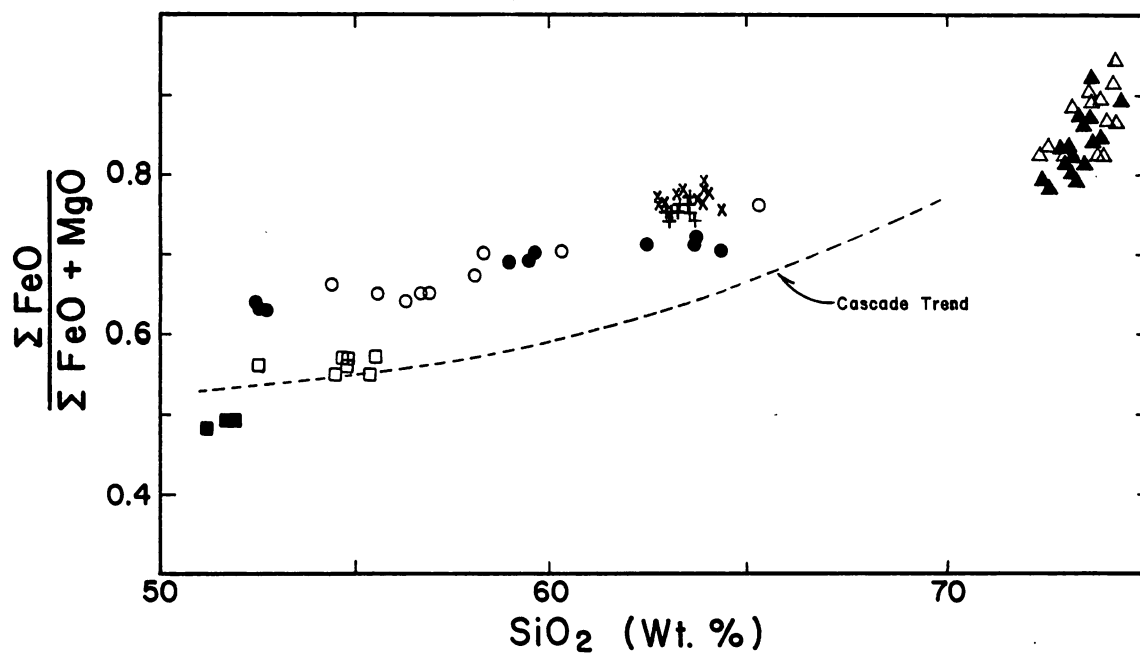
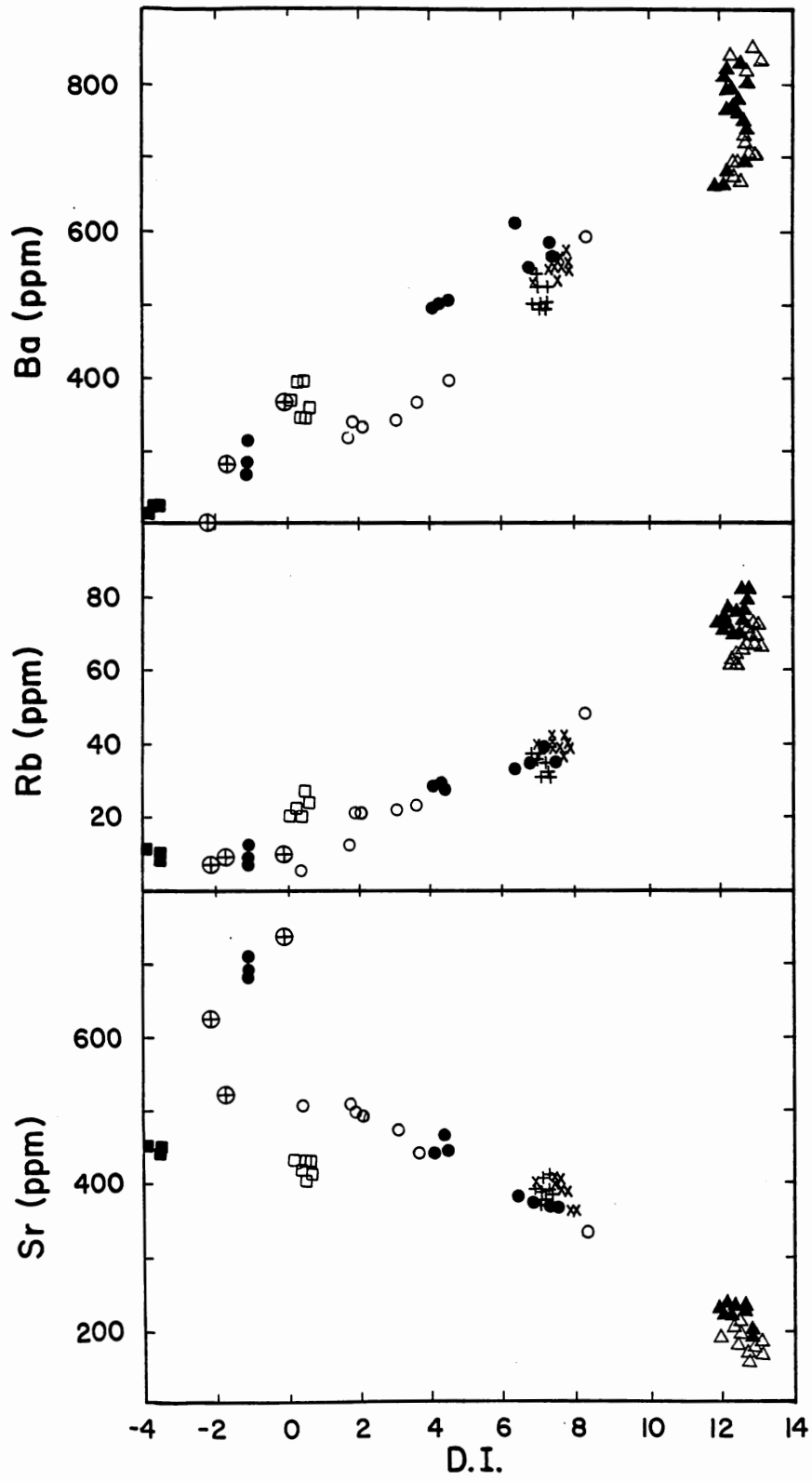


Figure 13. Total iron over total iron plus magnesium versus silica for lavas from the South Sister volcanic complex. Dashed Cascade trend after Osborn (1959). Symbols as in Figure 8.

Figure 14. Variation of selected trace elements with a modified Larsen differentiation index ( $D.I. = 1/3Si + K - Ca - Mg$ ). Symbols as in Figure 8.



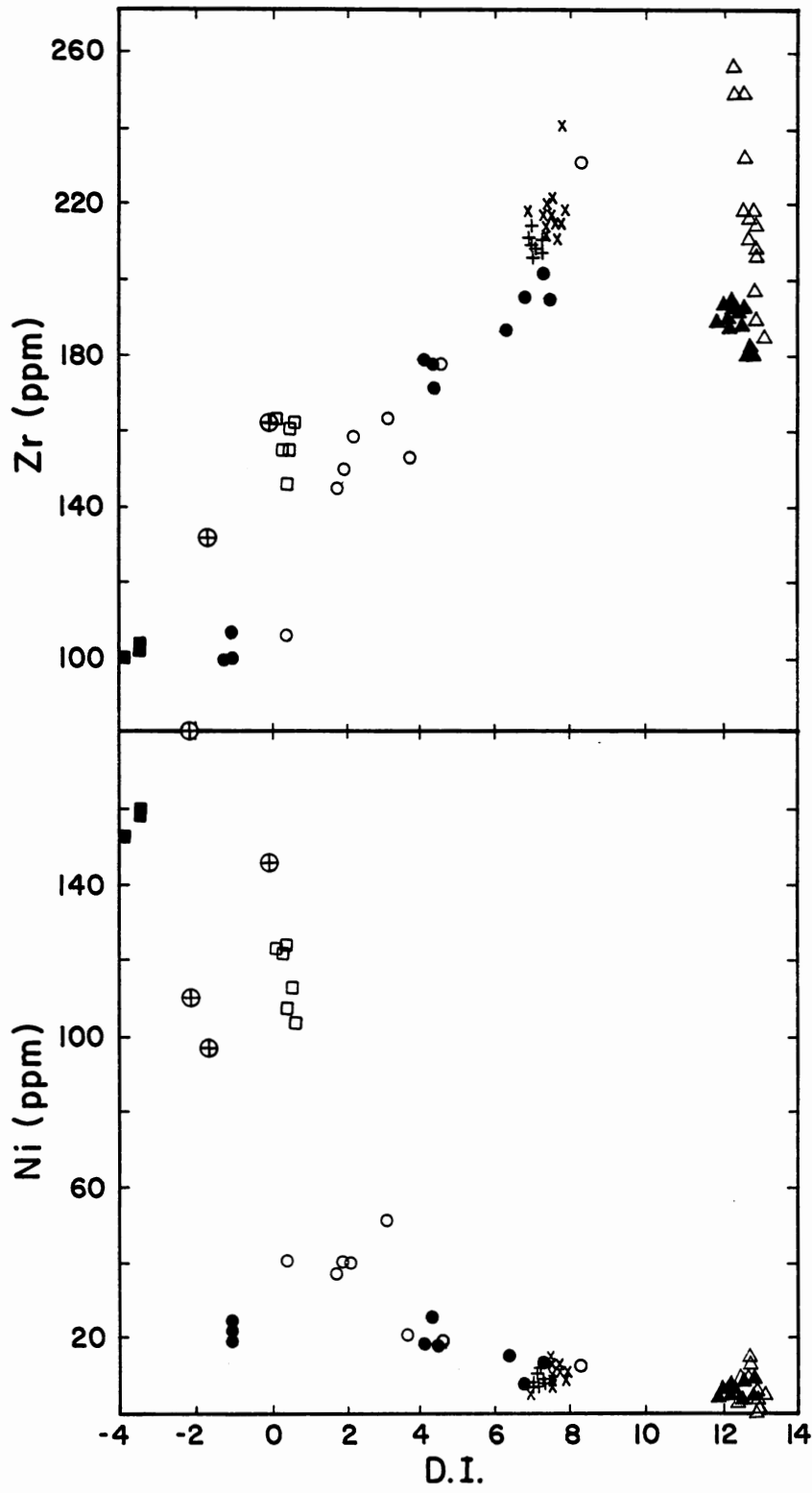


Figure 14. (Continued)

Wide compositional gaps exist only for the late-stage, divergent magmas, while narrower compositional gaps for the suite as a whole are evident only for Rb, Sr and, to a lesser extent, Ba. Ba abundances are lower at a given DI in the summit cone suite ( $Ps_{ba}$ ) than in rocks of similar composition from the main cone sequence ( $Ps_{ad}$ ). The rhyodacitic rocks ( $Ps_{rda}$ ,  $Ho_{rda}$ ) have a wide variation in trace element abundances for all elements plotted except Ni. Zr abundances drop off rapidly in the rhyodacitic rocks. The post-glacial rhyodacites ( $Ho_{rda}$ ) are distinctive from the early rhyodacites ( $Ps_{rda}$ ) in that they have generally higher abundances of Rb and Sr, and lower abundances of Zr than do the early rhyodacites. Ni abundances define a steep, negative slope with an inflection to a shallower slope at  $DI=4$ . Ni is strongly depleted in the andesitic and more silicic rocks.

### Basalts

The scatter in the Ni and Cr data at the mafic end of the trace element - DI plots is not random (Figure 15). Basaltic rocks associated with each eruptive unit have characteristic trace element signatures. The oldest ( $Ps_{bs}$ ) and youngest ( $Ho_{bs}$ ) basalts have Ni abundances between 90 ppm and 580 ppm. Main ( $Ps_{ad}$ ) and summit ( $Ps_{ba}$ ) cone basaltic rocks have Ni abundances less than 40 ppm and Cr

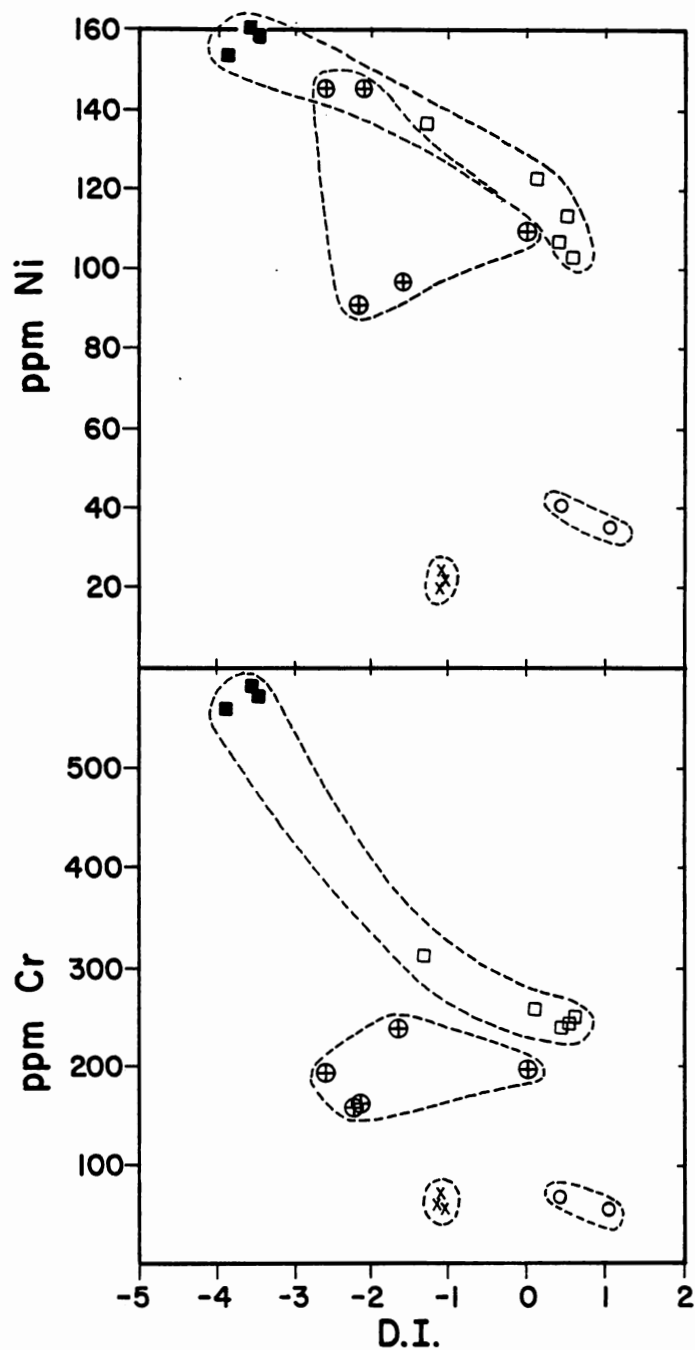


Figure 15. Variation of Ni and Cr with a modified Larsen differentiation index ( $D.I. = 1/3 Si + K - Ca - Mg$ ) in basaltic rocks from the South Sister volcanic complex. Symbols as in Figure 8.

abundances less than 70 ppm. The post-glacial basaltic rocks have the highest Ni and Cr abundances. The low Ni and Cr abundances in the main and summit cone basalts are typical of basaltic rocks from calc-alkaline volcanoes throughout the world (Jakes and White, 1972).

### Mineral Composition and Variation

A generalized paragenetic sequence for the South Sister volcanic suite is presented in Figure 16 and is based on petrographic examination of lavas from each unit. The solid lines indicate the presence of the mineral as a primary liquidus phase, while dashed lines indicate only the sporadic occurrence of a phase as either an inclusion within a primary phase, a remnant of incomplete peritectic reaction (olivine), or as a xenocryst.

Electron microprobe analyses were obtained for phenocrysts from selected samples of all volcano-stratigraphic units with the exception of the Pleistocene shield basalts ( $Ps_{bs}$ ). The raw data and calculated compositions are given in Appendix C and plotted in Figures 17 and 18.

#### Olivine

Olivine ( $\pm$  plagioclase) is the primary crystallizing phase in both the shield basalts ( $Ps_{bs}$ ) and the post-glacial basalts. Olivine is joined by clinopyroxene as the

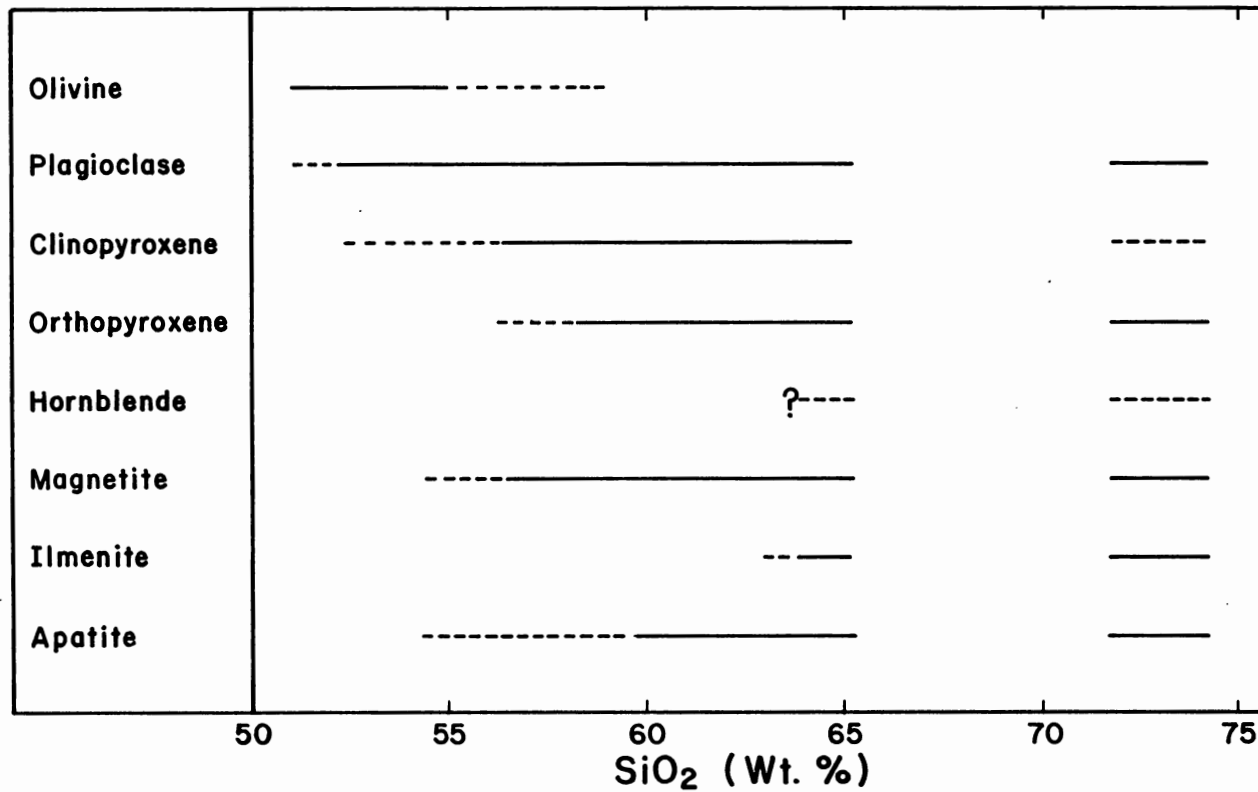


Figure 16. Generalized paragenetic sequence for the South Sister volcanic suite. See text for explanation.

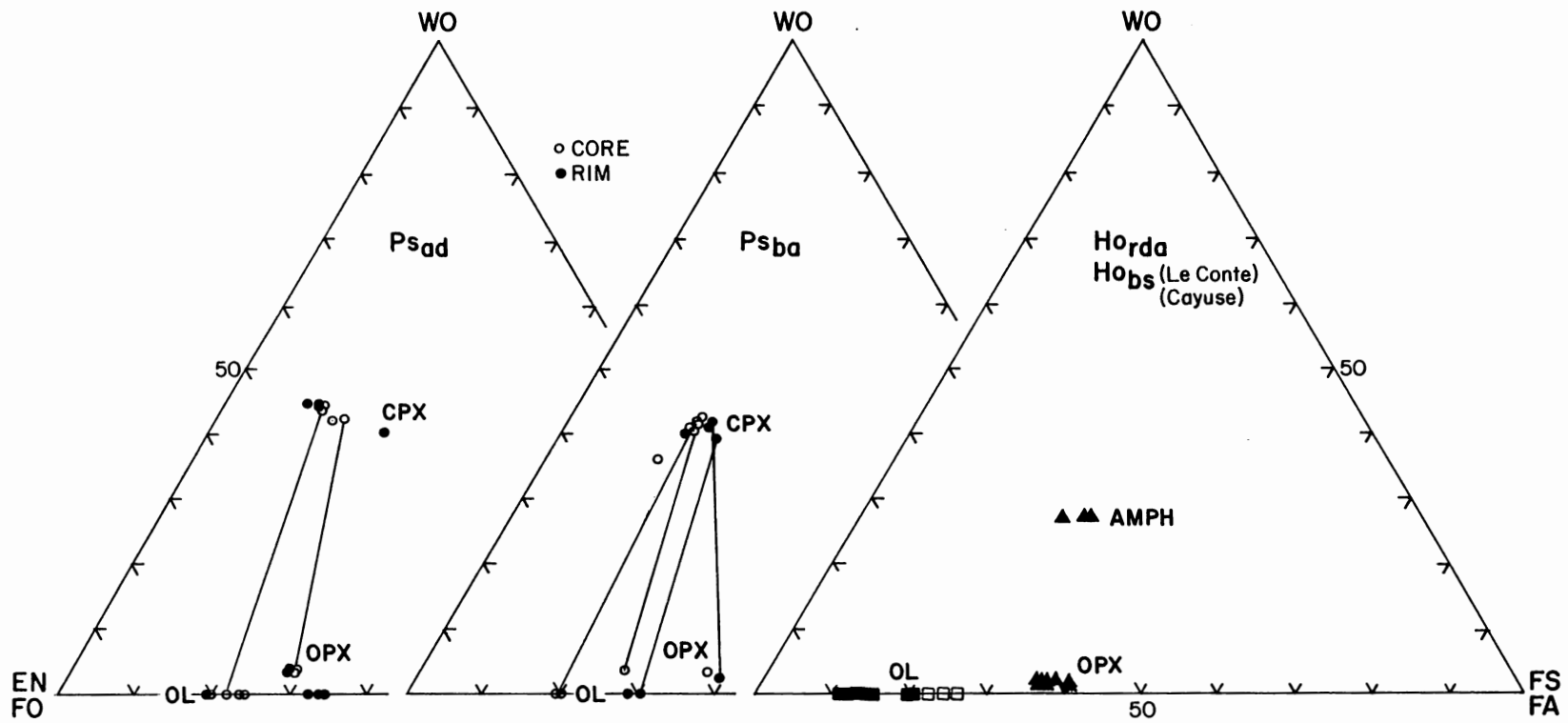


Figure 17. Mafic phenocryst compositions in lavas from the South Sister volcanic complex. Symbols as in Figure 8.

dominant mafic phases in the main ( $Ps_{ad}$ ) and summit ( $Ps_{ba}$ ) cone basalts. Deeply corroded olivine remnants found in one andesitic flow appear to represent incomplete peritectic reaction of primary olivine with the liquid to form orthopyroxene. Olivine compositions from main cone ( $Ps_{ad}$ ), summit cone ( $Ps_{ba}$ ), and post-glacial ( $Ho_{bs}$ ) basalts and basaltic andesites are plotted in Figure 17, along with compositions of their coexisting pyroxenes. The total compositional range is from  $Fo_{88}$  to  $Fo_{66}$ , and normal zonation is prevalent. The post-glacial basalts have the most magnesian compositions ( $Fo_{88}$  to  $Fo_{74}$ ). Inclusions of cubic, red-brown, chromian spinel are common in olivine phenocrysts of basalts from all stratigraphic units.

#### Pyroxenes

Data from pyroxene analyses for samples taken from South Sister volcano are plotted in Figure 17. Augite is present as a primary crystallizing phase throughout the main cone ( $Ps_{ad}$ ) and summit cone ( $Ps_{ba}$ ) sequences, but occurs only rarely as xenocrysts in rhyodacitic rocks. The augites differ only slightly in composition, with weak normal zonation in the summit cone sequence ( $Ps_{ba}$ ) and weak normal or reverse zonation in the main cone sequence ( $Ps_{ad}$ ). Augites from the summit cone sequence are more Fe-rich and less calcic than those from the main cone

sequence.

Petrographic examination of chemically-analyzed rocks showed that hypersthene formed late in rocks in the basaltic andesite range as a product of reaction between olivine and liquid. Hypersthene is present in all of the differentiated rocks. It is the primary mafic phase in the rhyodacitic rocks. It ranges in composition from  $En_{70}$  to  $En_{58}$ , and there is some overlap in orthopyroxene compositions between andesitic to dacitic rocks and the rhyodacitic rocks. Weak reverse zonation is common in hypersthene of all units, but weak normal zonation is also found. Hypersthene from the summit cone sequence are more Fe-rich than those from the main cone sequence, as are their co-existing augites.

The clinopyroxenes from South Sister are enriched in  $Al_2O_3$  compared to their co-existing orthopyroxenes.  $Al_2O_3$  and  $TiO_2$  abundances decrease with increasing  $FeO^*$  in all the clinopyroxenes and in orthopyroxene from the summit cone sequence and the rhyodacitic rocks. These trends are similar to those in pyroxene from Yamsay Mountain (Hering, 1981) and unlike those from the southern Cascade volcanoes (Smith and Carmichael, 1968).

#### Amphibole

A single hornblende xenocryst was found in one dacitic

flow from the main cone ( $Ps_{ad}$ ). Otherwise, hornblende does not occur in rocks less silicic than rhyodacite. In the rhyodacites ( $Ps_{rda}$ ,  $Ho_{rda}$ ) hornblende occurs rarely as microphenocrysts. The hornblendes are relatively fresh and show only minor alteration of the rims to opacite. The pargasitic amphibole microphenocrysts in the rhyodacitic rocks from South Sister have higher  $FeO^*$  abundances and  $FeO^*/MgO$  ratios than do pargasites in similar rocks from Crater Lake (Ritchey, 1979) and Yamsay Mountain (Hering, 1981). This feature is consistent with the generally higher  $FeO^*$  abundances of the South Sister suite relative to other Cascade volcanoes (Clark, unpublished data; Hering, 1981).

#### Plagioclase

Plagioclase is a primary liquidus phase for all the rocks in this study with the exception of the Cayuse basalts. Phenocryst and microphenocryst compositions are plotted in Figure 18 and range from  $An_{82}$  to  $An_{22}$ . Compositional zonation within plagioclase phenocrysts is seen in all rock types and may be normal, reversed, oscillatory, or patchy. The maximum variation of anorthite content in a single phenocryst is 12 mole percent. Within a single rock type the maximum variation of anorthite content in plagioclase phenocrysts is 19 mole percent ( $Ho_{rda}$ ). Plagioclase

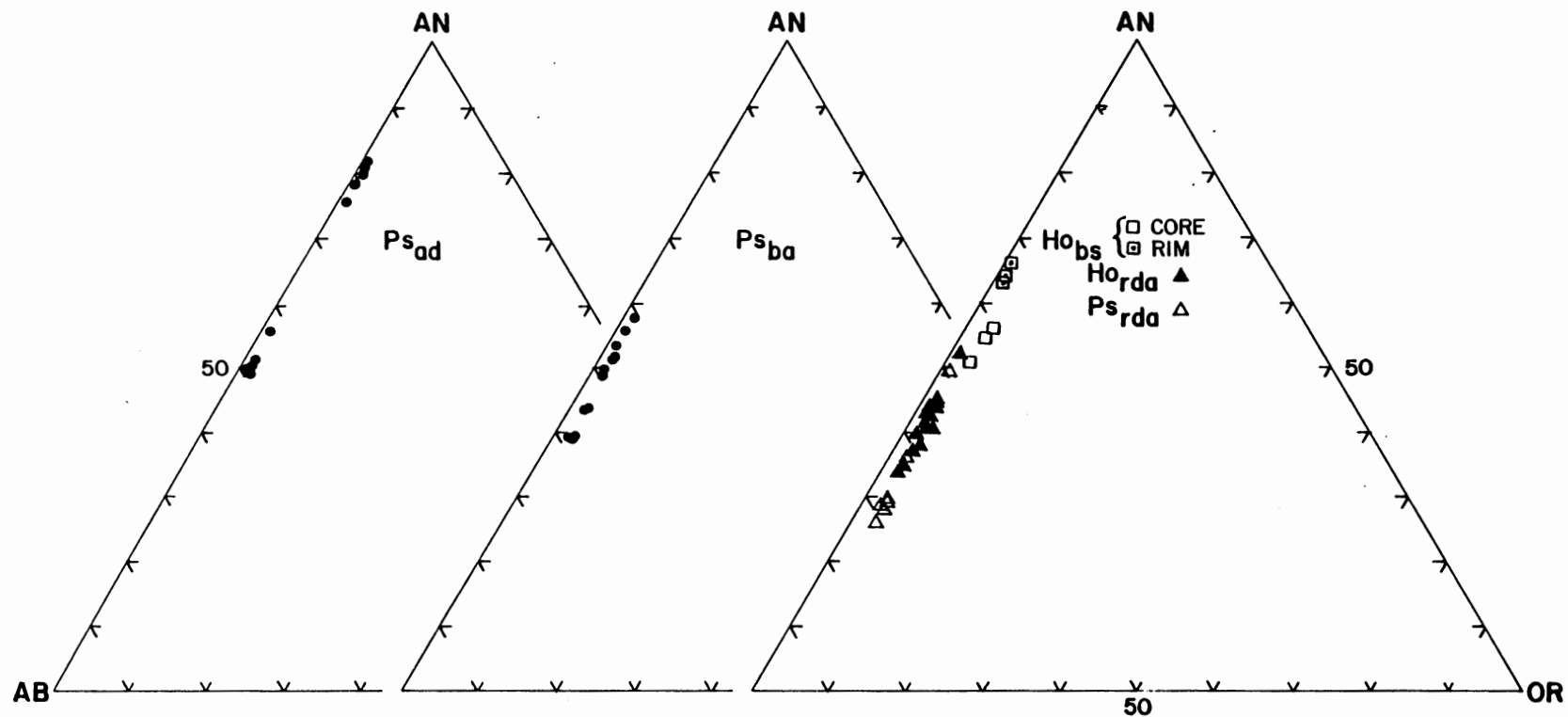


Figure 18. Plagioclase phenocryst compositions in lavas from the South Sister volcanic complex. Symbols as in Figure 8, except where noted.

compositions range from  $An_{56}$  to  $An_{49}$  in the basalts and basaltic andesites, from  $An_{56}$  to  $An_{39}$  in the andesites and dacites, and from  $An_{52}$  to  $An_{22}$  in the rhyodacites. Basalts interbedded with the main cone sequence ( $Ps_{ad}$ ) contain the most calcic plagioclase phenocrysts ( $An_{82}$  to  $An_{76}$ ), and the most sodic plagioclase phenocrysts are found in the early rhyodacites ( $Ps_{rda}$ ). Compositions of groundmass plagioclase are equivalent to, or only slightly more sodic than compositions of plagioclase microphenocrysts. The abundances of the orthoclase component in the plagioclase phenocrysts and microphenocrysts range from  $Or_{.1}$  to  $Or_{3.6}$ . The highest  $Or$  abundances in plagioclase phenocrysts occur in the fritted phenocrysts in the post-glacial rhyodacites and in the irregular, clear cores of strongly corroded phenocrysts in the post-glacial basalts from Le Conte Crater.

Disequilibrium textures in plagioclase phenocrysts are found throughout the South Sister volcanic suite. It is noteworthy that the textures are best-developed in the basaltic rocks ( $Ps_{ad}$ ,  $Ps_{ba}$ ,  $Ho_{bs}$ ) and in the post-glacial rhyodacites. Only minor resorption and glass inclusions are found in plagioclase phenocrysts in the andesitic, dacitic, and early rhyodacitic rocks. Plagioclase disequilibrium textures in the mafic rocks are distinctly different from those in the post-glacial rhyodacites

(Figures 5 and 6). The disequilibrium textures are described in detail in Chapter 1 along with their significant compositional features. The importance of these textures to the petrogenesis of the late-stage, divergent magmas will be discussed in the last chapter.

#### Fe-Ti Oxides and Apatite

Magnetite and ilmenite compositions for the post-glacial rhyodacites are tabulated in Appendix C. Magnetite and apatite began to crystallize in the andesites and were joined by ilmenite in the dacites and rhyodacites.

## CHAPTER 3

## PETROLOGY AND GEOCHEMISTRY

Field, petrographic and geochemical data presented in Chapters 1 and 2 reveal that South Sister has undergone a petrologic history in which the volumetrically dominant lavas progressed from basaltic ( $Ps_{bs}$ ) to silicic ( $Ps_{rda}$ ), through intermediate ( $Ps_{ad}$ ), and finally to more basaltic, ( $Ps_{ba}$ ) compositions. Post-glacial flank eruptions were of strongly contrasting basaltic ( $Ho_{bs}$ ) and rhyodacitic ( $Ho_{rda}$ ) magmas. The following sections of Chapter 3 consider primarily the petrogeneses of the main ( $Ps_{ad}$ ) and summit ( $Ps_{ba}$ ) cone lavas. Detailed discussion of the petrology and geochemistry of the rhyodacitic rocks ( $Ps_{rda}$ ,  $Ho_{rda}$ ) and their associated basalts ( $Ps_{bs}$ ,  $Ho_{bs}$ ) is deferred until Chapter 4.

Phase Relations

Bulk rock compositions for the South Sister Suite were projected into the pseudoquaternary system  $XO - YO - R_2O_3 - ZO_2$  using the calculation procedures of O'Hara

(1976). FeO was added to MgO and the alkali feldspar components were calculated as equivalent moles of anorthite to minimize the effects of solid solution on the interpretation of the phase relations. Figure 19 is a projection from clinopyroxene onto the plane  $XO.R_2O_3 - YO - ZO_2$ , where

$$XO = (CaO + 2Na_2O + 2K_2O) \times 56.08$$

$$YO = (MgO + FeO + MnO - TiO_2) \times 40.32,$$

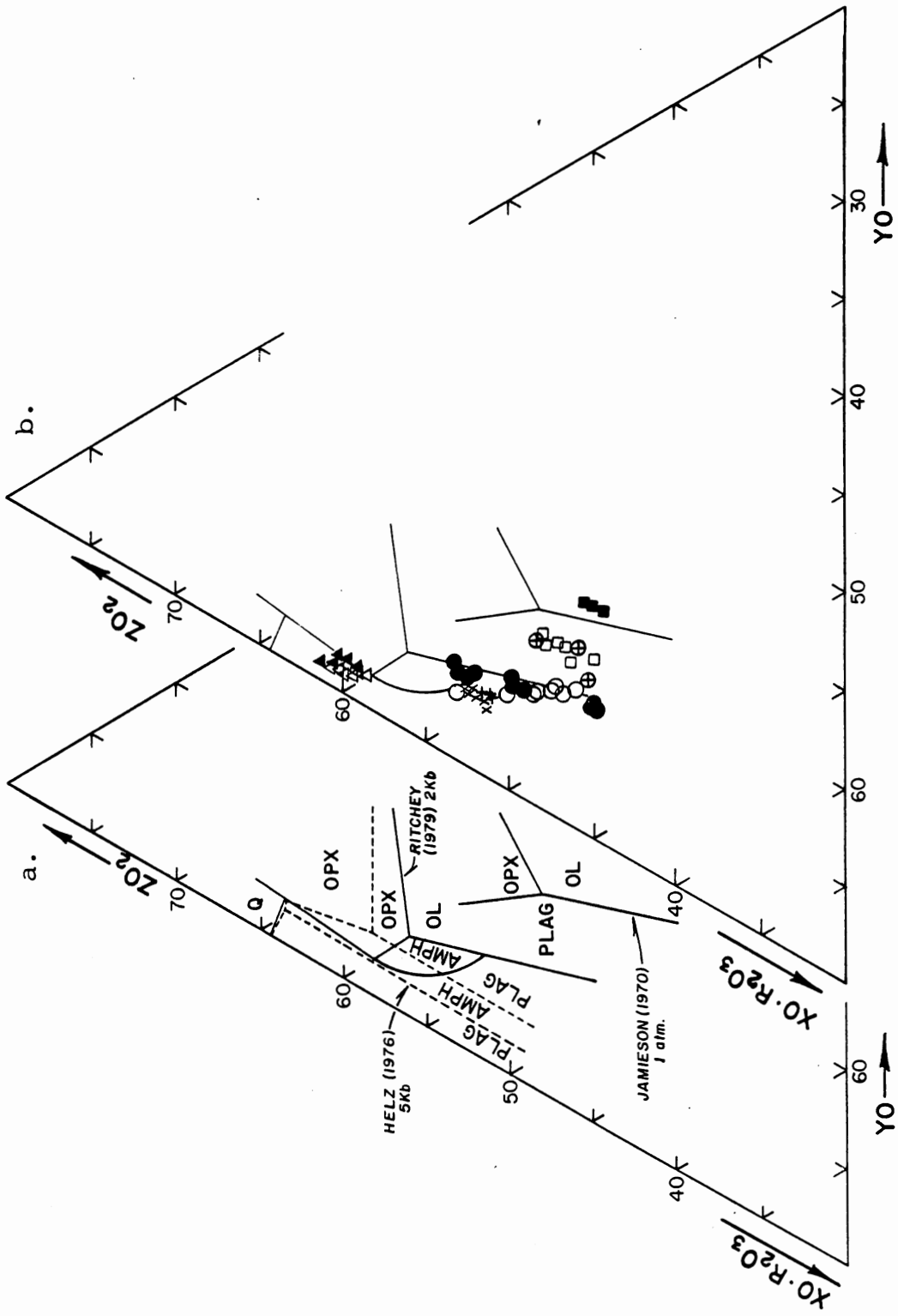
$$R_2O_3 = (Al_2O_3 + Fe_2O_3 + TiO_2 + Na_2O + K_2O) \times 101.96,$$

$$ZO_2 = (SiO_2 - 2Na_2O - 2K_2O) \times 60.09.$$

This projection best illustrates the calc-alkaline trend, because silica enrichment is apparent, and clinopyroxene is an early liquidus phase in the main and summit cone lavas. The compositional trends reflect the general geochemical evolution of the magmas, but do not exactly reproduce a liquid line of descent, probably owing to the effects of crystal accumulation.

Figure 19a shows experimentally determined phase relations for basaltic systems at one atmosphere under dry conditions (Jamieson, 1970) and at 5 Kb water pressure (Helz, 1976), and for water-undersaturated basaltic andesite to rhyodacitic compositions at  $P_{total} \approx 2$  Kb (Ritchey, 1979). These data indicate that the phase volume of OL + CPX increases at the expense of the phase volumes of PL + CPX and OPX + CPX as water pressure increases, and

Figure 19.  $XO \cdot R_2O_3 - YO - ZO_2$  projection from clinopyroxene. 19a shows experimentally-determined phase relations for basalt at 1 atm (Jamieson, 1970), at  $P_{H_2O} < P_{total} = 2 \text{ Kb}$  (Ritchey, 1979), and at  $P_{H_2O} = 5 \text{ Kb}$  (Helz, 1976). 19b shows South Sister compositions projected from clinopyroxene. Symbols as in Figure 8.



that the phase volume of amphibole opens and expands with increasing water pressure as olivine and clinopyroxene react with the liquid.

Compositions of South Sister rocks are projected in Figure 19b. The main and summit cone sequences plot near, but slightly oblique to the 2 Kb, water-undersaturated, PL - OL - CPX cotectic of Ritchey (1979). Initial liquids are in equilibrium with plagioclase, olivine, and clinopyroxene, and trend toward the stability fields of orthopyroxene and amphibole. Though several of the main cone lavas appear to enter the field of primary amphibole crystallization, the presence in these rocks of orthopyroxene, rather than amphibole, suggests their crystallization under conditions of lower  $P_{H_2O}$  than those attendant during the evolution of the Crater lake divergent suite, described by Ritchey (1979). The effect of lower  $P_{H_2O}$  during the crystallization of rocks of these compositions is to increase the temperature interval between the appearance of liquidus or near-liquidus plagioclase, clinopyroxene, and orthopyroxene, and the upper temperature stability limit of amphibole crystallization (Eggler, 1972). The relationships in Figure 19b are consistent with the derivation of the main ( $Ps_{ad}$ ) and summit ( $Ps_{ba}$ ) cone lavas by fractional crystallization along a multi-phase cotectic (Ritchey, 1979). Alternatively, the same range of compositions can

be produced by progressive partial melting of a hydrous mantle source (Kushiro, 1974, 1979). These processes and their relative importance to the petrogenesis of South Sister lavas are discussed below.

The projection from clinopyroxene is only thermodynamically valid for CPX-bearing systems. Neither the rhyodacitic units, nor the post-glacial basalts contain clinopyroxene as a primary liquidus phase. This projection remains, however, a useful method of representing bulk rock compositions. The post-glacial basalts from Cayuse Crater plot near and parallel to the anhydrous one atmosphere OL - PL - CPX cotectic. The Le Conte basalts also plot parallel to this phase boundary, but may have evolved at a slightly elevated water pressure. Both early and post-glacial rhyodacitic rocks plot along the OPX - PL - CPX cotectic at  $P_{\text{total}} = 2 \text{ Kb}$ , and their position on the diagram reflects their lack of primary liquidus amphibole. The compositional gap noted in the major element data for the South Sister suite is apparent also in this projection.

#### Trace Element Variations

Baker et al (1977) and Weaver (1972) have shown that ratios of incompatible trace elements provide sensitive indicators of the consanguinity of certain alkaline magmatic suites. Hering (1981) and Meijer and Reagan (1981) successfully extended this approach to calc-alkaline rocks.

During the geochemical evolution of a group of magmas related by either fractional crystallization from a parental magma, or by progressive partial melting of a uniform source, the concentrations of two incompatible trace elements change in successive liquids, but their ratio remains constant (Baker et al, 1977; Baker, 1978). The XRF and AAS trace element data for volcanic rocks from South Sister presented in Chapter 2 illustrate the smooth variations typical of a suite of rocks from an individual volcanic center. Reliable neutron activation (INAA) trace element data were not obtained for this study, but data for a random suite of rocks from South Sister are available from Steinborn (1972). Significant among these data are the variations in the incompatible trace elements, Th and Rb, shown in Figure 20. Th and Rb have a strong linear covariance, and Th/Rb ratios are constant through the suite. A least-squares linear regression analysis of the data yields a Th/Rb ratio of 0.11 and a Y-intercept value of -0.04 ppm Th. Th/Rb ratios are constant despite major differences in charge and ionic radii between Th and Rb, and this constancy probably results from the nearly ideal exclusion of these elements from crystalline phases during partial melting or fractional crystallization (Baker, 1978). These data indicate that fractional crystallization or partial melting of sources with similar Th/Rb ratios were the processes most likely responsible for the generation

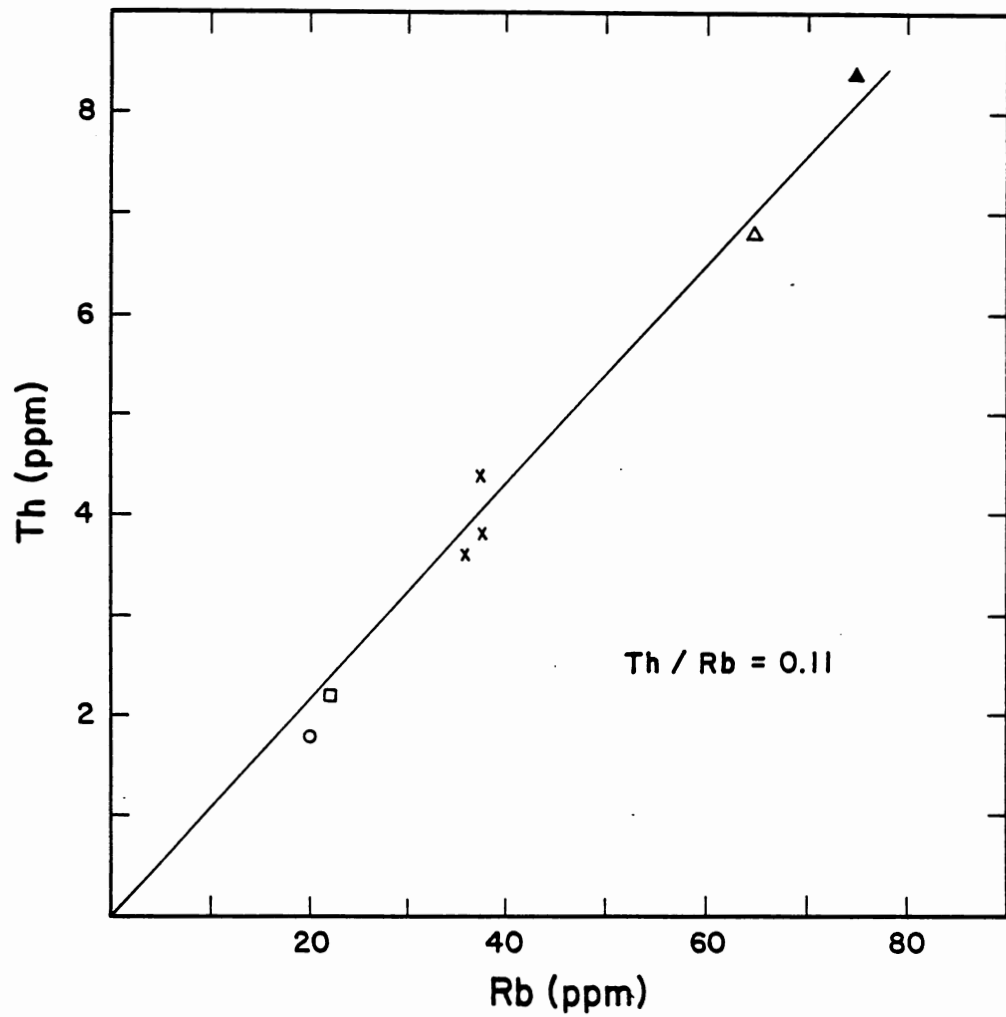


Figure 20. Th versus Rb for lavas from the South Sister volcanic complex. Symbols as in Figure 8. Data from Steinborn (1972).

of the South Sister volcanic suite.

### Fractional Crystallization

Fractional crystallization models were developed for selected suites of South Sister volcanic rocks and utilized a modified versions of the least-squares petrologic mixing program described by Bryan et al (1969) and Wright and Doherty (1970). Phase proportions added to or subtracted from a parental liquid to generate a differentiated liquid were calculated by computer. Phenocryst and whole rock data used in the calculations are listed in Appendices B and C. A mix is considered satisfactory if the sum of the squares of the residuals,  $\Sigma r^2$ , is less than unity, and if the phase compositions and proportions result in a petrologically plausible model. The rock suites chosen for modeling were from the main ( $Ps_{ad}$ ) and summit ( $Ps_{ba}$ ) cone sequences, and were those which displayed the widest compositional variation, and for which good stratigraphic control was available.

Predicted versus observed trace element abundances were compared in the models derived below for the elements Rb, Sr, Zr, Ba, Ni and Cr. Trace element abundances in parental and derivative liquids provide sensitive indicators of the validity of models calculated from major element compositions (Baker, et al, 1977). Predicted trace element abundances in successive liquids were calculated

using the Rayleigh law fractionation equation:

$$C_L = C_0 F^{(\bar{D}-1)},$$

where  $C_0$  = the concentration of the trace element in the parental liquid

$C_L$  = the concentration of the trace element in the residual liquid

$F$  = the fraction of residual liquid

$\bar{D}$  = the bulk distribution coefficient

Phase proportions and the fraction of liquid remaining were obtained from the major-element fractionation models. Because individual mineral/liquid distribution coefficients can vary with  $T$ ,  $P$ ,  $f_{O_2}$  and magma composition, and the scarcity of data makes it difficult to predict quantitatively the variation for a given suite of rocks, predicted trace element abundances in derivative liquids were calculated using the high and low extremes of published distribution coefficients in calc-alkaline rocks. Values for the distribution coefficients used in this study are summarized in Table 1. Owing to the wide variation in predicted trace element abundances caused by the use of extreme values of the individual mineral/liquid distribution coefficients, deviation of the observed trace element abundances from the calculated range of predicted abundances is significant reason to reject a particular model.

TABLE 1.  
RANGES OF DISTRIBUTION COEFFICIENTS

	<u>Olivine</u>	<u>Clinopyroxene</u>	<u>Orthopyroxene</u>	<u>Plagioclase</u>
Rb	.01- .02	.01- .14	.01- .03	.02- .20
Sr	.01- .10	.05- .15	.01- .04	1.0 -3.5
Zr	.01- .02	.20- .50	.01- .20	.01- .08
Ba	.01- .02	.01- .10	.01- .10	.10- .50
Ni	5.0 -25.0	4.0 - 9.0	1.0 -10.0	.02- .40
Cr	.20-50.0	10.0 -100.0	5.0 -75.0	.01- .20

	<u>Magnetite</u>	<u>Ilmenite</u>	<u>Apatite</u>	<u>Hornblende</u>
Rb	.02- .30	.02- .30	.01- .10	.05- .10
Sr	.02- .30	.02- .30	2.0 -5.0	.20- .40
Za	.50- 2.0	.50- 2.0	.10- .50	.20- .80
Ba	.02- .30	.02- .30	.01- .10	.20- .40
Ni	5.0 - 20.0	.50- 2.0	.01- .10	5.0 -15.0
Cr	10.0 -100.0	1.0 -10.0	.01- .10	5.0 -50.0

Data sources: Arth (1976)  
Gill (1978)  
Ritchey (1979)  
Baitis and Lindstrom (1980)  
Luhr and Carmichael (1980)

Main Cone Andesites and Dacites (Ps<sub>ad</sub>)

Lavas ranging from basalt to dacite form the bulk of the main cone, but andesites and dacites are volumetrically dominant. The suite selected for modeling consists of ten flows collected from the northeastern flank of the volcano. The compositional variations of major and trace element abundances with stratigraphic position are plotted in Figure 21. Within the section the earliest lavas were dacitic, and compositions became more mafic with time. A trend reversal to andesitic composition is present at the top of the sequence. An apparent compositional gap exists between approximately 52% SiO<sub>2</sub> and 59% SiO<sub>2</sub>. Most trace element abundances reflect this compositional gap as well, but Ni and Cr have nearly continuous variations.

Models of incremental fractional crystallization derived for the main cone sequence progress from basalt to dacite. Five of these are illustrated in Table 2, along with predicted and observed trace element abundances. Mass balance models based on major element abundances of lavas and phenocrysts yield exceptionally good fits.  $\Sigma r^2$  is less than 0.06 in all cases. The largest deviations between the observed and predicted residual liquid compositions were for the alkalis, Na<sub>2</sub>O and K<sub>2</sub>O. The data show that initial fractionation of OL + CPX + PL + MT + AP is capable of generating the compositions of main cone andesites from a

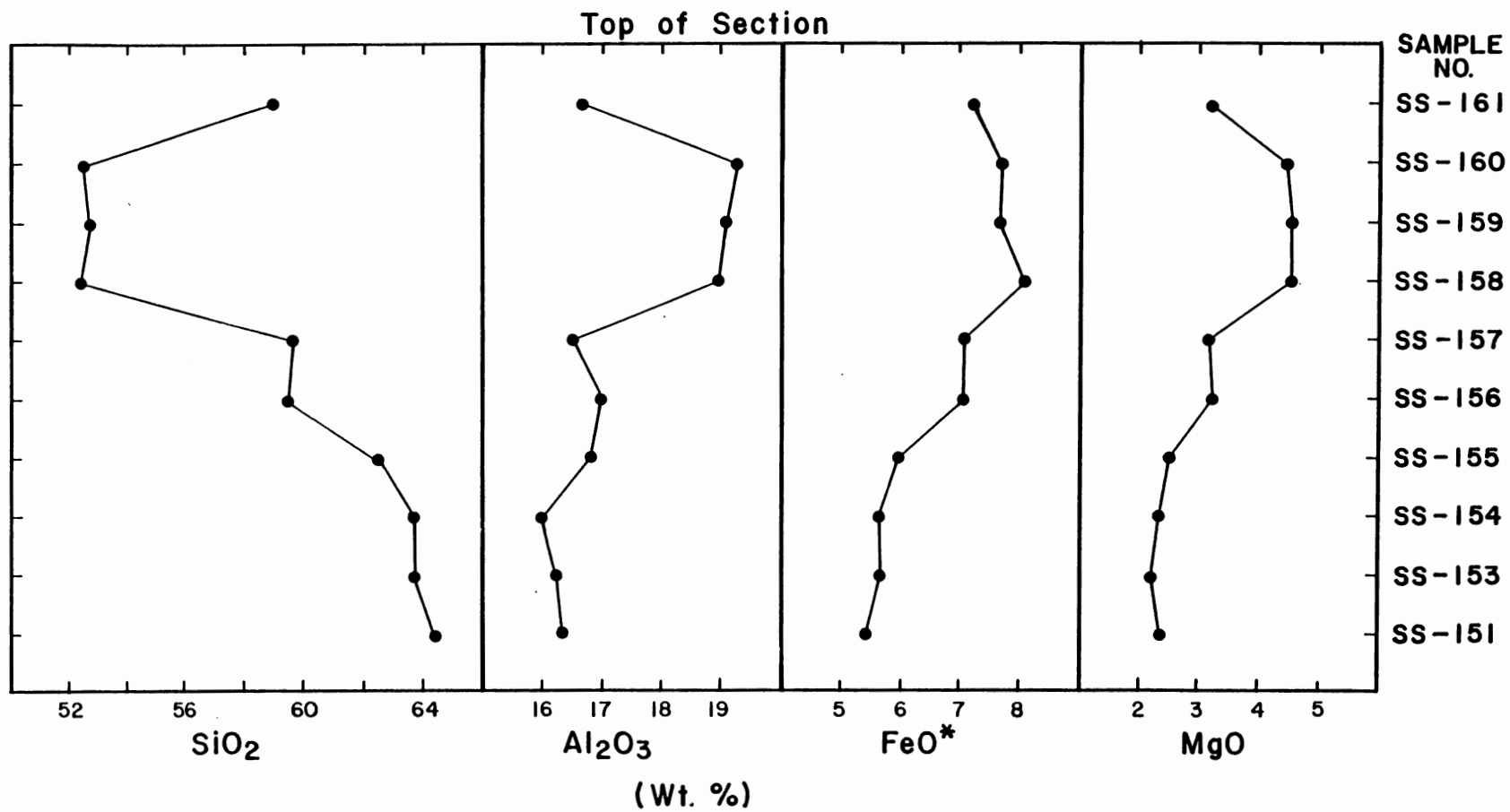


Figure 21. Compositional variation of main cone ( $Ps_{ad}$ ) lavas with stratigraphic position.

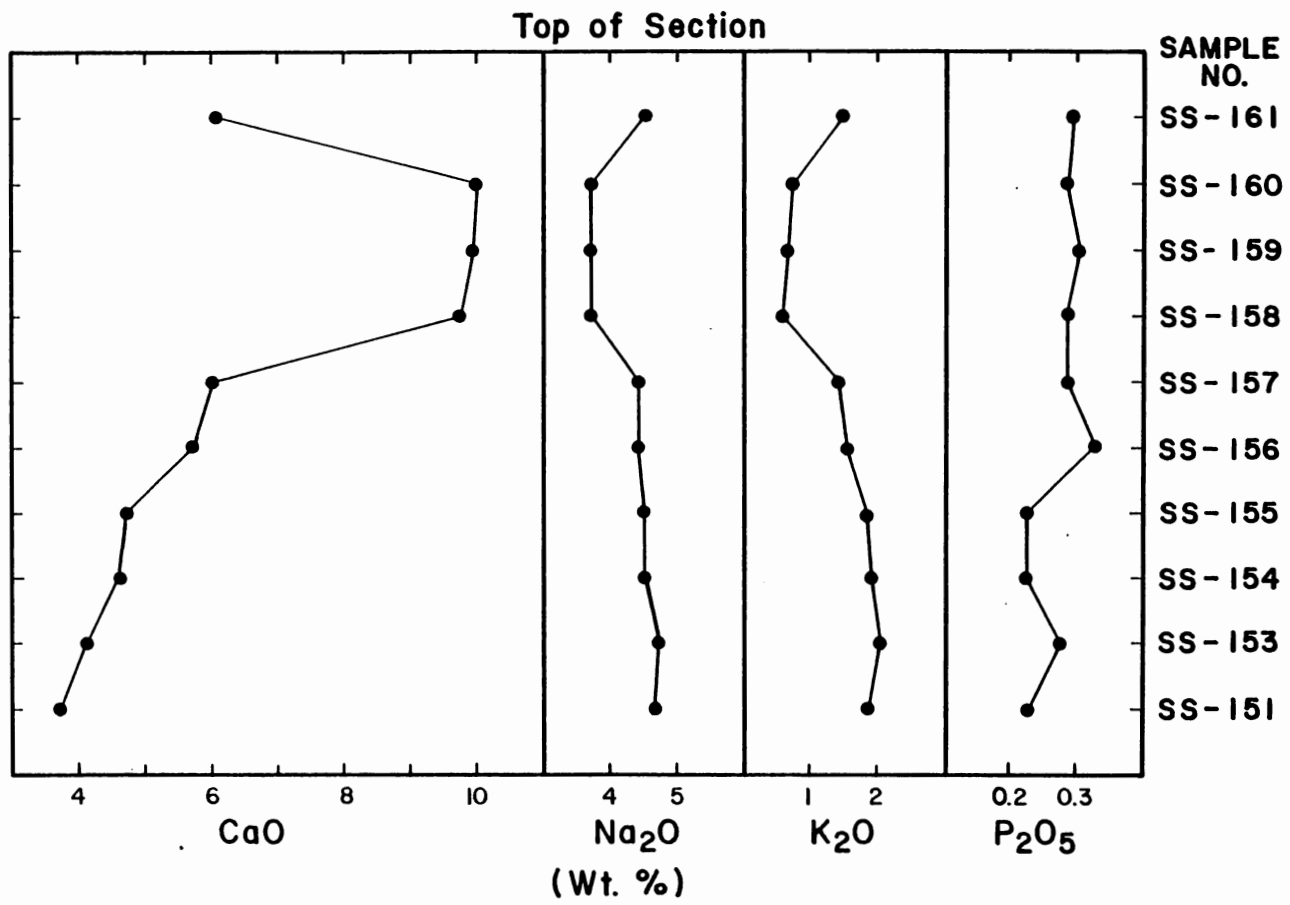


Figure 21. (Continued)

Top of Section

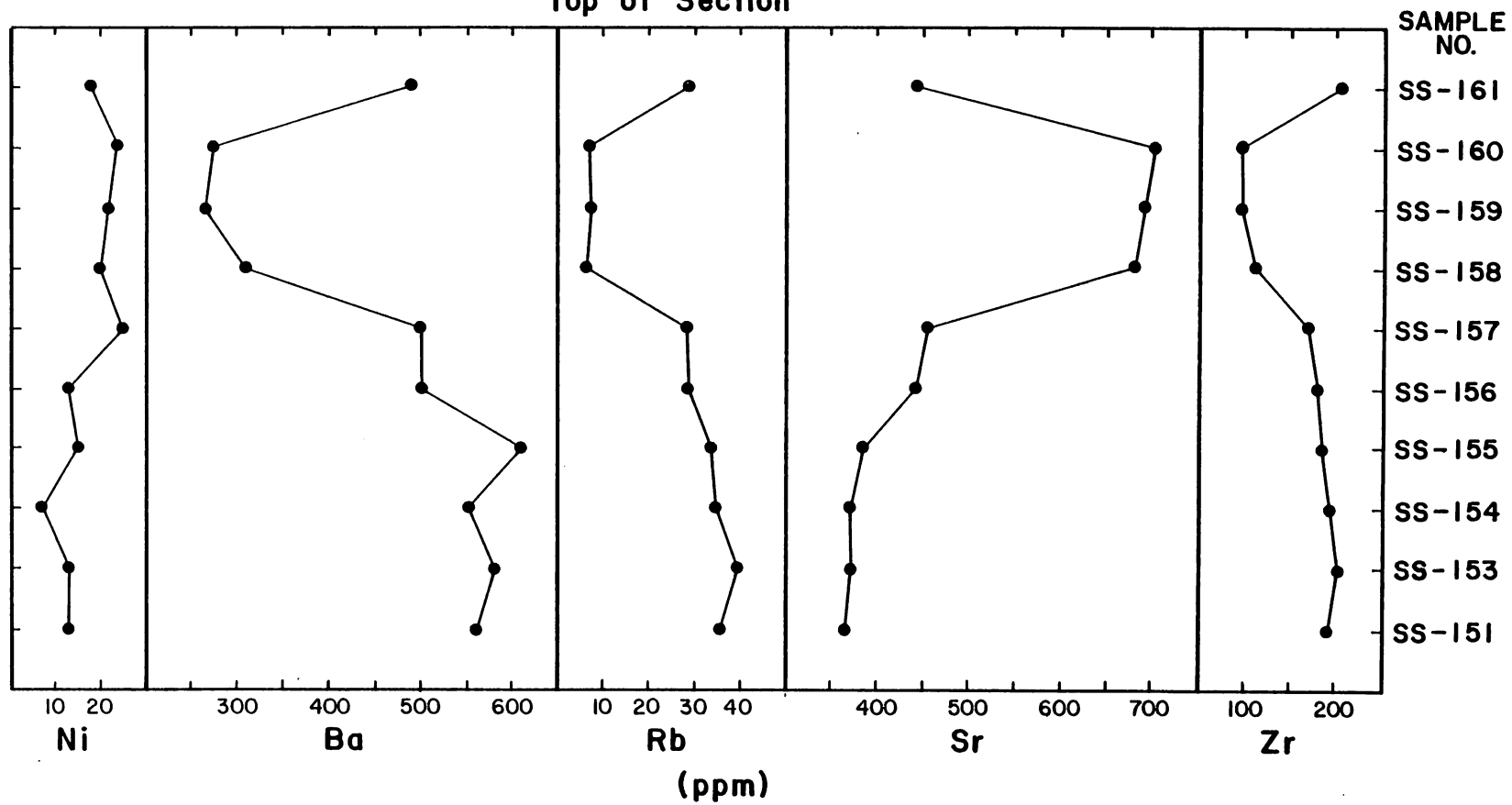


Figure 21. (Continued)

TABLE 2.

 $P_{s_{ad}}$  MAJOR AND TRACE ELEMENT FRACTIONATION MODELS

	MODEL #1		MODEL #2	
	<u>Parent</u>	<u>Daughter</u>	<u>Parent</u>	<u>Daughter</u>
	SS-160	SS-161	SS-161	SS-157
SiO <sub>2</sub>	52.53	58.87	58.87	59.46
TiO <sub>2</sub>	1.34	1.54	1.54	1.52
Al <sub>2</sub> O <sub>3</sub>	19.17	16.55	16.55	16.52
FeO	7.72	7.32	7.32	7.13
MnO	0.14	0.13	0.13	0.13
MgO	4.45	3.14	3.14	3.06
CaO <sub>2</sub>	9.98	6.13	6.13	5.96
Na <sub>2</sub> O	3.68	4.52	4.52	4.45
K <sub>2</sub> O	0.68	1.46	1.46	1.47
P <sub>2</sub> O <sub>5</sub>	0.28	0.29	0.29	0.28
$\Sigma r^2$	0.052		$\Sigma r^2$	0.017
Plagioclase (An <sub>56</sub> )	45.5	Plagioclase (An <sub>51</sub> )	2.6	
Clinopyroxene (En <sub>44</sub> )	11.8	Orthopyroxene (En <sub>68</sub> )	0.5	
Olivine (Fo <sub>66</sub> )	4.5	Clinopyroxene (En <sub>42</sub> )	0.4	
Titanomagnetite	3.6	Oxides	0.5	
Apatite	0.4	Apatite	0.1	
F	0.345	F	0.958	
Cumulative F	0.345	Cumulative F	0.331	

## Trace Elements

	<u>Predicted</u>	<u>Observed</u>	<u>Predicted</u>	<u>Observed</u>
Cr	0 - 15.9	14	4.6- 13.2	15
Ni	0.5- 16.6	18	15.8- 18.0	25
Zr	214 -261	179	184 -186	171
Rb	16.8- 20.0	28	28.9- 29.1	28
Sr	142 -952	441	416 -446	453
Ba	547 -761	491	503 -510	500

TABLE 2. (Continued)

	MODEL #3		MODEL #4	
	<u>Parent</u>	<u>Daughter</u>	<u>Parent</u>	<u>Daughter</u>
	SS-157	SS-155	SS-155	SS-153
SiO <sub>2</sub>	59.46	62.37	62.37	63.64
TiO <sub>2</sub>	1.52	0.97	0.97	1.16
Al <sub>2</sub> O <sub>3</sub>	16.52	16.76	16.76	16.12
FeO	7.13	6.06	6.06	5.73
MnO	0.13	0.12	0.12	0.11
MgO	3.06	2.45	2.45	2.16
CaO	5.96	4.72	4.72	4.10
Na <sub>2</sub> O	4.45	4.51	4.51	4.72
K <sub>2</sub> O	1.47	1.81	1.81	1.98
P <sub>2</sub> O <sub>5</sub>	0.28	0.22	0.22	0.27
$\Sigma r^2$	0.050		$\Sigma r^2$	0.024
Plagioclase (An <sub>51</sub> )		10.3	Plagioclase (An <sub>51</sub> )	9.3
Clinopyroxene (En <sub>42</sub> )		4.3	Orthopyroxene (En <sub>68</sub> )	1.9
Orthopyroxene (En <sub>68</sub> )		1.7	Clinopyroxene (En <sub>38</sub> )	0.7
Oxides		2.3	Oxides	0.5
Apatite		0.2	F	0.877
F		0.811	Cumulative F	0.235
Cumulative F		0.269		

## Trace Elements

	<u>Predicted</u>	<u>Observed</u>	<u>Predicted</u>	<u>Observed</u>
Cr	0.0- 9.4	7	0.3- 6.2	6
Ni	12.9- 23.7	15	10.6- 15.7	13
Zr	193 -206	187	207 -312	202
Rb	33.2- 34.4	33	37.0- 37.9	39
Sr	363 -493	383	309 -398	368
Ba	573 -608	610	663 -694	579

TABLE 2. (Continued)

MODEL #5		
	<u>Parent</u>	<u>Daughter</u>
	SS-155	SS-151
SiO <sub>2</sub>	62.37	64.35
TiO <sub>2</sub>	0.97	0.99
Al <sub>2</sub> O <sub>3</sub>	16.76	16.29
FeO	6.06	5.53
MnO	0.12	0.11
MgO	2.45	2.33
CaO	4.72	3.65
Na <sub>2</sub> O	4.51	4.64
K <sub>2</sub> O	1.81	1.88
P <sub>2</sub> O <sub>5</sub>	0.22	0.22
$\Sigma r^2$		0.023
Plagioclase (An <sub>56</sub> )		8.5
Clinopyroxene (En <sub>38</sub> )		2.4
Orthopyroxene (En <sub>68</sub> )		0.3
Oxides		0.9
F		0.876
Cumulative F		0.235

## Trace Elements

	<u>Predicted</u>	<u>Observed</u>
Cr	0.2- 5.5	6
Ni	10.3- 14.6	13
Zr	204 -211	195
Rb	36.7- 37.5	35
Sr	314 -397	366
Ba	660 -688	562

parental basalt. Similarly, fractionation of PL + CPX + OPX + Oxides + AP from an andesitic liquid can explain the observed variations from andesite to dacite. The compositions and proportions of subtracted phases are in general accord with modal abundances (Appendix A).

Although the major element fractionation models give acceptable solutions, trace element data do not support four of the five models. Rb is anomalously enriched, relative to predicted abundances, in two of the models, while Ba and Zr are depleted, relative to predicted abundances in four of the models. Only Model 3 is internally consistent with regard to both major and trace element abundances. The data indicate that fractional crystallization can explain only part of the smooth major and trace element variations in the main cone sequence.

#### Summit Basaltic Andesites ( $Ps_{ba}$ )

The capping lavas of the summit cone have the same range of variation as the main cone, but basaltic andesites predominate. The section selected for study consists of nine flows collected from the cirque above Clark Glacier, immediately southwest of the summit. Major and trace element variations with stratigraphic position are plotted in Figure 22. The rocks range from basaltic andesite to dacite and exhibit a cyclical pattern in which the basaltic andesites become more mafic and the differentiated rocks

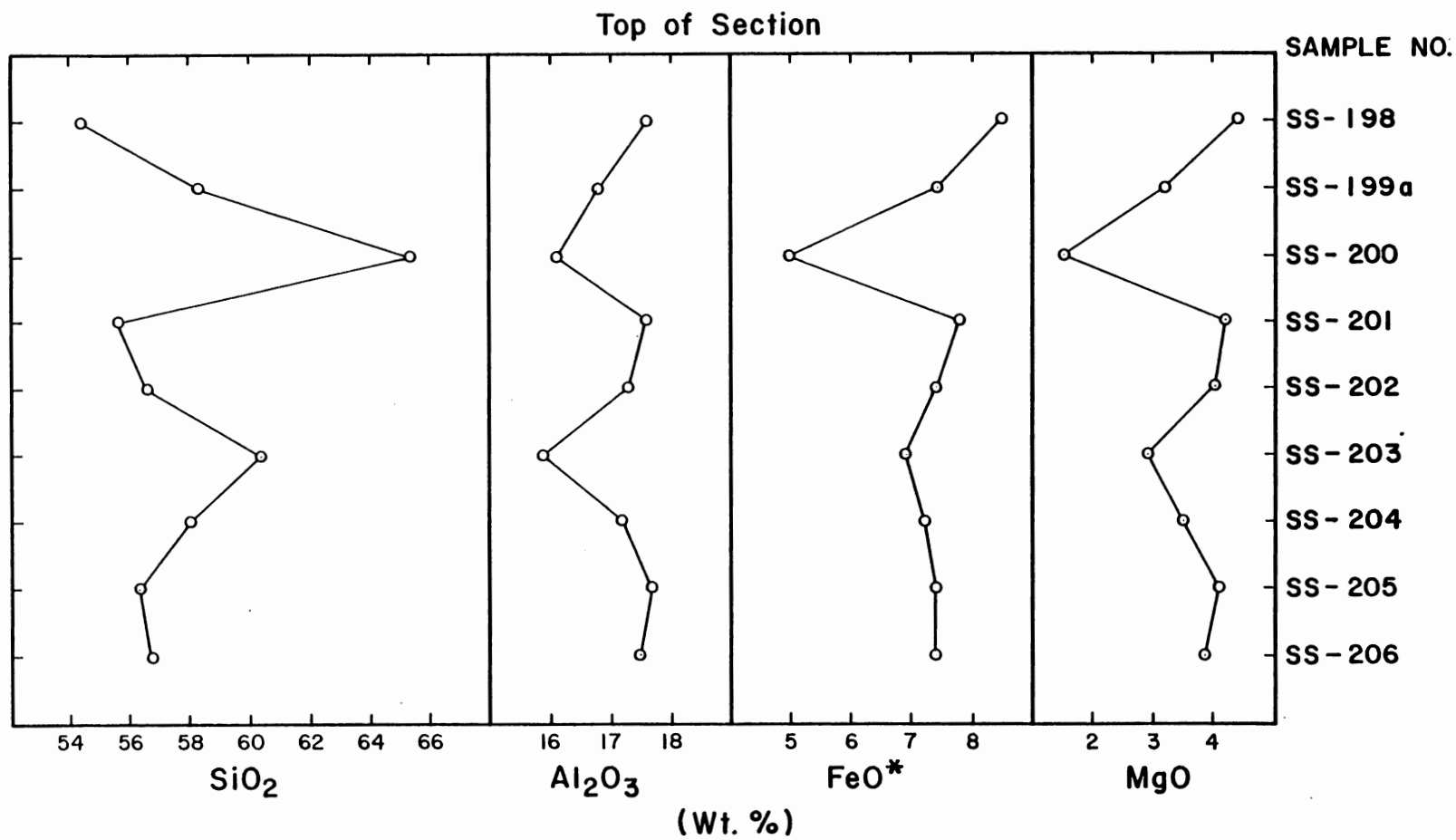


Figure 22. Compositional variation of summit cone (Ps<sub>ba</sub>) lavas with stratigraphic position.

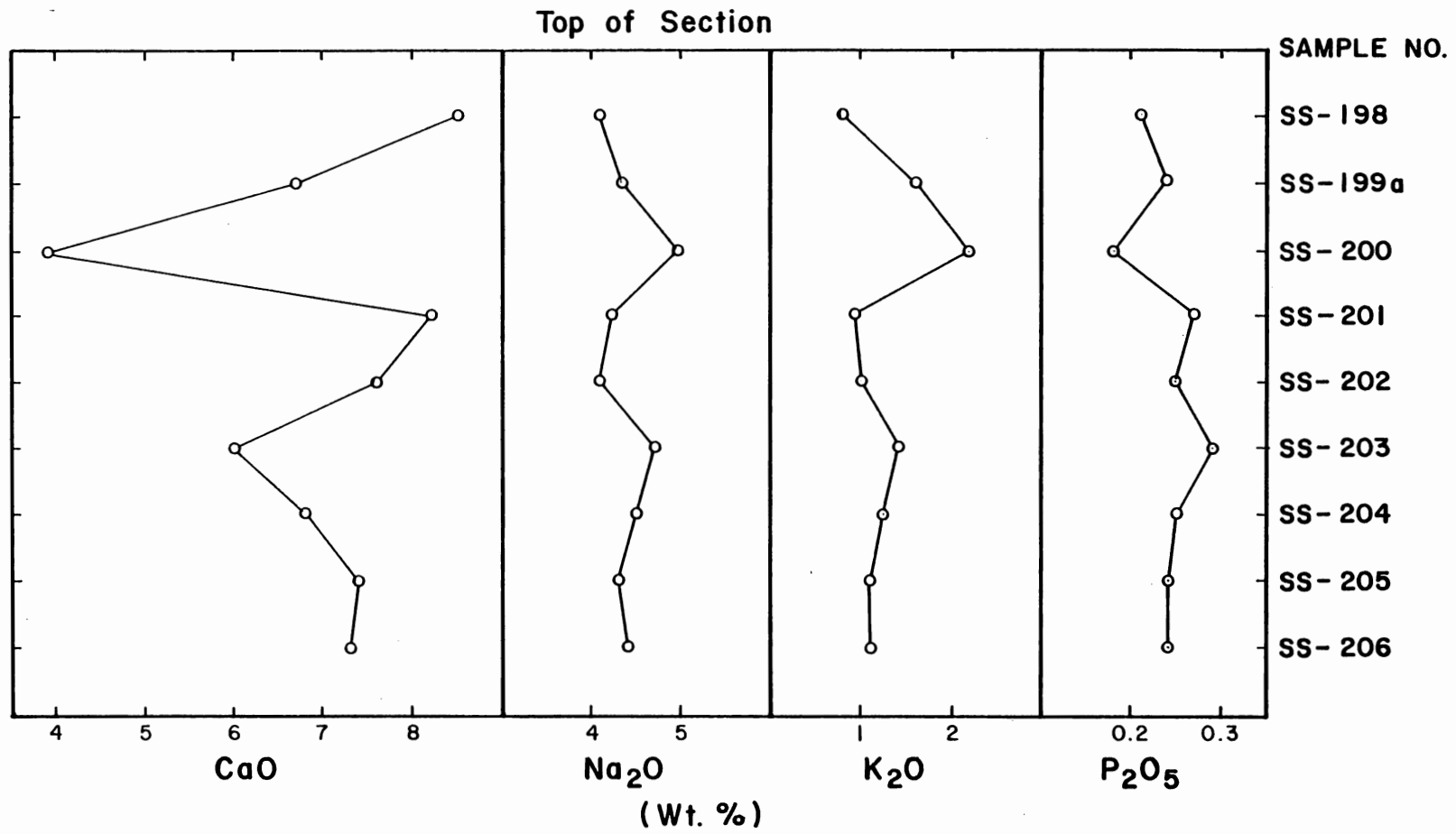


Figure 22. (Continued)

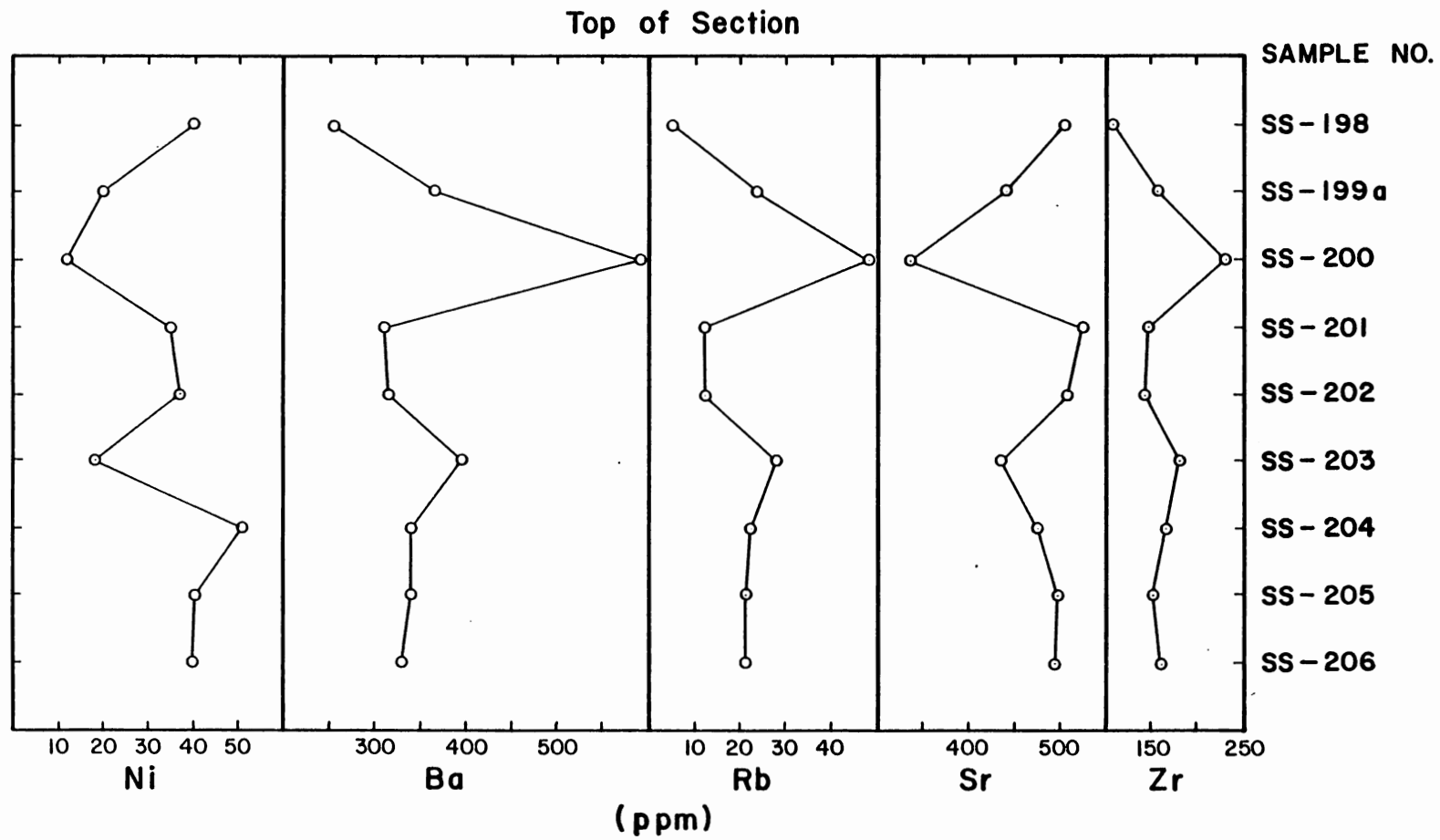


Figure 22. (Continued)

more silicic with time.

Six models of incremental fractional crystallization progressing from basaltic andesite to dacite were tested for the summit cone sequence. These are listed in Table 3, along with predicted and observed trace element abundances. The major-element mixing models again yield exceptionally good fits, with  $\Sigma r^2$  less than 0.07 in all cases. The data show that fractionation of the multiphase assemblage, OL + CPX + PL + MT ± AP, is capable of producing andesitic compositions from a parental basaltic andesite. Dacitic compositions can be generated by fractionation of PL + OPX + CPX + Oxides + AP from parental andesite. Phase compositions and proportions are in accord with modal data from the summit cone sequence (Appendix A).

On the basis of the same trace-element arguments used to reject four of five fractionation models calculated for the main cone ( $Ps_{ad}$ ) sequence, all the fractionation models for the summit cone ( $Ps_{ba}$ ) must be similarly rejected. Model 5 comes closest to a satisfactory solution, but the observed abundance of Zr is far too low relative to the predicted Zr abundance. Because Zr concentrations in these compositions are too low to stabilize zircon crystallization (Watson, 1979), zircon fractionation can be ruled out, and this model, too, must be rejected. Fractional crystallization alone, therefore, cannot reproduce both major and

TABLE 3.

Ps<sub>ba</sub> MAJOR AND TRACE ELEMENT FRACTIONATION MODELS

	MODEL #1		MODEL #2	
	<u>Parent</u>	<u>Daughter</u>	<u>Parent</u>	<u>Daughter</u>
	SS-198	SS-201	SS-201	SS-202
SiO <sub>2</sub>	54.31	55.45	55.45	56.61
TiO <sub>2</sub>	1.40	1.23	1.23	1.41
Al <sub>2</sub> O <sub>3</sub>	17.54	17.56	17.56	17.22
FeO	8.61	7.90	7.90	7.56
MnO	0.15	0.14	0.14	0.13
MgO	4.39	4.16	4.16	4.03
CaO	8.48	8.16	8.16	7.63
Na <sub>2</sub> O	4.07	4.18	4.18	4.15
K <sub>2</sub> O	0.80	0.90	0.90	0.97
P <sub>2</sub> O <sub>5</sub>	0.21	0.27	0.27	0.25
$\Sigma r^2$	0.001		$\Sigma r^2$	0.065
Plagioclase (An <sub>53</sub> )		7.2	Plagioclase (An <sub>53</sub> )	9.5
Clinopyroxene (En <sub>43</sub> )		2.7	Clinopyroxene (En <sub>43</sub> )	2.3
Olivine (Fo <sub>81</sub> )		1.7	Olivine (Fo <sub>81</sub> )	1.4
Titanomagnetite		0.7	Titanomagnetite	0.8
F		0.879	F	0.861
Cumulative F		0.879	Cumulative F	0.757

## Trace Elements

	<u>Predicted</u>	<u>Observed</u>	<u>Predicted</u>	<u>Observed</u>
Cr	0.6- 46.9	54	1.4- 43.0	49
Ni	19.7- 35.7	35	19.3- 33.0	37
Zr	114 -120	145	161 -166	139
Rb	5.6- 5.7	13	14.7- 15.1	12.3
Sr	434 -534	523	418 -546	508
Ba	275 -286	309	339 -355	313

TABLE 3. (Continued)

	MODEL #3		MODEL #4	
	<u>Parent</u>	<u>Daughter</u>	<u>Parent</u>	<u>Daughter</u>
	SS-201	SS-206	SS-206	SS-204
SiO <sub>2</sub>	55.45	56.65	56.65	57.95
TiO <sub>2</sub>	1.23	1.21	1.21	1.15
Al <sub>2</sub> O <sub>3</sub>	17.56	17.50	17.50	17.16
FeO	7.90	7.54	7.54	7.29
MnO	0.14	0.14	0.14	0.13
MgO	4.16	3.92	3.92	3.50
CaO	8.16	7.32	7.32	6.80
Na <sub>2</sub> O	4.18	4.37	4.37	4.50
K <sub>2</sub> O	0.90	1.08	1.08	1.24
P <sub>2</sub> O <sub>5</sub>	0.27	0.24	0.24	0.25
$\Sigma r^2$	0.007		$\Sigma r^2$	0.012
Plagioclase (An <sub>53</sub> )		9.6	Plagioclase (An <sub>50</sub> )	11.9
Clinopyroxene (En <sub>43</sub> )		4.4	Clinopyroxene (En <sub>40</sub> )	2.2
Olivine (Fo <sub>81</sub> )		1.4	Olivine (Fo <sub>70</sub> )	2.0
Titanomagnetite		0.5	Titanomagnetite	0.9
F		0.843	F	0.829
Cumulative F		0.741	Cumulative F	0.614

## Trace Elements

	<u>Predicted</u>	<u>Observed</u>	<u>Predicted</u>	<u>Observed</u>
Cr	0.1- 34.5	73	2.9- 62.4	36
Ni	17.3- 31.2	40	17.8- 37.4	21
Zr	162 -169	159	184 -190	163
Rb	15.0- 15.4	21	24.5- 25.2	22
Sr	423 -557	493	371 -520	474
Ba	345 -363	331	372 -394	338

TABLE 3. (Continued)

	MODEL #5		MODEL #6	
	<u>Parent</u>	<u>Daughter</u>	<u>Parent</u>	<u>Daughter</u>
	SS-204	SS-203	SS-203	SS-200
SiO <sub>2</sub>	57.95	60.31	60.31	65.20
TiO <sub>2</sub>	1.15	1.33	1.33	0.85
Al <sub>2</sub> O <sub>3</sub>	17.16	15.87	15.87	16.05
FeO	7.29	7.02	7.02	5.04
MnO	0.13	0.13	0.13	0.09
MgO	3.50	2.89	2.89	1.54
CaO	6.80	6.00	6.00	3.86
Na <sub>2</sub> O	4.50	4.69	4.69	4.95
K <sub>2</sub> O	1.24	1.44	1.44	2.23
P <sub>2</sub> O <sub>5</sub>	0.25	0.29	0.29	0.18
$\Sigma r^2$	0.017		$\Sigma r^2$	0.002
Plagioclase (An <sub>56</sub> )		17.9	Plagioclase (An <sub>39</sub> )	22.6
Orthopyroxene (En <sub>70</sub> )		4.9	Clinopyroxene (En <sub>41</sub> )	7.2
Clinopyroxene (En <sub>50</sub> )		0.4	Orthopyroxene (En <sub>60</sub> )	4.2
Oxides		0.7	Oxides	2.9
Apatite		0.1	Apatite	0.4
F		0.755	F	0.628
Cumulative F		0.464	Cumulative F	0.291

## Trace Elements

	<u>Predicted</u>	<u>Observed</u>	<u>Predicted</u>	<u>Observed</u>
Cr	0.1- 30.0	23	0.0- 9.3	15
Ni	10.6- 23.9	19	4.7- 18.0	12
Zr	203 -214	178	244 -273	231
Rb	27.8- 29.0	28	41.2- 44.3	48
Sr	303 -510	436	245 -516	333
Ba	400 -438	394	532 -610	591

trace element variations in either summit cone ( $Ps_{ba}$ ) or main cone ( $Ps_{ad}$ ) sequences.

### Discussion

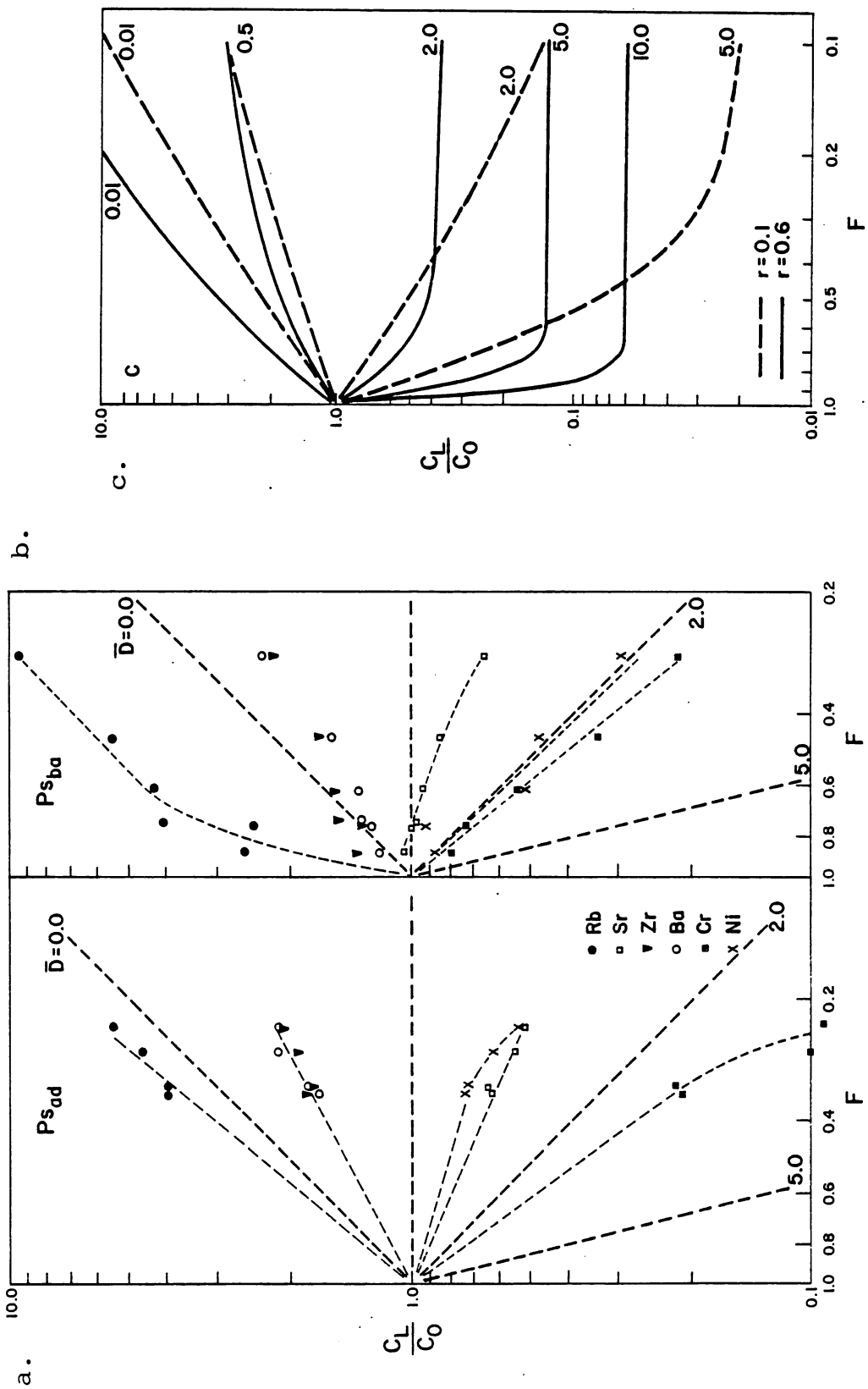
The lack of agreement between predicted and observed trace element abundances forms the primary basis upon which we must reject a simple, closed-system crystal fractionation model to explain chemical variations in the main and summit cone lavas. The trace element variations are best illustrated by plotting ratios of the concentration of an element in a differentiated liquid relative to that of the associated "parental" basalt versus the fraction of liquid remaining (F) calculated from the fractionation models. This has been done in Figure 23, a and b. The dashed lines in Figure 23 are idealized trends at given values of the bulk distribution coefficient,  $\bar{D}$ .  $\bar{D}$ 's can be estimated for each element by rearrangement of the Rayleigh law equation:

$$\bar{D} = [\ln (CL/CO) / \ln F] + 1.$$

The most striking feature of the data is the anomalous enrichment of Rb in the differentiated rocks. Observed Rb abundances in the main and summit cone sequences are higher than predicted if only closed-system crystal fractionation was operable, even if Rb was totally excluded from the crystallizing phases ( $\bar{D} = 0.0$ ). Similar anomalous Rb enrichment has been noted for suites of rocks from Yamsay Mountain, Oregon (Hering, 1981), and the Wooley Creek

Figure 23. Ratio of trace element concentration in a differentiated liquid ( $C_L$ ) to that in an assumed parental basalt ( $C_0$ ) plotted versus the fraction of liquid remaining ( $F$ ).

- a. Main cone sequence ( $Ps_{ad}$ ). Heavy dashed lines show Rayleigh fractionation trends for different values of the bulk distribution coefficient ( $D$ ). Light dashed lines show the trends for the South Sister lavas.
- b. Summit cone sequence ( $Ps_{ba}$ ).
- c. Theoretical trends for steady-state magma mixing (O'Hara, 1977) or combined assimilation-fractional crystallization (De Paolo, 1981) with different mass ratios ( $r$ ) of either fractionated crystals to input of fresh magma, or assimilated wallrock to fractionated crystals. See text for explanation.



batholith, California (Barnes, 1982). Zr displays similar anomalous enrichment in the summit cone sequence for values of  $F$  greater than 0.6. For  $F < 0.6$  Zr behaves as a moderately excluded element, along with Ba and K. Included element ratios (Ni, Cr, Sr) drop off rapidly according to their individual  $\bar{D}$  values.

We can consider several processes capable of generating the anomalous Rb enrichment in the differentiated rocks. The first is partial melting (Hering, 1981) and is discussed in the next section. Steady-state magma mixing (i.e. a fixed ratio of crystallization to input of fresh magma) or wall rock assimilation-fractional crystallization (AFC) (i.e. a fixed ratio of assimilated wall rock to crystals fractionating from the parent magma) will produce the same effect and both processes may result in the same characteristic trace element signatures (O'Hara, 1977; De Paolo, 1981). Theoretical trends for steady-state assimilation-fractional crystallization with mass ratios ( $r$ ) equal to 0.1 and 0.6 ( $r$  = mass of assimilated wall rock/mass of crystals fractionated from the parent magma) are illustrated in Figure 23c, along with expected trends for fractional crystallization only (De Paolo, 1981). It is apparent from Figure 23c that both the AFC process and steady-state magma mixing result in anomalous enrichments of both excluded and included elements in differentiated liquids. The included elements,

Sr, Ni, and Cr, in main and summit cone lavas are not enriched anomalously, and it is unlikely that either process played a major role in differentiation of South Sister magmas. Although the data presented in Figures 21 and 22 are consistent with periodic recharge of main and summit cone chambers, mixing between successive magma batches was apparently very limited in extent.

#### Physical Considerations

Geochemical arguments discussed above apparently rule out fractional crystallization and steady-state AFC and magma mixing as dominant processes within South Sister magma chambers. We can also consider the validity of fractional crystallization from a physical standpoint.

Estimates of pre-eruption temperatures for South Sister andesites were made using the 2-pyroxene geothermometer of Wells (1977) and the plagioclase geothermometer (Kudo and Weill, 1970). The plagioclase geothermometer can also be used to estimate  $P_{H_2O}$  if the temperature is determined independently (Kudo and Weill, 1970; Ritchev, 1979). Temperatures calculated using the 2-pyroxene geothermometer hover around 1100°C and are in close agreement with the temperatures calculated from plagioclase-liquid equilibria under dry conditions (Table 4). This accordance lends qualitative support to the conclusion reached earlier from phase relations that the main and summit cone magmas

TABLE 4.

TEMPERATURE, DENSITY AND VISCOSITY OF REPRESENTATIVE SAMPLES  
FROM MAIN ( $Ps_{ad}$ ) AND SUMMIT ( $Ps_{ba}$ ) LAVAS

a. Temperature

SS-154 ( $Ps_{ad}$ )

$T = 1114^{\circ}C$  (2-pyroxene geothermometer - Wells, 1977)

$T_{dry} = 1112^{\circ}C$  (Plagiocalse geothermometer - Kudo and Weill, 1970)

$T_{0.5 \text{ Kb}} = 1064^{\circ}C$

$T_{1.0 \text{ Kb}} = 1022^{\circ}C$

SS-200 ( $Ps_{ba}$ )

$T = 1053^{\circ}C$

$T_{dry} = 1060^{\circ}C$

$T_{0.5 \text{ Kb}} = 1014^{\circ}C$

$T_{1.0 \text{ Kb}} = 969^{\circ}C$

b. Density (1 Kb,  $1100^{\circ}C$ , 2%  $H_2O$ ) (Bottinga and Weill, 1970)

SS-151 ( $Ps_{ad}$ )

$\rho = 2.36$

SS-161 ( $Ps_{ad}$ )

$\rho = 2.42$

c. Viscosity (1 Kb,  $1100^{\circ}C$ , 2%  $H_2O$ ) (Shaw, 1972)

SS-151 ( $Ps_{ad}$ )

Log Viscosity = 4.14

SS-161 ( $Ps_{ad}$ )

Log Viscosity = 3.47

comprised a system relatively low in H<sub>2</sub>O.

The viscosity and density of a South Sister andesite were calculated using the procedures of Shaw (1972) and Bottinga and Weill (1970), and with the temperature derived from the pyroxene and plagioclase geothermometers (1100°C). Water content and pressure were set arbitrarily at 2 weight percent and 1 kilobar, respectively. The results appear in Table 4. Stokes settling velocities calculated using the information in Table 4 suggest that average size (1 to 2 mm diameter) plagioclase, clinopyroxene, and orthopyroxene phenocrysts would settle through a static magma body of 4 kilometers vertical dimension in a geologically reasonable period of time (<100 years).

It has been suggested, however, that magmas behave as non-Newtonian fluids, and that the finite yield strength of the liquid must be exceeded before crystal settling can occur (Murase and McBirney, 1973; McBirney and Noyes, 1979). Measured values of the yield strengths of andesitic liquids which have crystallized their principal phases are on the order of  $10^4$  dynes cm<sup>-2</sup> (Murase and McBirney, 1973), and no reasonable combination of density contrast and crystal size in South Sister andesites will exceed this threshold stress. This physical argument thus supports the conclusion reached on a geochemical basis that fractional crystallization is unlikely to have produced the spectrum of rock types present in the main and summit cone sequences

at South Sister.

### Partial Melting

In the case of extreme fractionation of the kind documented for certain alkaline systems (Baker, et al, 1977), fractional crystallization can produce stronger enrichments of incompatible trace elements than can partial melting (Baker, 1978). In calc-alkaline suites, however, rhyodacitic residual liquids may be generated by less than 80% fractionation from a basaltic parent (Ritchey, 1979; Ritchey, 1980). For elements with low values of the bulk distribution coefficient ( $\bar{D}$ ), partial melting has a greater effect on concentrations in residual liquids than does partial melting (Hanson, 1978). Small degrees of partial melting (<20%) can produce stronger enrichments of incompatible trace elements relative to a source rock than can moderate amounts of fractional crystallization ( $0.25 < F < 1.0$ ) from a parental liquid (Hanson, 1978; Arth, 1976).

The process of partial melting is difficult to quantify because of numerous assumptions one must make regarding T, P,  $P_{H_2O}$ , bulk and phase composition of the source rock, and the melting proportions. Lacking this information we can still discriminate between the relative importance of partial melting and fractional crystallization processes in explaining the chemical variance in a

comagmatic suite of rocks. The geochemical discriminants are based primarily on the disequilibrium (Rayleigh) nature of the crystal fractionation process versus the largely equilibrium (Nernst) behavior of source rocks and liquid during partial melting. Hanson (1978) has discussed the differential behavior of ratios of excluded elements to included elements during partial melting and fractional crystallization. A relatively small variation in included element abundances accompanying a large variation in excluded element abundances is diagnostic of partial melting, while the reverse holds true for fractional crystallization. The relationship determined by Hanson (1978) is illustrated in Figure 24, along with an Rb-Ni covariance diagram for the  $Ps_{ad}$  and  $Ps_{ba}$  stratigraphic sections discussed earlier. The steep negative slopes for the main and summit cone sections suggest that the suites may be related by progressive partial melting of some unspecified source rock, rather than by fractional crystallization from a basaltic magma, in accordance with the earlier conclusions based on trace element abundances in residual liquids.

A more useful geochemical discriminant was developed by Treuil (1973) and Treuil and Joron (1975). The method utilized the behavioral differences between totally excluded ( $\bar{D} \leq 0.01$ ), H (hypermagmatophile) elements and moderately excluded ( $0.1 \leq \bar{D} \leq 0.3$ ), M (magmatophile) elements.

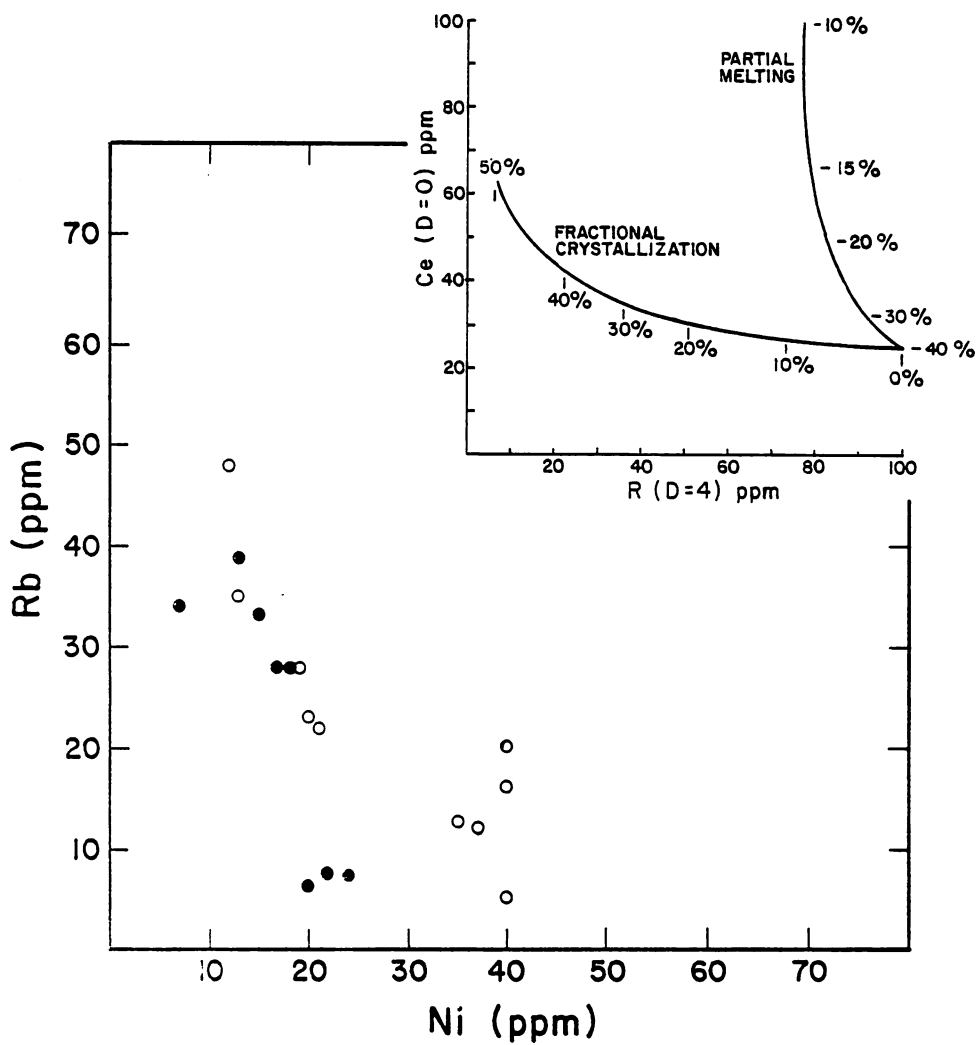


Figure 24. Rb versus Ni in main (Ps<sub>ad</sub>) and summit (Ps<sub>ba</sub>) cone lavas from the South Sister volcanic complex. Symbols are in Figure 8. Inset shows relationship determined by Hanson (1978) for partial melting and fractional crystallization processes.

Again, the assumption is made that partial melting is an equilibrium (Nernst) process, while fractional crystallization is a disequilibrium (Rayleigh) process. Plots of the ratio H/M versus H can be used to discriminate between partial melting and fractional crystallization processes (Treuil and Joron, 1975; Allegre and Minster, 1978; Hering, 1981). The following derivation of the method is taken from Allegre and Minster (1978):

During fractional crystallization the concentration of a trace element in residual liquids is given by the Rayleigh equation:

$$C_L = C_0 F^{(\bar{D}-1)} \quad , \quad \text{where}$$

$C_L$  = the concentration of an element in the residual liquid

$C_0$  = the concentration of the element in the parental liquid

$F$  = the fraction of residual liquid

$\bar{D}$  = the bulk distribution coefficient.

If  $\bar{D}$  is so small that it can be neglected relative to 1 for the excluded H and M elements, then

$$C_L^H \approx \frac{C_0^H}{F} \quad \text{and} \quad C_L^M \approx \frac{C_0^M}{F} \quad ,$$

where  $C_L^H$  = the concentration of the H element in the residual liquid

$C_0^H$  = the concentration of the H element in the parental liquid

$C_L^M$  = the concentration of the M element in the residual liquid, and

$C_O^M$  = the concentration of the M element in the parental liquid.

The ratio  $C_L^H/C_L^M \approx C_O^H/C_O^M$  is approximately constant, and a comagmatic suite of rocks related by fractional crystallization will plot along a horizontal line on a H/M vs. H diagram.

During batch partial melting the concentration of an element in the liquid is given by the Nernst equation:

$$C_L = C_O / [\bar{D} + F(1-\bar{D})] \quad , \text{ where}$$

$C_L$  = the concentration of an element in the liquid

$C_O$  = the concentration of the element in the initial solid

$\bar{D}$  = the bulk distribution coefficient, and

$F$  = the fraction of melting.

For H elements,  $\bar{D}_H \approx 0$ , and

$$C_L^H = C_O^H / F$$

For M elements,  $0 < \bar{D}_M \ll 1$ , and a good approximation of  $C_L^M$  is  $C_L^M \approx C_O^M / (\bar{D}_M + F)$ .

The ratio of the elements in the liquid is

$$C_L^H / C_L^M = \frac{C_O^H \cdot \bar{D}_M}{C_O^M \cdot F} + \frac{C_O^H}{C_O^M} \quad , \text{ and because}$$

$$C_L^H = C_O^H / F \quad , \quad C_L^H / C_L^M = (\bar{D}_M / C_O^M) \cdot C_L^H + C_O^H / C_O^M$$

On a  $C_L^H/C_L^M$  vs.  $C_L^H$  diagram, rocks related by partial melting should plot on a straight line with slope  $\bar{D}_M/C_O^M$  and a Y-intercept value equivalent to the ratio  $C^H/C^M$  in the source rocks. The behavior of the ratios  $C^H/C^M$  with increasing  $C^H$  during partial melting and fractional crystallization is illustrated in Figure 25, in part modified from Hering (1981). H elements in calc-alkaline rocks include Rb and Th, while Zr, Ba, and K are typical M elements.

Main and summit cone lavas exhibit diagnostic partial melting trends on H/M vs. H diagrams (Figure 25) and appear to represent approximately 2 to 20 percent batch partial melting of a source with a Rb/Zr ratio of 0.038. Extrapolated source area ratios of Rb/K and Rb/Ba are slightly different for the main and summit cone sequences, a possible indication that the source area for each group of lavas is geochemically distinctive.

The significant feature of these data is that fractional crystallization processes will not result in the observed rapid increase in excluded element ratios unless unreasonably high  $\bar{D}$ 's are assumed for the moderately excluded M elements. Figure 25 illustrates that the  $\bar{D}$  for Zr must equal 0.5 to reproduce the rate of increase of Rb/Zr ratios in South Sister main and summit cone rocks. No petrologically valid crystallizing assemblage in these

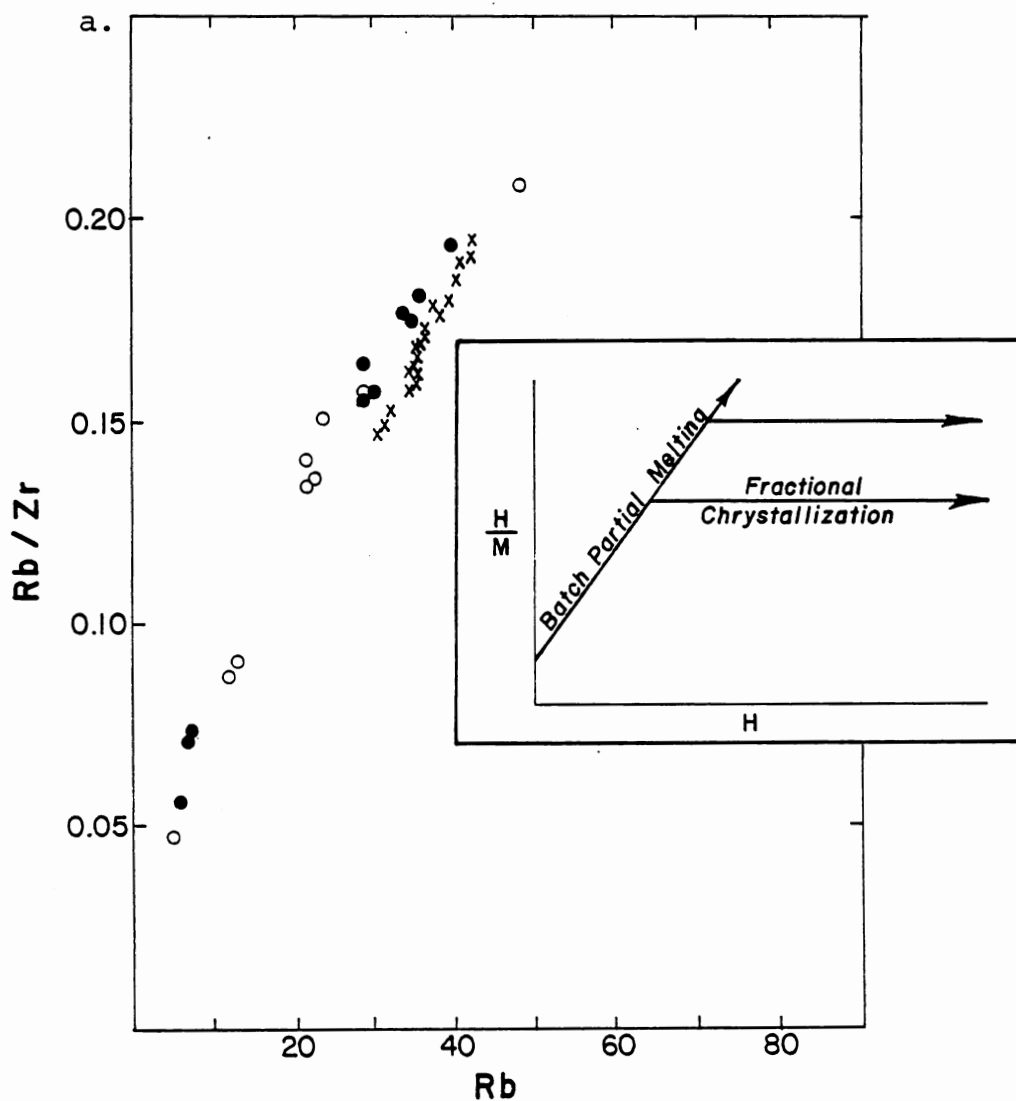


Figure 25. H/M versus H element plots. Inset in 25a shows theoretical trends for batch partial melting and fractional crystallization. Symbols as in Figure 8. See text for explanation.

a. Rb/Zr vs. Rb

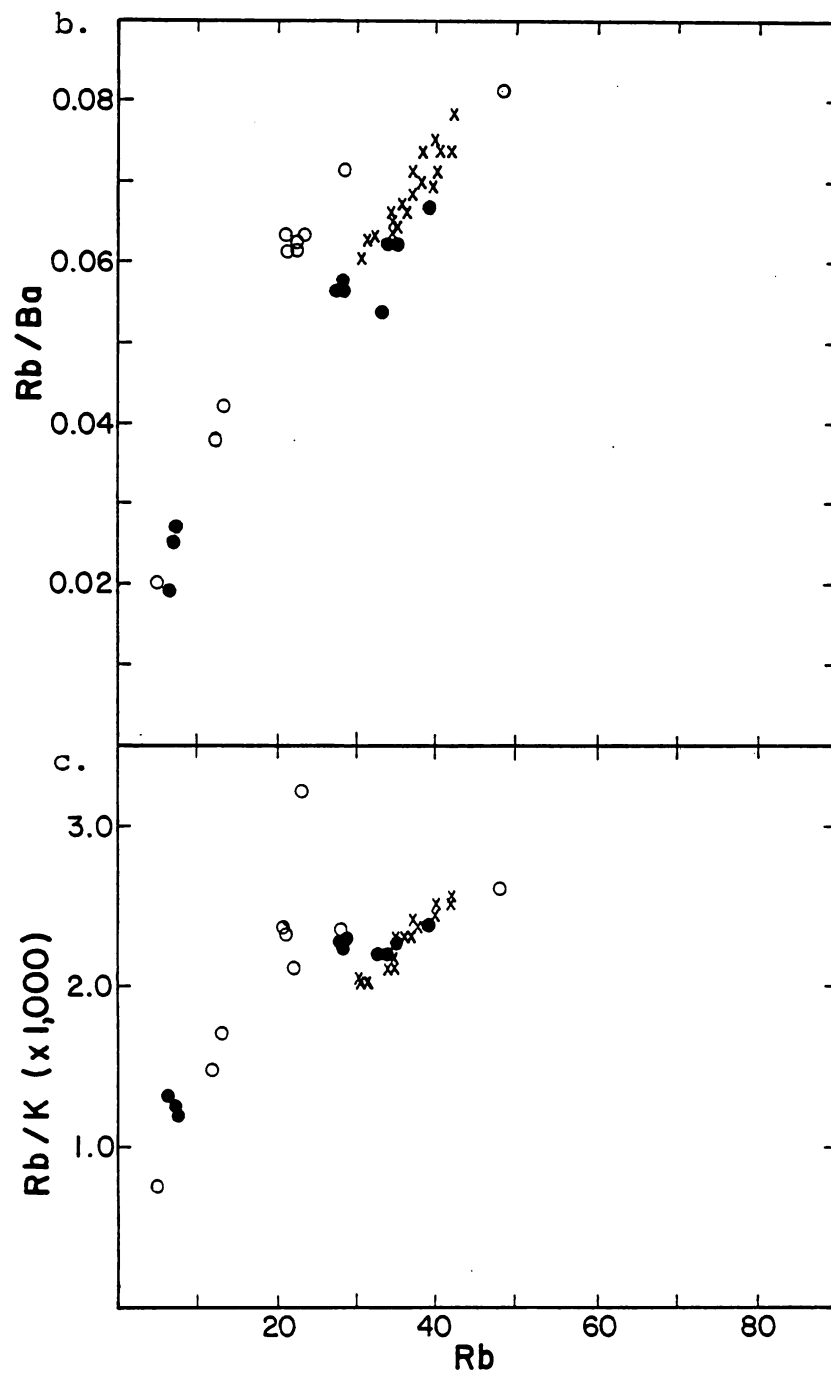


Figure 25. (Continued)

b. Rb/Ba vs. Rb

c. Rb/K vs. Rb

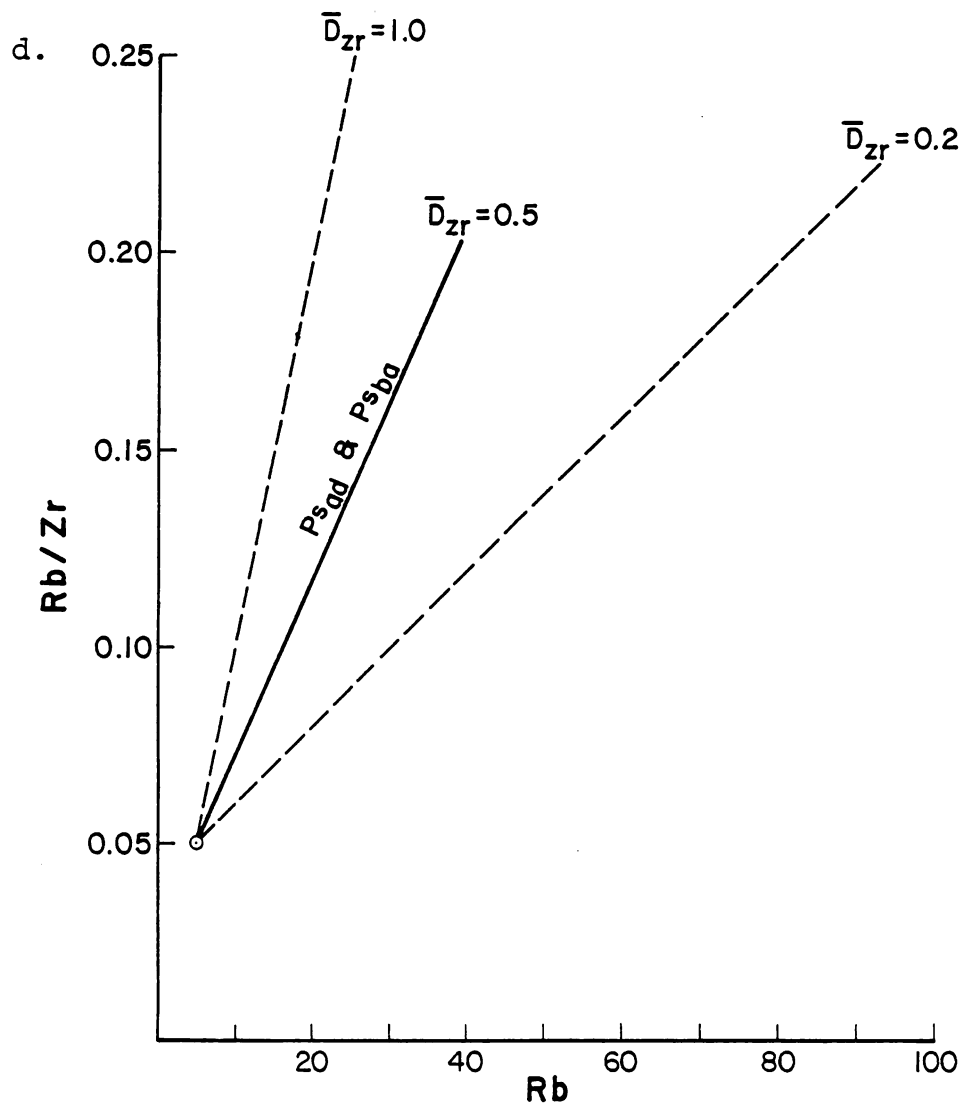


Figure 25. (Continued)

- d. Variation of Rb/Zr vs. Rb slope at different values of  $\bar{D}_{Zr}$ .  $Ps_{ad}$  and  $Ps_{ba}$  trends are shown for comparison.

rocks will result in a  $\bar{D}_{Zr}$  of 0.5. The same arguments apply for Ba and K as well. Strong enrichments of excluded elements in residual liquids are produced by small degrees of partial melting ( $F = 0.01$  to  $0.2$ ), while smaller changes in excluded element abundances occur over fractional crystallization intervals of  $F = 1.0$  to  $F = 0.25$ . The favored interpretation, therefore, is that the groups of lavas forming the main and summit cones of South Sister are linked primarily by progressive batch partial melting of similar, but slightly distinctive (with respect to Rb/Ba and Rb/K ratios), source rocks. This is not meant to imply that the sequences represent unmodified partial melts of mantle material. Fractionation models presented previously allow that some of the chemical variation owes its existence to shallow-level fractional crystallization. At deeper levels the expansion of the olivine ( $\pm$  spinel) stability field in a rising magma (Kushiro, 1979) must result in fractionation and subsequent differentiation of basaltic liquids. Lower viscosities and yield strengths of magmatic liquids at high pressures (Kushiro, Yoder and Mysen, 1976) may also remove the physical barriers to fractional crystallization alluded to in the last section. These factors may account for some of the scatter in Figure 25. Maintenance of the steep slopes on the Rb/Zr, Rb/Ba, and Rb/K versus Rb diagrams requires, however, that

the amount of deep-level fractionation remained approximately constant throughout the suite. The effect of constant deep-level fractionation on the diagrams in Figure 25 would be to shift the trend line in the direction of increasing Rb abundance with minimal slope change. The imprint of partial melting as the primary genetic link remains intact.

These data do not allow quantification of source rock composition and mineralogy; however, experimental evidence suggests that a spectrum of liquid compositions, from high-alumina basalt to silica-rich andesite, can coexist with reasonable mantle assemblages (OL + CPX + OPX) in the presence of pure H<sub>2</sub>O or an H<sub>2</sub>O-rich gas phase at a variety of pressures (Kushiro, 1972; Mysen and Boettcher, 1975).  $\bar{D}$ 's estimated from Figure 25 for Zr and Ba are too high if the segregated liquids equilibrated only with mantle peridotite containing olivine and pyroxenes. The anomalously high values of  $\bar{D}_{Zr}$  and  $\bar{D}_{Ba}$  suggest that the main and summit cone magmas of South Sister have equilibrated with a residual solid assemblage, either in the source area or enroute to the surface, which included a phase capable of retaining Zr and Ba. That residual phase would most likely be amphibole. Pearce and Norry (1979) have estimated that the distribution coefficient for Zr in amphibole in mafic bulk compositions ranges between 0.4 and 1.0. Likewise, the distribution coefficient for Ba in amphibole may be

as high as 0.7 in mafic compositions (Arth, 1976). Amphibole rejects Rb to a greater extent than K during melting (Arth, 1976), and this process may be reflected in the higher Rb/K ratios in rocks suspected of being derived from the smallest degrees of partial melting (Figure 25). Progressive batch partial melting can reproduce the quasi-linear trends on Harker diagrams (Kushiro, 1979), and the presence of amphibole in the crystalline residua will buffer the Fe/Mg ratio of the melt, minimize Fe-enrichment, and produce a calc-alkaline trend.

It is not likely that South Sister volcano was situated over a large, fractionating, calc-alkaline magma chamber. Rather, the data presented here support the existence of several smaller bodies of magma, into which were intruded discrete batches of magma with a variety of compositions, from basalt to dacite. Most of the compositional variation owes its existence to progressive batch partial melting, but the magmas may have been somewhat modified by deep-level and minor shallow-level fractional crystallization, and by limited wall-rock interaction enroute to the surface.

## CHAPTER 4

## ORIGIN OF THE DIVERGENT SUITE

Bimodal basalt-rhyodacite complexes comprise both the earliest ( $Ps_{ba}$ - $Ps_{rda}$ ) and latest ( $Ho_{bs}$ - $Ho_{rda}$ ) eruptive sequences associated with volcanic activity at South Sister. The temporal relationships of the basalts and rhyodacites, and the apparent scarcity of intervening lavas of intermediate composition, suggest that these bimodal suites are perhaps similar to those at Medicine Lake (Mertzman, 1977; Mertzman and Williams, 1981), Yamsay Mountain (Hering, 1981) and Crater Lake (Ritchey, 1979, 1980). Hypotheses introduced to explain bimodal suites include:

1. Efficient fractional crystallization from a basaltic parent (Ritchey, 1979, 1980; Baker et al, 1977).
2. Melting of crustal material by underplating basaltic magma (Ewart and Stipp, 1968; Sigurdsson, 1977; Lachenbruch and Sass, 1976; Hildreth, 1979, 1981; Bacon and Duffield, 1980).
3. Differential partial melting of a hydrous mantle

source (Kushiro, 1972; Kushiro et al, 1972; Yoder, 1973).

4. Liquid immiscibility (Philpotts, 1976; Watson, 1976; Ryerson and Hess, 1978).

Most geologic studies of bimodal associations favor the former two hypotheses (references cited in 1. and 2. above). Several studies indicate also that the rhyolitic rocks in bimodal suites may be generated by fractional crystallization from dacitic magmas produced by partial melting (Hering, 1981; Mertzman and Williams, 1981). Another factor in the petrogenesis of bimodal suites is the almost universal association of igneous bimodality with extensional tectonic regimes (Martin and Piwinskii, 1972; Lachenbruch and Sass, 1976; Baker et al, 1977).

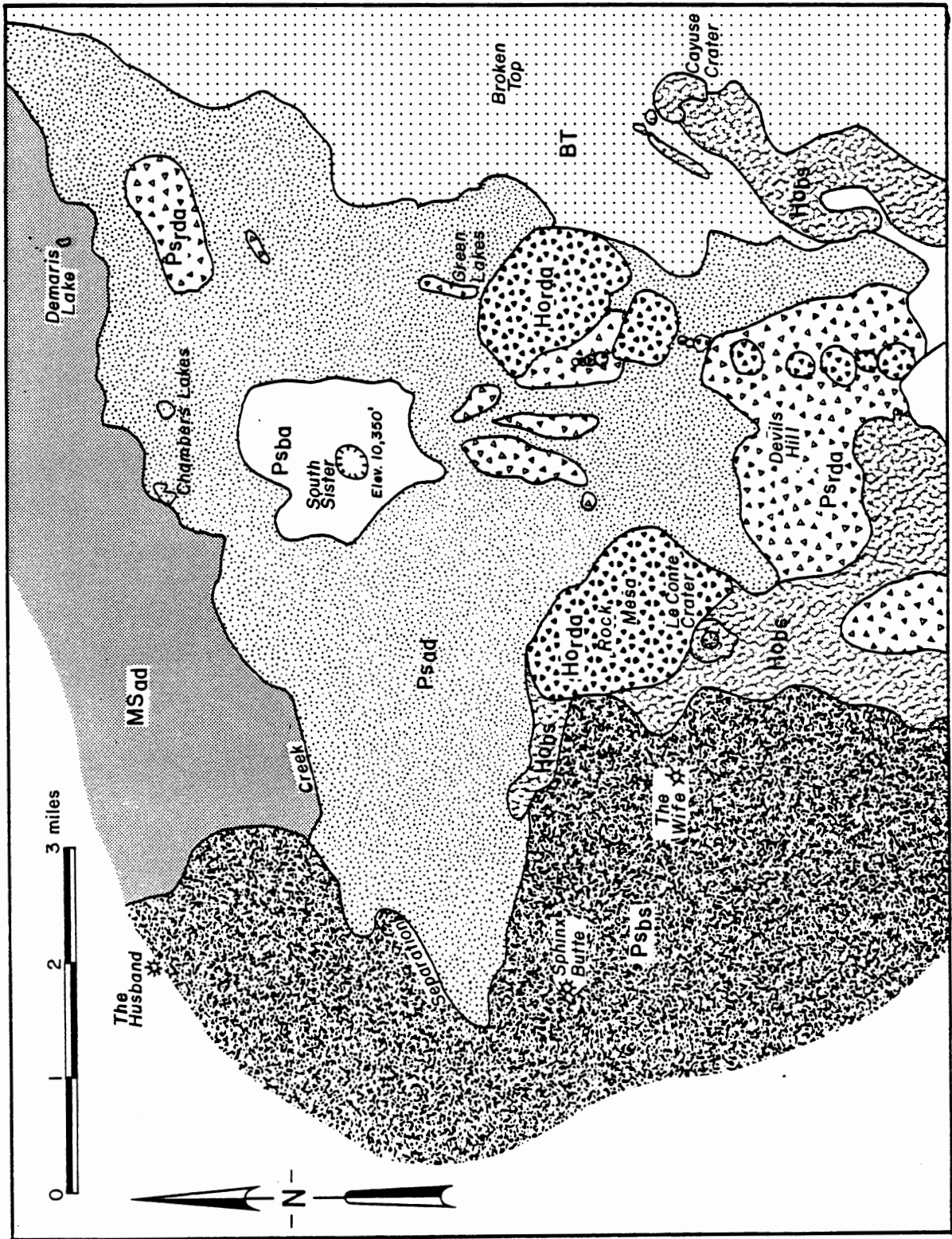
In this chapter I compile field, petrographic, geochemical, and phase equilibria data, along with calculated and estimated physical parameters, in order to develop an internally consistent physical model for the origin of the early and late-stage divergent magmas at South Sister volcano.

## Geology and Petrography

### Field Relationships

The geological relationships at South Sister volcano are summarized in the sketch map in Figure 26. Main and

Figure 26. Geological sketch map of South Sister volcano and vicinity.



summit cone lavas at South Sister are sandwiched between the early ( $Ps_{bs}$ - $Ps_{rda}$ ) and late ( $Ho_{bs}$ - $Ho_{rda}$ ) basalt-rhyodacite sequences. The early rhyodacites ( $Ps_{rda}$ ) underlie most of the eastern third of the volcanic edifice and extend from Kokostik Butte on the south to Demaris Lake on the north. Similar rocks crop out west of North Sister at Obsidian Cliffs. These rhyodacites were erupted following extensive basaltic volcanism ( $Ps_{bs}$ ) in the central High Cascades. The post-glacial rhyodacites ( $Ho_{rda}$ ) were erupted along an approximately north-trending fracture extending from Devil's Lake on the South to near the 8000 foot level on South Sister. The Rock Mesa flow (also  $Ho_{rda}$ ) erupted along a N70E vent alignment that may intersect the major north-south fracture. The post-glacial rhyodacites ( $Ho_{rda}$ ) are areally-restricted to terrain underlain by the early rhyodacites ( $Ps_{rda}$ ). Post-glacial basaltic cinder cones ( $Ho_{bs}$ ) ring the periphery of the area covered by the rhyodacites. Le Conte Crater lies closest to the rhyodacitic rocks. These basaltic rocks may be as much as 10,000 years older than the post-glacial rhyodacites according to Taylor (1978).

Time-composition-volume data given in Figure 7 summarize these geological relationships for South Sister. These data indicate that rhyodacitic rocks make up a volumetrically minor proportion of the total erupted rocks at

South Sister. In particular the early bimodal sequence ( $Ps_{bs}$ - $Ps_{rda}$ ) appears to have a ratio of basalts to rhyodacites of nearly 20:1. This relationship does not appear to persist in the post-glacial basalt-rhyodacite sequence if only the map area of Figure 26 (and Plate 1) is considered (Figure 7). However, the total volume of post-glacial basaltic rocks erupted within a 10 kilometer radius from the Newberry rhyodacite flow on the south flank of South Sister is in excess of  $30 \text{ km}^3$ , according to additional volumetric calculations. Most of these post-glacial basaltic rocks were erupted in the vicinity of Mt. Bachelor (Taylor, 1978). The post-glacial bimodal sequence ( $Ho_{bs}$ - $Ho_{rda}$ ) may, therefore, have a ratio of erupted basalts to erupted rhyodacites as high as 60:1.

### Petrography

#### Shield Basalts ( $Ps_{bs}$ )

The basalts and basaltic andesites of the pre-cone shield are ubiquitously olivine-phyric. Olivine phenocrysts ( $Fo_{85-80}$ ) are subhedral to resorbed, 1 to 2 mm in length, and make up 3 to 10 volume percent of the rock. Many olivines have inclusions of clear glass and cubic to octahedral, red-brown spinel. The glass inclusions may represent trapped magmatic liquid (Anderson, 1976), and rare pyroxene and plagioclase inclusions in the olivines

can probably be attributed to post-entrapment crystallization of this trapped melt. Olivine phenocrysts in more evolved shield lavas have rims of granular pyroxene. Plagioclase phenocrysts and microphenocrysts make up less than 5% of the rock and are generally less than 1 mm in length. The plagioclase crystals display weak patchy to concentric compositional zonation and range from  $An_{75}$  to  $An_{55}$  in composition. Trapped melt inclusions are also common in plagioclase phenocrysts and have minor post-entrapment pyroxene. Some plagioclase and olivine phenocrysts form glomerocrysts. The fine-grained, holocrystalline to glassy groundmass includes plagioclase, pyroxene (augite  $\pm$  pigeonite ?), olivine, titanomagnetite, apatite and brown glass. Most shield lavas are porphyritic and vesicular, but a wide variety of groundmass textures may be found. Observed textures include pilotaxitic, intergranular with minor intersertal glass, intersertal with minor intergranular pyroxene and olivine, intergranular with minor ophitic pyroxene, and rarely, seriate plagioclase laths. Groundmass plagioclase laths range from  $An_{55}$  to  $An_{45}$  in composition and commonly contain tiny needles of apatite. Groundmass glass may contain minute, acicular crystals of clinopyroxene.

#### Early Rhyodacites ( $Ps_{rda}$ )

The rhyodacitic lavas crop out as pale gray pumiceous,

medium-gray lithoidal, or dense, black obsidian varieties, but all have contorted flow banding. The glassy obsidian is somewhat perlitic and commonly contains pink to gray spherulites and lithophysae up to several centimeters in diameter. Lavas similar to the early rhyodacites at South Sister are also exposed at Obsidian Cliffs, northwest of Middle Sister.

The early rhyodacitic lavas contain less than 15% phenocrysts of plagioclase, orthopyroxene, Fe-Ti oxides, and rare hornblende set in a glassy to microcrystalline groundmass. Modal abundances of representative samples are listed in Appendix A. Plagioclase phenocrysts and microphenocrysts are euhedral to subhedral laths up to 3 mm in length. Zonation is oscillatory-normal or patchy, and the total compositional range is from  $An_{35}$  to  $An_{22}$ . Most zonation is in phenocrysts, while microphenocrysts are relatively unzoned. Inclusions of clear glass, pyroxene, magnetite, or apatite are rare. Marginal resorption of plagioclase phenocrysts is not common. Orthopyroxene microphenocrysts are euhedral to subhedral and less than 0.5 mm in length. They range in composition from  $En_{65}$  to  $En_{55}$  and commonly have thin, reversely-zoned rims. The orthopyroxene microphenocrysts are generally dispersed throughout the matrix, but also occur as monomineralic glomerocrysts, or in conjunction with plagioclase and/or

magnetite. Magnetite and ilmenite are present as microphenocrysts less than 0.2 mm in length. Rare zircon microphenocrysts are less than 0.15 mm in length. Holocrystalline, cognate xenoliths occur as rare, polycrystalline aggregates of plagioclase, orthopyroxene, and magnetite up to 1 cm in diameter. One inclusion has a peculiar "hornfelsic" texture (Figure 4). The xenoliths may represent the products of crystallization at the walls of a magma chamber. The dark, glassy groundmass shows contorted flow banding and radial, spherulitic devitrification, and contains microlites of orthopyroxene and sodic plagioclase. Vesicles are commonly filled with a silica mineral, probably cristobalite.

#### Post-glacial Basalts (Ho<sub>bs</sub>)

The olivine basalt flows from Cayuse Crater and nearby centers contain phenocrysts of olivine in a pilotaxitic network of plagioclase laths, granular pyroxene and olivine, and intersertal glass. Olivine phenocrysts and microphenocrysts (Fo<sub>88-80</sub>) are subhedral and up to 1.5 mm in length. The olivines occur as discrete phenocrysts and glomerophytic aggregates of from two to four crystals. Inclusions of cubic, red-brown, chromian spinel are common. Several olivine phenocrysts show marginal resorption and thin, granular reaction coronas of pyroxene. Groundmass

plagioclase may range to microphenocryst size (0.5 mm) and ranges in composition between  $An_{70}$  and  $An_{60}$ . Quench crystals of magnetite occur within the intersertal glass pools.

The olivine-plagioclase basalts from Le Conte Crater were studied in more detail because of their greater textural and chemical variability and because of their location immediately adjacent to vents which discharged rhyodacitic magma (Rock Mesa flow). The olivine and plagioclase phenocrysts are set in a fine, hyalopilitic to intergranular-intersertal groundmass of plagioclase laths ( $An_{65-70}$ ), black glass, and olivine. Fasciculate groundmass textures are rarely present. Olivine ranging in composition from  $Fo_{80}$  to  $Fo_{76}$  occurs as euhedral to subhedral phenocrysts and microphenocrysts up to 3 mm in length. The olivines are either discrete phenocrysts or are in clots of up to four crystals. Inclusions of cubic, red-brown, chromian spinel are common. Plagioclase inclusions are rare and appear to have crystallized from liquid which migrated along cracks in the grains. A few of the larger olivine phenocrysts are deeply resorbed with thin rims of granular pyroxene and glass. Plagioclase phenocrysts and microphenocrysts are up to 3 mm in length and fall into two major categories. The first type,  $Pl_I$ , has a subhedral, clear rim of approximately  $An_{65-70}$  composition, and

an inner zone charged with inclusions of vermiform glass, calcic plagioclase, and, less commonly, pyroxene. The inner zone may or may not have an irregular, clear core of more sodic plagioclase ( $An_{55-50}$ ) (Figure 27). The  $Pl_I$  phenocrysts are similar to those described by Heiken and Eichelberger (1980) in basalts from Chaos Crags, California. The second type,  $Pl_{II}$ , occurs as euhedral to subhedral microphenocrysts and lesser phenocrysts up to 1.5 mm in length. The  $Pl_{II}$  grains are clear and rarely show concentric compositional zonation from  $An_{70}$  to  $An_{65}$ . Minor marginal resorption is seen in a few examples. Strongly resorbed quartz xenocrysts were found in a Le Conte basalt adjacent to Devil's Lake (SS-192). The quartz xenocrysts are up to 1.5 mm in diameter and are rimmed with reaction coronas of granular clinopyroxene and brown glass (Figure 28).

Other proximal post-glacial basaltic rocks are present to the south and east of the area mapped for this study. These basalts and basaltic andesites have been described by Taylor (1978) and occur primarily in the vicinity north of Mt. Bachelor. The basalts contain phenocrysts of olivine and sparse microphenocrysts of plagioclase in a pilotaxitic groundmass of plagioclase microlites in subophitic intergrowth with clinopyroxene. The basaltic andesites contain up to 15% plagioclase phenocrysts and less than 2% each of

Figure 27. Post-glacial Le Conte basalt ( $\text{Ho}_{\text{bs}}$ ),  
Large plagioclase phenocryst has  
core of  $\text{An}_{50}$  and rim of  $\text{An}_{70}$ .  
Groundmass plagioclase is  $\text{An}_{70}$ .

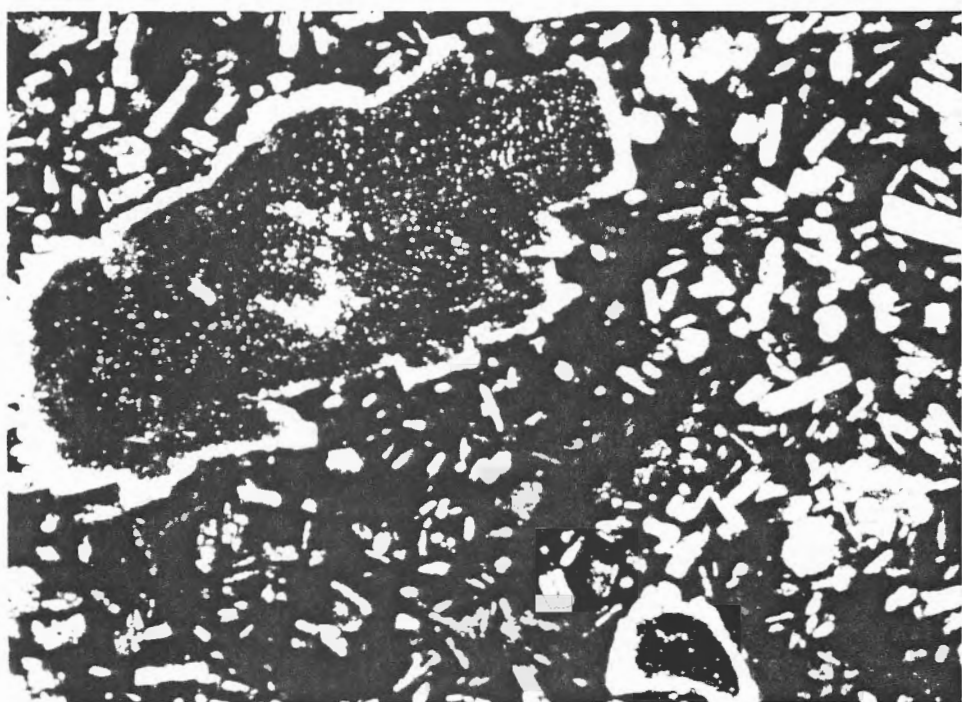
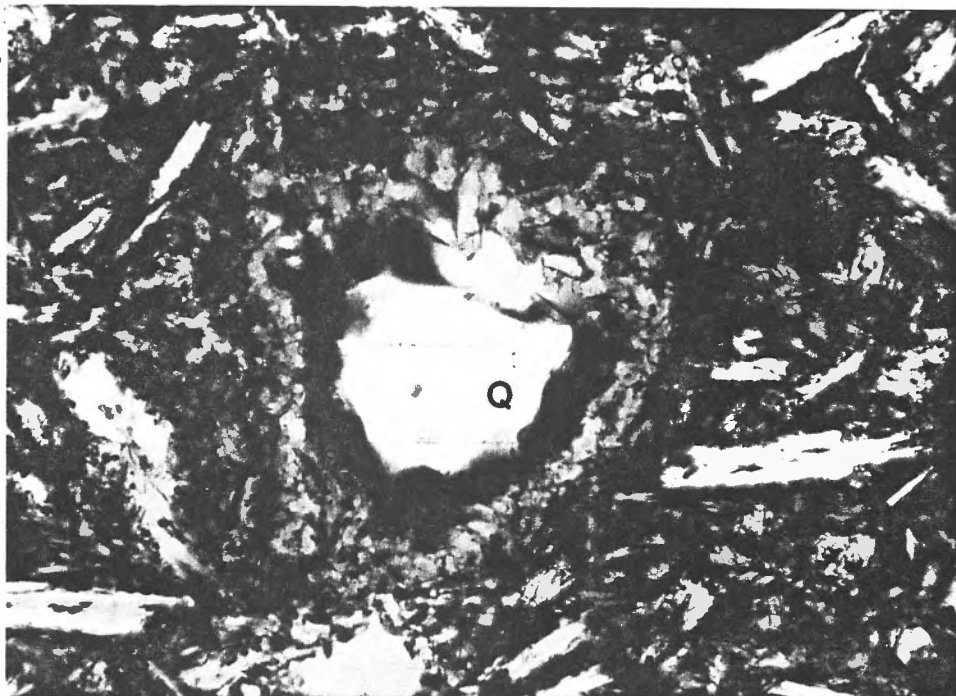


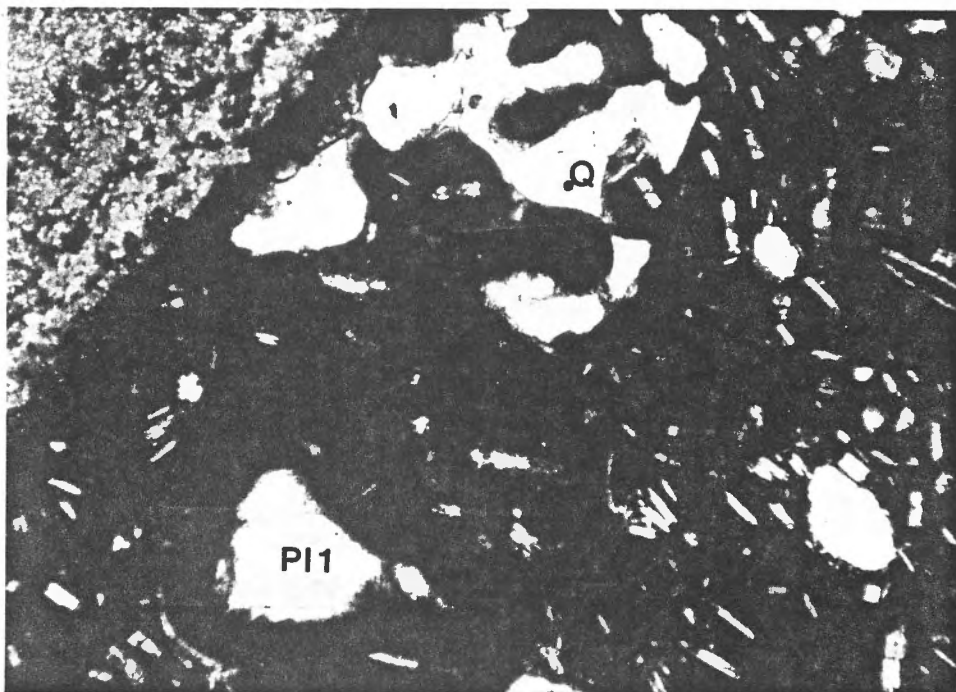
Figure 28. Post-glacial Le Conte basalts ( $Ho_{bs}$ ).

- a. Resorbed quartz xenocryst (Q) with mantle of brown glass and granular clinopyroxene.
- b. Resorbed quartz xenocryst (Q) with mantle of glass. Note resorbed plagioclase phenocryst ( $Pl_I$ ) with sodic core ( $An_{50-55}$ ) surrounded by zone of glass inclusions.

a.



b.



olivine and clinopyroxene phenocrysts set in a hyaloophitic to intergranular groundmass of plagioclase, clinopyroxene, and glass.

#### Post-glacial Rhyodacites (Hordana)

The post-glacial rhyodacites contain up to 20 volume percent phenocrysts and microphenocrysts of plagioclase and orthopyroxene, plus minor Fe-Ti oxides and rare amphibole and zircon microphenocrysts, set in a vitrophyric to pumiceous groundmass of dark brown glass and plagioclase micro-lites. As in the Holocene basalts of Le Conte Crater, the plagioclase phenocrysts in the post-glacial rhyodacites fall into two groups. Most of the microphenocrysts (0.5 mm in length) and some of the phenocrysts (0.5 mm to 3 mm in length) occur as euhedral to subhedral crystals with minor concentric-normal zonation and a narrow compositional range between  $An_{43}$  and  $An_{36}$ . The second group consists primarily of plagioclase phenocrysts which have moderate to strong resorption and abundant glass inclusions. The orientation of the glass inclusions within the plagioclase phenocrysts appears to be crystallographically controlled, and the inclusions are of either brown or clear glass. Phenocrysts of the second textural variety exhibit a broader range of anorthite contents than do the first group, from  $An_{52}$  to  $An_{34}$ . Normal and reverse concentric zonation and patchy

zonation are common. Resorption intensity ranges from minor rounding of the phenocrysts to strongly fritted phenocrysts (Figure 29). Both plagioclase phenocryst types contain common inclusions of euhedral, rod-like apatite, and rare inclusions of magnetite or orthopyroxene. Orthopyroxene occurs as euhedral microphenocrysts up to 1 mm in diameter. These microphenocrysts show a narrow compositional range ( $En_{63}$  to  $En_{59}$ ) and commonly have thin, reversely-zoned rims. The orthopyroxenes contain rare inclusions of apatite or magnetite, and a single orthopyroxene microphenocryst was observed to encompass a tiny, rounded inclusions of pleochroic amphibole. Minor magnetite and ilmenite microphenocrysts are euhedral to subhedral and less than 0.2 mm in length. Magnetite is also found as inclusions in orthopyroxene or, more rarely, in plagioclase. Hornblende is present as rare, corroded microphenocrysts to 0.3 mm in length, euhedral microphenocrysts less than 0.1 mm in length (quench crystallization?), or as inclusions in orthopyroxene (only one example observed). Euhedral zircon microphenocrysts are rare and up to 0.15 mm in length. Glomerocrysts are common and consist of the following mineral assemblages:

Plagioclase

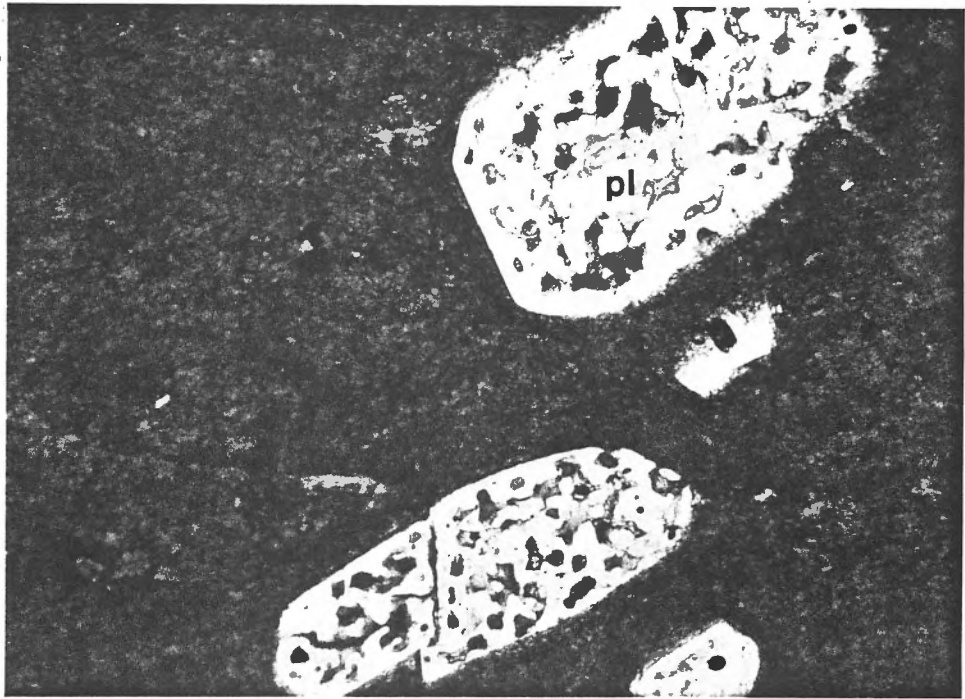
Plagioclase + Orthopyroxene + Magnetite

Orthopyroxene + Magnetite

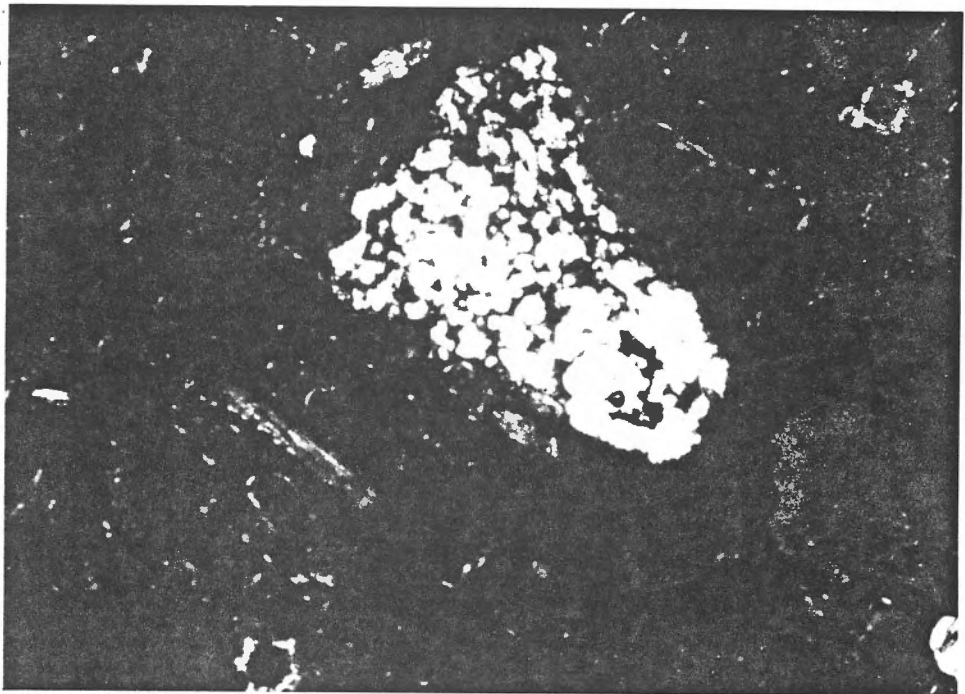
Figure 29. South Sister rhyodacites.

- a.  $Ho_{rda}$  - resorbed plagioclase phenocrysts with rounded margins and glass inclusions.
- b.  $Ho_{rda}$  - fritted plagioclase phenocryst ( $An_{52}$ ).
- c.  $Ps_{rda}$  - eu- to subhedral plagioclase phenocrysts.

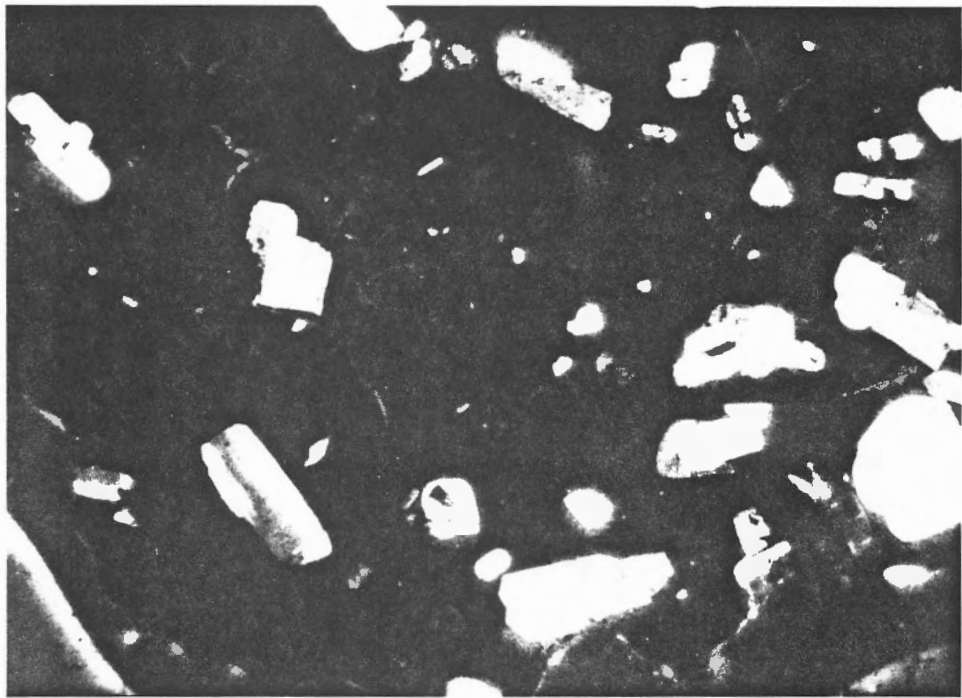
a.



b.



c.



### Orthopyroxene

The groundmass is predominantly dark brown to black glass with microlitic needles of plagioclase and, less commonly, fine, granular orthopyroxene. Magnetite dusting is common in the glass. Sheared and folded flow banding is another common feature.

Modal abundances of phenocrysts from the units described above are given in Appendix A. Microprobe analyses of phenocrysts are tabulated in Appendix C and plotted for illustration in Figure 30.

### Major and Trace Element Geochemistry

Major and trace element analyses of basalts and rhyodacites belonging to the early ( $Ps_{bs}$ - $Ps_{rda}$ ) and late ( $Ho_{bs}$ - $Ho_{rda}$ ) stage divergent suites at South Sister are included in Appendix B. The major element analyses were plotted versus silica in Figure 8, along with analyses from main cone andesites and dacites ( $Ps_{ad}$ ) and summit cone basaltic andesites ( $Ps_{ba}$ ) for comparison. As noted in Chapter 2 a compositional gap appears to separate rocks of 65%  $SiO_2$  and 72%  $SiO_2$ . In the divergent magmas, however, there are no analyses between 55.5%  $SiO_2$  and 72%  $SiO_2$ , a compositional gap of more than 16%! The trace element analyses for divergent lavas were plotted against a modified Larsen index (D.I.) in Figure 14. Main and summit

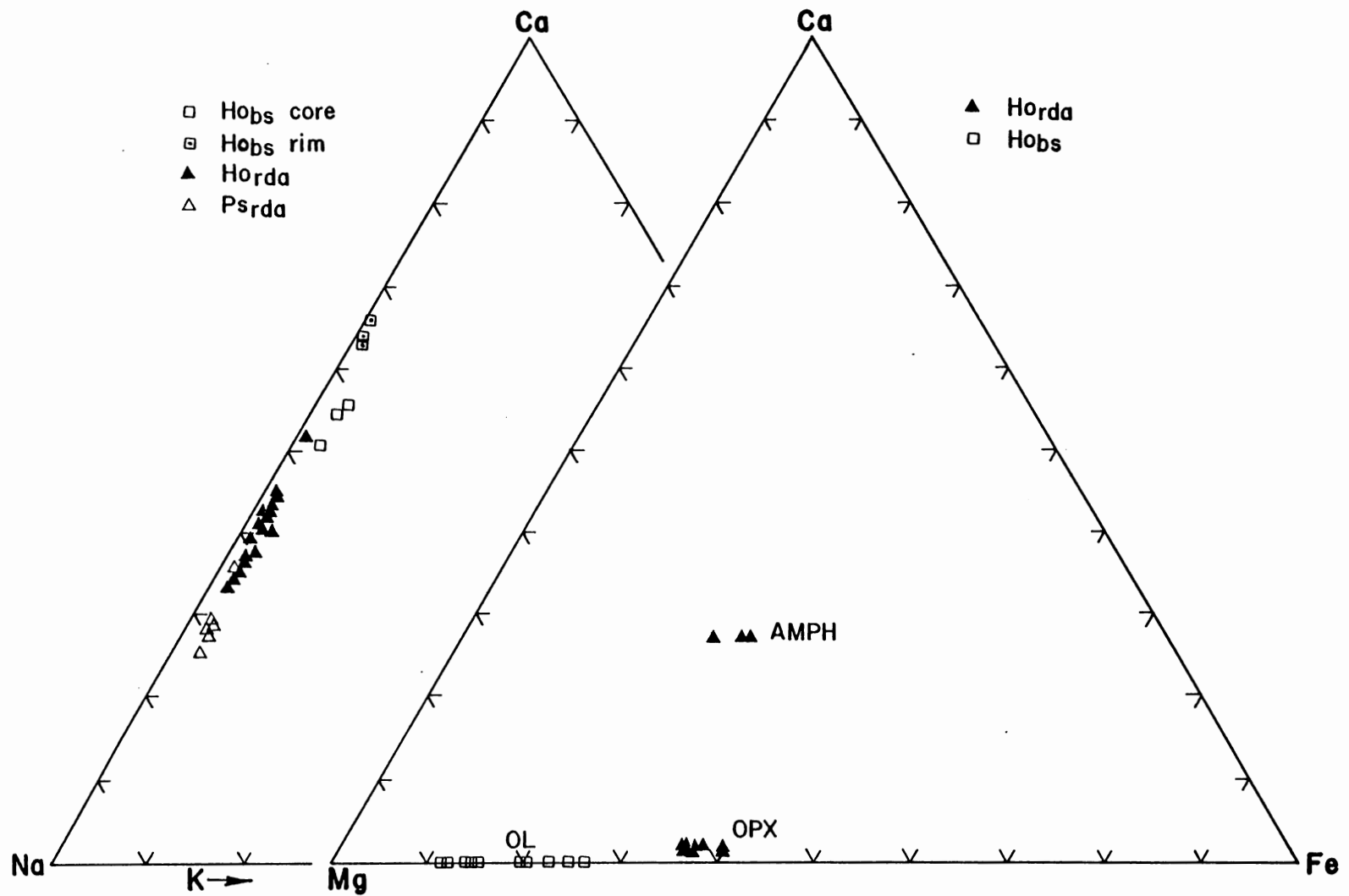


Figure 30. Phenocryst compositions in early rhyodacites ( $Ps_{rda}$ ) and post-glacial basalts and rhyodacites ( $Ho_{bs}$ ,  $Ho_{rda}$ ).

cone rocks were plotted for comparison. The compositional gaps illustrated by the major element data are apparent also in the trace element data.

The older basaltic rocks ( $Ps_{bs}$ ) are compositionally similar to their post-glacial counterparts, but they have slightly lower  $TiO_2$  and Ni, and higher Fe/Mg and Sr. The  $Ps_{bs}$  and  $Ho_{bs}$  basaltic rocks are strongly enriched in Ni and Cr relative to basalts from the main ( $Ps_{ad}$ ) and summit ( $Ps_{ba}$ ) cone units (Figure 15).

The rhyodacitic rocks ( $Ps_{rda}$ ,  $Ho_{rda}$ ) are compositionally similar with respect to major elements, although the post-glacial rhyodacites ( $Ho_{rda}$ ) have slightly higher  $K_2O/Na_2O$  ratios. Trace element abundances in these rocks range widely for all analyzed elements except Ni. The post-glacial rhyodacites ( $Ho_{rda}$ ) are distinctive from the early rhyodacites ( $Ps_{rda}$ ) in that they have generally higher abundances of Rb and Sr, and lower abundances of Zr than do the early rhyodacites. Zr abundances in the early rhyodacites drop off sharply from levels extant in the main cone rocks and range between 259 ppm and 183 ppm. Zr abundances in the post-glacial rhyodacites have a much narrower range of between 180 ppm and 196 ppm.

#### Petrogenesis

The wide compositional gap between the calc-alkaline

basalts and rhyodacites at South Sister appears to preclude a consanguinous igneous association, yet they are closely related in a spatial and temporal sense. The presence of quartz xenocrysts in the Le Conte basalt, abundant disequilibrium phenocryst textures in both the post-glacial basalts and rhyodacites, and the position of the Le Conte basaltic vent immediately adjacent to the Rock Mesa rhyodacitic flow all suggest a degree of interaction between the basalt and a silicic, probably crustal, component. The discussions that follow consider briefly the petrogenesis of the basalts, while that of the rhyodacites is considered in more detail.

### Basalts

The compositions, crystallization sequences, and phenocryst compositions of the post-glacial basalts can be used to constrain the physical conditions under which the basaltic magma crystallized.

#### Crystallization Sequence

Post-glacial basaltic rocks from the South Sister area range in composition from basalt to basaltic andesite. The olivine basalts from Cayuse Crater have the most primitive compositions and contain phenocrysts of olivine with inclusions of chromian spinel. The more evolved basalts from Le

Conte Crater crystallized plagioclase in addition to olivine and spinel. Finally, the most evolved of the post-glacial basaltic andesites, those immediately north of Mt. Bachelor, precipitated olivine (+ spinel), plagioclase, and clinopyroxene (Taylor, 1978). The deduced crystallization sequence in post-glacial basaltic rocks from the South Sister area is therefore: olivine + spinel, olivine + spinel + plagioclase, and olivine + spinel + plagioclase + clinopyroxene. Considering the similarity between the post-glacial and shield basalts with respect to bulk rock and phenocryst compositions, this crystallization sequence is likely to apply to the shield basalts ( $Ps_{bs}$ ) as well.

#### Crystallization Pressure

Phase relations in basaltic systems and the paragenetic sequence in post-glacial basaltic rocks from South Sister provide a rough constraint on estimates of the pressure of crystallization. The lack of clinopyroxene as a near-liquidus phase limits crystallization of the basaltic rocks to pressures less than about 7 Kb (Kushiro and Thompson, 1972). High-alumina basalt compositions that crystallize olivine and plagioclase before clinopyroxene have probably crystallized at pressures less than about 4.5 Kb (Green et al, 1967). The olivine-plagioclase assemblage in the Cayuse and Le Conte basalts suggests

that these basalts crystallized at relatively low pressure, between one atmosphere and 4.5 Kb.

### Water Content

The lack of hydrous phases precludes direct determination of  $f_{\text{H}_2\text{O}}$  and water content in the basaltic rocks. Crystallization experiments on basaltic compositions similar to those of the South Sister divergent suites indicate that plagioclase is the liquidus phase under anhydrous conditions (Yoder and Tilley, 1962; Yoder, 1969). With low to moderate  $P_{\text{H}_2\text{O}}$  the crystallization of plagioclase is suppressed and olivine becomes the primary liquidus phase. Low abundances of  $\text{H}_2\text{O}^+$  (0.3 to 0.8%) in the Cayuse and Le Conte basalts, in conjunction with the observed paragenetic sequence and low pressure phase relationships, suggest that the basalts contained only minor amounts of water ( $\leq 1\%$ ).

### Temperature and $f_{\text{O}_2}$

It is not possible to use the Fe-Ti oxide geothermometer-oxygen barometer to estimate eruption temperatures and oxygen fugacities of the basalts, because magnetite and ilmenite phenocrysts do not co-exist in the shield ( $\text{Ps}_{\text{bs}}$ ) or post-glacial ( $\text{Ho}_{\text{bs}}$ ) basaltic rocks. The olivine saturation surface presented by Roeder and Emslie (1970) for

basaltic liquids can be used to estimate crystallization temperatures for the basaltic rocks. The relationship between olivine composition and crystallization temperature, and the mole percent of FeO and MgO in the liquid was determined empirically from experimental data on olivine-liquid equilibria (Roeder and Emslie, 1970). Olivine compositions in the post-glacial basalts indicate crystallization temperatures of from 1220°C for the Cayuse olivine basalt to 1150°C for the Le Conte olivine-plagioclase basalt, according to Figure 7 of Roeder and Emslie (1970). These temperatures are in accord with the 1200°C temperature determined by the olivine-spinel geothermometer (Evans and Frost, 1975) for similar post-glacial basaltic rocks from Collier Cone, northwest of North Sister.

Oxygen fugacities for basaltic liquids can be estimated from the relationship between  $f_{O_2}$  and the ratio of ferric to ferrous iron, determined by Roeder and Emslie (1970):

$$f_{O_2} = 10^{-5.2} \frac{X_{FeO_{1.5}}^5}{X_{FeO}}$$

where  $X_{FeO_{1.5}}$  and  $X_{FeO}$  refer to the mole fractions of  $FeO_{1.5}$  and FeO in the liquid. Bulk rock compositions of Cayuse and Le Conte basalts define a narrow range of  $f_{O_2}$  values between  $10^{-9.5}$  and  $10^{-9.6}$  atm. These values are considered to be maximum owing to expected post-eruption

oxidation.

### Rhyodacites

Discussion of the petrogenesis of the rhyodacites is divided into three sections. The first section deals with the physical magmatic conditions under which the rhyodacitic chamber may have existed. The second and third sections consider two possible modes of origin for the rhyodacites: fractional crystallization and partial melting.

#### Intensive Variables

Knowledge of the physical conditions within the post-glacial rhyodacitic magma chamber is essential to any complete petrogenetic model for the origin of these rocks.  $T$ ,  $f_{O_2}$ ,  $P_{H_2O}$ ,  $P_T$ , density and viscosity were estimated for the post-glacial rhyodacites using phenocryst and bulk rock compositions and thermodynamic relationships.

The temperature and oxygen fugacity of the rhyodacitic magma at the time of eruption were estimated from the compositions of coexisting magnetite and ilmenite microphenocrysts and the data of Buddington and Lindsley (1964). Temperatures range between 850°C and 875°C and oxygen fugacities plot near the N-NO buffer curve (Figure 31). These values are similar to those obtained from the Crater Lake rhyodacites by Ritchey (1980).

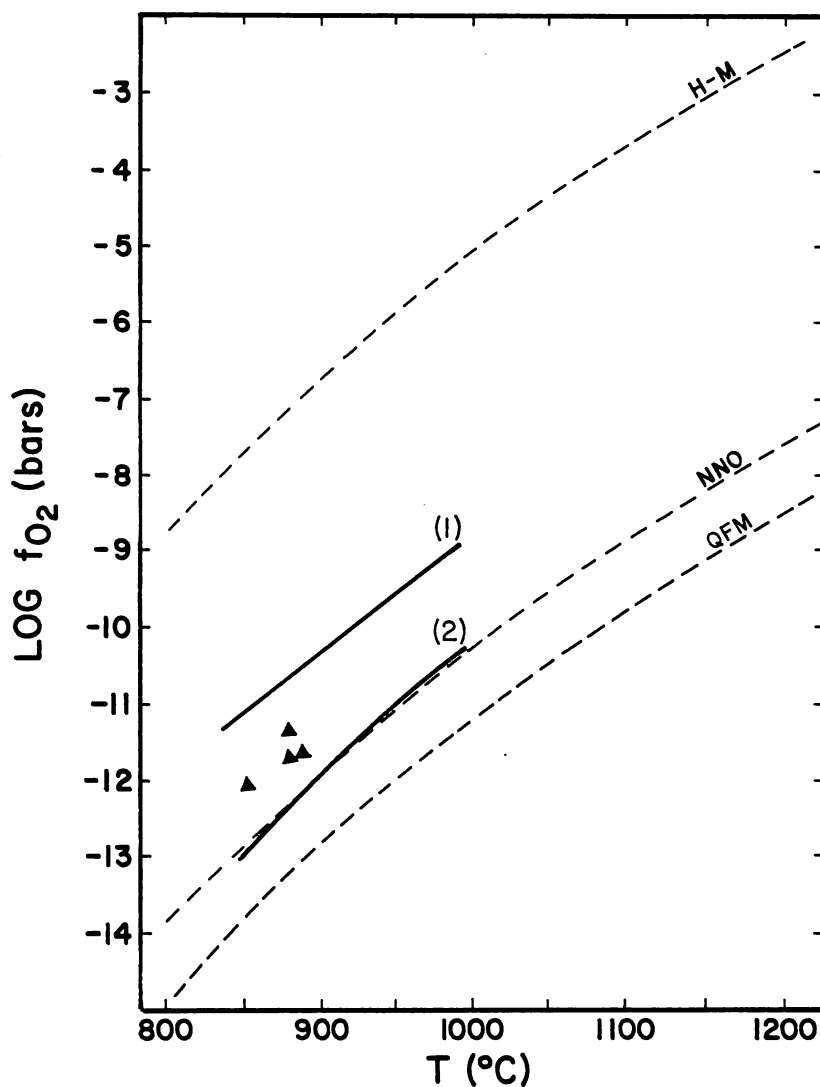
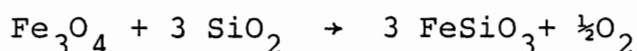


Figure 31. T- $f_{O_2}$  relations of post-glacial rhyodacites estimated from the magnetite-ilmenite geothermometer of Buddington and Lindsley (1964). Dashed curves are synthetic buffers; numbered curves after Carmichael (1967). (1): Hb and Bi-bearing dacites; (2): OPX-bearing rocks.

If equilibration temperatures are known, the plagioclase geothermometer of Kudo and Weill (1970) provides an estimate of the water pressure in the magma. Coexisting glass and plagioclase microphenocrysts along with the temperatures calculated from the Fe-Ti oxide geothermometer were used to estimate water pressure in the post-glacial rhyodacitic magma chamber. Calculated values of  $P_{\text{H}_2\text{O}}$  fall between 1.5 and 1.7 Kb.

Total pressure is the most difficult parameter to estimate because most reactions have small volume changes. I have attempted to estimate total pressure (P) by two methods. If the temperature (T) and the equilibrium water pressure ( $P_{\text{ew}}$ ) in a magma are known, the total pressure and water content can be estimated from the work of Burnham and Davis (1974) on the solubility of water in an albite melt. Burnham and Davis (1974) determined the P-T relationships of calculated crystal-liquid equilibrium as a function of the activity of  $\text{H}_2\text{O}$  and the equilibrium water pressure. Application of the Fe-Ti oxide temperature ( $875^\circ\text{C}$ ) and  $P_{\text{H}_2\text{O}}$  (1.6 Kb) calculated for a post-glacial rhyodacite from South Sister to Figure 19 of Burnham and Davis (1974) yields a total pressure of 2.1 Kb and a water content of 5.3 weight percent. The water content appears to be too high, considering the absence of primary liquidus amphibole, the high apparent viscosity of the

domes, and the docile mode of eruption. The steep isopleths for the activity of water in the liquid make the estimate particularly sensitive to the temperature determination. If the temperature calculated from the Fe-Ti thermometer was 50°C higher, the estimate of the water content in the rhyodacitic magma would be less than 4 weight percent, in accord with the experimental data of Ritchey (1979). A crude estimate of the total pressure can also be obtained from the following reaction:



The equilibrium constant for this reaction is:

$$\log K = \frac{-14327}{T(^{\circ}\text{K})} + 5.46 + \frac{0.1451}{T(^{\circ}\text{K})} (P_{\text{bars}} - 1) ,$$

where  $\log K = 3 \log a_{\text{Fe}_3\text{O}_4} + \frac{1}{2} \log f_{\text{O}_2} - 3 \log a_{\text{SiO}_2} - \log a_{\text{mt}}$  (Williams, 1971). The post-glacial rhyodacites contain all requisite phases for this calculation except quartz. However, the rhyodacites have in excess of 25% normative quartz; in rocks this rich in silica, Mertzman and Williams (1981) suggest that an assumption of  $a_{\text{SiO}_2} = 1$  may be approximately correct. Making this assumption, the calculated total pressure for the post-glacial rhyodacites is 4.1 Kb. According to Williams (1971) the thermodynamic uncertainties indicate that this estimate is accurate to within  $\pm 0.5$  Kb, but the calculation is also sensitive to estimates of temperature, oxygen fugacity, and the activity corrections, particularly the activity of  $\text{SiO}_2$ . The

actual uncertainty is almost certainly larger. If one assumes an error of + 0.1 log units in  $a_{\text{SiO}_2}$  and ideal behavior of the solid solutions, the pressure estimate drops to 1.8 Kb. The data are tenuous, but suggest that the post-glacial rhyodacitic liquids may have segregated at pressures between about 2 and 4 kilobars prior to eruption.

The density of the rhyodacitic liquid was calculated from partial molar volumes using the method of Bottinga and Weill (1970). At  $T = 875^\circ\text{C}$ ,  $P_T = 3 \text{ Kb}$ , and a water content of 3%, the estimated liquid density is  $2.26\text{g/cm}^3$ . Similarly, the viscosity of the rhyodacitic liquid was calculated using the same physical parameters according to the method of Shaw (1972), and a value of  $\log \eta$  of 6.14 (poise) was obtained. This viscosity represents that of the liquid phase only. Crystals suspended in the rhyodacitic liquid would increase the apparent viscosity, and the extent of the increase can be estimated from the relationship of Einstein (1906):

$$\eta_s = (1 + 2.5\phi)\eta_o \quad , \text{ where}$$

$\eta_s$  is the viscosity of melt plus crystals,  $\phi$  is the volume fraction of crystals present, and  $\eta_o$  is the viscosity of the liquid phase. Applying the liquid viscosity and a  $\phi$  value determined from modal phenocryst abundances in the post-glacial rhyodacites (Appendix A) to this equation

yields a  $\log \eta_s$  value of 6.27 (poise).

Intensive parameters for the post-glacial rhyodacites are summarized in Table 5.

#### Fractional Crystallization

It is unlikely that the post-glacial rhyodacites at South Sister were produced by fractional crystallization from a parental basaltic magma; the wide compositional gap (16-18%  $\text{SiO}_2$ ) between the two magma types is difficult to reconcile with such an origin. Ritchey (1979, 1980) has presented a strong case for the origin of the divergent suite at Crater Lake, Oregon, by efficient fractional crystallization from a parental basaltic magma. However, glass analyses of the Crater Lake rocks have a more gradual compositional change than do bulk rock analyses, and the apparent strong bimodality is mainly due to the bulk compositions of cumulate assemblages.

Both the Yamsay Mountain and Medicine Lake caldera complexes have bimodal suites in which rocks of intermediate composition are volumetrically insignificant (Hering, 1981; Mertzman and Williams, 1981). Hering (1981) and Mertzman and Williams (1981) have shown that the rhyodacitic and rhyolitic rocks of the Yamsay Mountain and Medicine Lake complexes, respectively, owe their origin to fractional crystallization from andesitic or dacitic

TABLE 5.

PHYSICAL PARAMETERS CALCULATED FOR POST-GLACIAL RHYODACITIC LAVAS ( $H_{o_{rda}}$ )

a. Temperature	850°C to 875°C	(Buddington and Lindsley, 1964)
b. $\text{Log } f_{O_2}$	-11.5 to -12.3	(Buddington and Lindsley, 1964)
c. $P_{H_2O}$	1.5 to 1.7 Kb	(Kudo and Weill, 1970)
d. Total pressure	2.1 Kb	(Burnham and Davis, 1974)
	4.1 Kb	(Williams, 1971)
e. Density @ $T = 875^\circ\text{C}$ $P_T = 3 \text{ Kb}$ $H_2O = 3\%$	$\rho = 2.262$	(Bottinga and Weill, 1970)
f. Log Viscosity @ $T = 875^\circ\text{C}$ $P_T = 3 \text{ Kb}$ $H_2O = 3\%$	6.14	(Shaw, 1972)

parental magmas. To test this hypothesis for silicic rocks from South Sister, least-squares fractionation models were calculated for both the early and post-glacial rhyodacites with main and summit cone dacitic compositions as parental liquids. The most successful models are listed in Table 6, along with observed and predicted trace element abundances.  $\Sigma r^2$  for all models ranges between 0.23 and 0.48. Ritchey (1980) has shown the importance of amphibole fractionation in the generation of the Crater Lake rhyodacites. Amphibole does not occur in the South Sister main and summit cone dacites, and occurs only rarely as microphenocrysts in the rhyodacites. Though petrographic evidence indicates that amphibole did not become a liquidus phase until very late in the crystallization sequence, fractionation models were calculated both with, and without, amphibole in the phenocryst assemblage. The presence of amphibole in the fractionating assemblage does not significantly change the quality of fit or the predicted trace element abundances.

The fractionation models based on major elements are acceptable, although the fits are worse than those obtained from the main and summit cone sequences (Tables 2 and 3). All the models must be rejected, however, because they conflict with observed trace element abundances. As was the case for the main and summit cone sequences, observed Rb

TABLE 6.

## MAJOR AND TRACE ELEMENT FRACTIONATION MODELS - SILICIC ROCKS

	MODEL #1		MODEL #2	
	<u>Parent</u>	<u>Daughter</u>	<u>Parent</u>	<u>Daughter</u>
	SS-200	SS-123	SS-200	SS-123
SiO <sub>2</sub>	65.27	72.99	65.27	72.99
TiO <sub>2</sub>	0.85	0.35	0.85	0.35
Al <sub>2</sub> O <sub>3</sub>	16.07	14.64	16.07	14.64
FeO	4.95	2.13	4.95	2.13
MnO	0.09	0.06	0.09	0.06
MgO	1.54	0.43	1.54	0.43
CaO	3.07	1.75	3.87	1.75
Na <sub>2</sub> O	4.95	4.55	4.95	4.55
K <sub>2</sub> O	2.23	3.01	2.23	3.01
P <sub>2</sub> O <sub>5</sub>	0.18	0.08	0.18	0.08
$\Sigma r^2$	0.477		$\Sigma r^2$	0.265
Plagioclase (An <sub>52</sub> )		21.0	Plagioclase (An <sub>49</sub> )	18.2
Orthopyroxene (En <sub>63</sub> )		5.1	Hornblende	8.3
Oxides		3.1	Orthopyroxene (En <sub>59</sub> )	1.1
Apatite		0.5	Oxides	2.2
F		0.698	Apatite	0.1
			F	0.698

## Trace Elements

	<u>Predicted</u>	<u>Observed</u>	<u>Predicted</u>	<u>Observed</u>
Cr	0.01- 12.0	10	0- 10	10
Ni	5.0 - 14.0	5	2- 9	5
Zr	296 - 323	194	284-319	194
Rb	64.0 - 67.9	70.5	65- 68	70.5
Sr	187 - 365	230	147-262	230
Ba	733 - 824	809	722-811	809

TABLE 6. (Continued)

	MODEL #3		MODEL #4	
	<u>Parent</u>	<u>Daughter</u>	<u>Parent</u>	<u>Daughter</u>
	SS-153	SS-91	SS-153	SS-91
SiO <sub>2</sub>	63.72	72.85	63.72	72.85
TiO <sub>2</sub>	1.16	0.37	1.16	0.37
Al <sub>2</sub> O <sub>3</sub>	16.14	14.45	16.14	14.45
FeO	5.64	2.12	5.64	2.12
MnO	0.11	0.06	0.11	0.06
MgO	2.16	0.47	2.16	0.47
CaO	4.10	1.78	4.10	1.78
Na <sub>2</sub> O	4.72	4.79	4.72	4.79
K <sub>2</sub> O	1.98	3.08	1.98	3.08
P <sub>2</sub> O <sub>5</sub>	.27	0.03	0.27	0.03
$\Sigma r^2$	0.225		0.225	
Plagioclase (An <sub>56</sub> )	23.3	Plagioclase (An <sub>56</sub> )	23.2	
Orthopyroxene (En <sub>68</sub> )	7.0	Hornblende	0.6	
Oxides	4.1	Orthopyroxene (En <sub>68</sub> )	6.8	
Apatite	0.4	Oxides	4.0	
F	0.649	Apatite	0.3	
		F	0.648	

## Trace Elements

	<u>Predicted</u>	<u>Observed</u>	<u>Predicted</u>	<u>Observed</u>
Cr	0- 4	7	0- 4	7
Ni	4- 15	4	3- 15	4
Zr	269-302	250	277-312	250
Rb	56- 60	64	57- 61	64
Sr	198-420	195	190-424	195
Ba	753-865	673	766-888	673

concentrations are too high in the differentiated rocks, and observed Zr abundances are too low, relative to their predicted concentrations.

Zr has been a problematical element in many calc-alkaline volcanic suites. It behaves uniformly in some suites and erratically in others (Robyn, 1977; Hering, 1981; White, 1980 a and b). At South Sister Zr abundances drop sharply in the rhyodacitic rocks relative to the rest of the suite (Figure 14). Robyn (1977) and Hering (1981) have suggested the possibility of zircon fractionation to explain the sometimes erratic behavior of Zr in calc-alkaline rocks. Indeed, zircon microphenocrysts are present in the South Sister rhyodacites. It is unlikely, however, that zircon fractionation was responsible for the Zr abundance patterns in the South Sister rhyodacites. Calculated Stokes settling velocities using the temperature, viscosity, and density data summarized in Table 5 indicate that more than 600,000 years (or nearly the maximum age of South Sister volcano) would be required to settle a zircon crystal 0.1 mm in length through a rhyodacitic magma chamber with a vertical dimension of 1 km. The high yield strength expected in the viscous, rhyodacitic liquid would also be an effective barrier to zircon fractionation. Magnetite and ilmenite have high  $D_{Zr}$  values (0.5-2.0), but insufficient amounts of these phases

could have fractionated to produce the Zr depletion in the rhyodacites, according to the models in Table 6. If a dense zircon crystal ( $\rho = 4.68$ ) cannot sink through its magma chamber in a geologically reasonable period of time, it is improbable that the major phenocryst phases of the same size would do so either. However, separation of liquid from crystals during flowage in a conduit (Komar, 1972) cannot be discounted without further data.

#### Partial Melting

H/M vs. H diagrams (refer to Chapter 3) for the early and post-glacial rhyodacites and post-glacial basalts are illustrated in Figure 32. Trends of the main ( $Ps_{ad}$ ) and summit ( $Ps_{ba}$ ) cone lavas are shown for comparison. Geochemical trends for the rhyodacitic rocks have the steep slopes diagnostic of an origin by batch partial melting on the Rb/Zr, Rb/Ba, and Rb/K versus Rb diagrams. Slopes and Y-intercepts of the rhyodacites on the Rb/K and Rb/Ba versus Rb diagrams differ markedly from those of the main and summit cone sequences and suggest that South Sister rhyodacites are not consanguinous with main and summit cone differentiated rocks and probably have a different source. Despite their difference in age, the early and post-glacial rhyodacites describe a common linear trend, with the post-glacial rhyodacites having higher values of

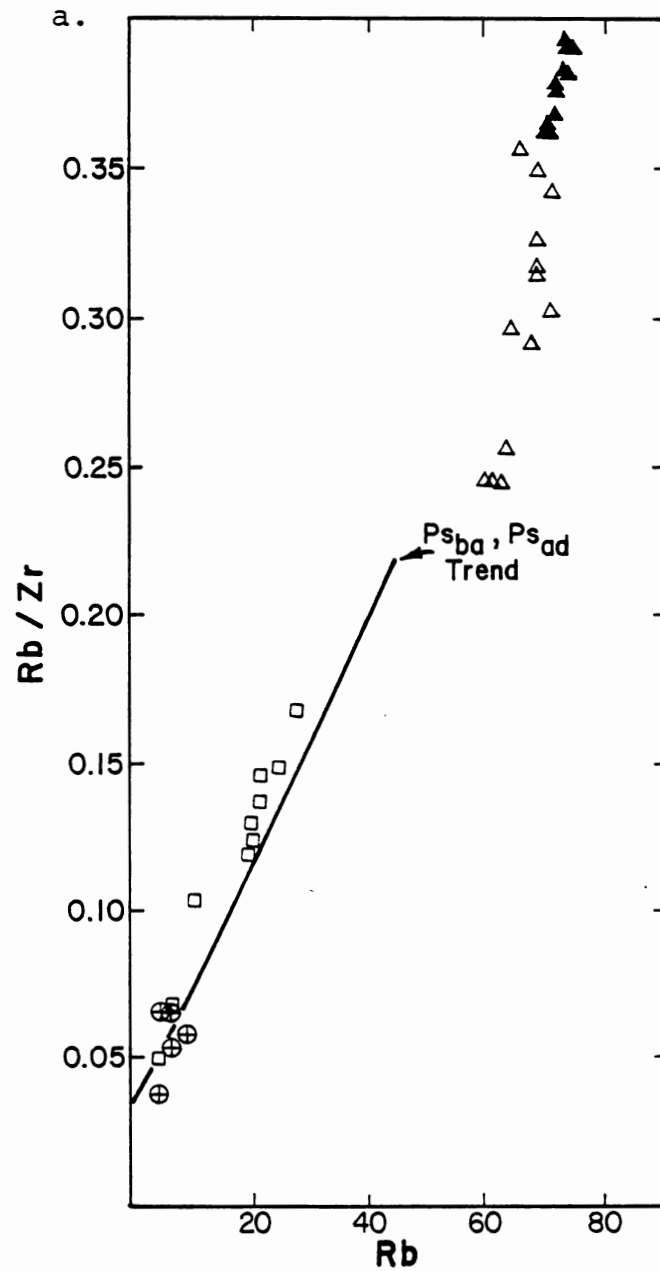


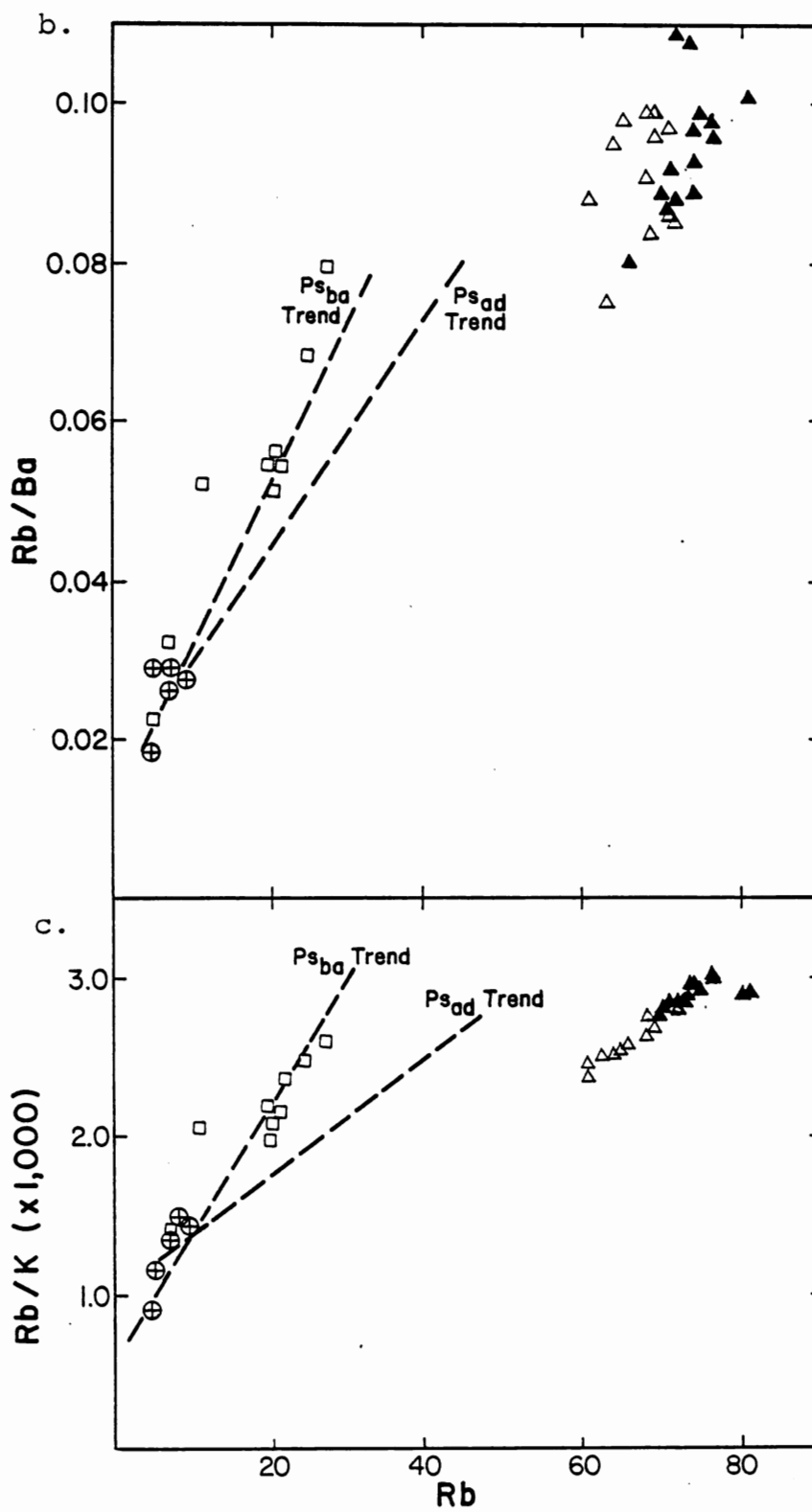
Figure 32. H/M versus H diagrams for divergent suites from South Sister and Crater Lake.

a. Rb/Zr vs. Rb - South Sister

Figure 32. (Continued)

b. Rb/Ba vs. Rb - South Sister

c. Rb/K vs. Rb - South Sister



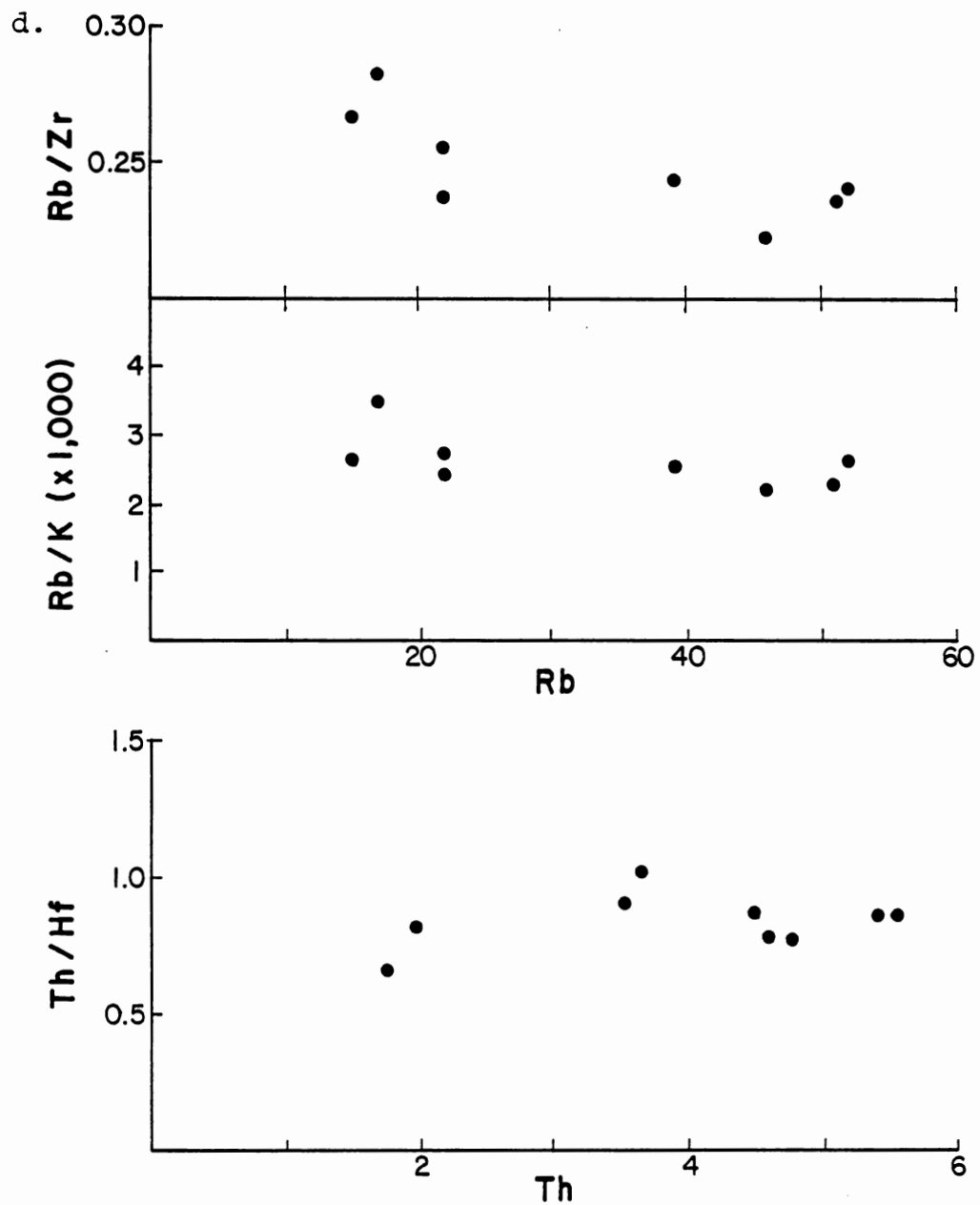


Figure 32. (Continued)

d. Rb/Zr vs. Rb, Rb/K vs. Rb, and Th/Hf vs. Th for the Pinnacles section at Crater Lake. Data are from Ritchey (1979).

Rb/Zr, Rb/Ba, and Rb/K as Rb concentrations increase. Just as in the case of the main and summit cone lavas, fractional crystallization processes will not produce the rapid increase in excluded element ratios unless unreasonably high  $\bar{D}$ 's are assumed for the moderately excluded M elements. The  $\bar{D}_{Zr}$  must again be equal to 0.5 to reproduce the rate of increase of Rb/Zr ratios with increasing Rb abundances in the rhyodacites, and no reasonable fractionating assemblage will result in a  $\bar{D}_{Zr}$  of 0.5. The data point to the possible presence of amphibole as a residual phase in the source rocks, a conclusion similar to that reached for the main and summit cone lavas. If the source rocks are of intermediate to silicic composition, zircon may also be present as a residual phase (Watson, 1979). The post-glacial basaltic rocks also have trends diagnostic of partial melting, and roughly parallel to the trends of the main and summit cone sequences. The inferred origin by partial melting of the South Sister divergent suites stands in contrast to the fractional crystallization mechanism proposed by Ritchey (1980) to explain the divergent magmas at Crater Lake, Oregon. Data from Ritchey (1979) are plotted on H/M versus H diagrams in Figure 32d. The patterns in Figure 32 a through d support Ritchey's (1979, 1980) contention that the variation in the Crater Lake divergent suite is caused primar-

ily by fractional crystallization, while that at South Sister owes its existence to partial melting of different source rocks, a mantle source for the basaltic magmas and, because of their silicic compositions, a probable crustal source for the rhyodacitic magmas.

The field, petrographic and geochemical data presented thus far suggest that the divergent suites at South Sister volcano may have evolved through interaction of mantle-derived basaltic magmas with crustal rocks. This topic is explored in the next section.

#### Basalt-Crust Interaction

Crustal interaction with ascending basaltic magmas is implied when partial melting of crustal material is invoked as the generative mechanism for the silicic end-member of bimodal volcanic suites (Lachenbruch and Sass, 1979; Sigurdsson, 1977; Bacon and Duffield, 1980; Hildreth, 1981). Convecting and crystallizing basaltic magmas provide the heat necessary for the melting of crustal rocks (Holmes, 1931; Wilcox, 1954; Ewart and Stipp, 1968; Hildreth, 1979, 1981; Myers and Marsh, 1981). Perhaps for this reason, extensional tectonic regimes, which favor the rapid ascent and eruption of large volumes of basaltic magma, are the most common location of bimodal volcanic suites (Martin and Piwinski, 1972; Hering, 1981).

Even at Crater Lake, Oregon, where Ritchey (1979, 1980) has made a strong case for the origin of the silicic rocks by fractional crystallization,  $^{18}\text{O}/^{16}\text{O}$  ratios and anomalous enrichments of included trace elements in the rhyodacites suggest some degree of shallow crustal interaction. It may also be significant that divergent and bimodal associations occur only in areas having a long history of earlier volcanism. Petrographic and geochemical evidence from South Sister indicate that the divergent suites developed in response to interaction between basaltic magmas and silicic crustal rocks.

#### Petrographic Evidence

Textural disequilibrium features support an origin for the post-glacial rhyodacites by partial melting of crustal rocks and interaction of the rhyodacitic magmas with their associated basalts. Post-glacial rhyodacites contain up to 15 volume percent plagioclase phenocrysts. In contrast to those from the early rhyodacites, plagioclase phenocrysts from the  $\text{Ho}_{\text{rda}}$  flows have strong compositional and textural diversity. Microphenocrysts and some phenocrysts are euhedral and weakly zoned, similar to those of the early rhyodacites. Up to 70% of the plagioclase phenocrysts in the  $\text{Ho}_{\text{rda}}$  flows, however, are subhedral to anhedral, in various stages of resorption, and

charged with glass inclusions. The phenocrysts as a group have a wide compositional range, from An<sub>52</sub> to An<sub>34</sub>. There is no clear compositional bimodality of the plagioclase phenocrysts based on texture, but resorbed crystals show a tendency toward more An-rich compositions. The resorption textures range from strongly fritted to only slightly resorbed. The range in resorption textures was shown in Figure 29, along with euhedral plagioclase phenocrysts from both rhyodacitic units for comparison. The observed range in plagioclase resorption textures and compositions is that which might be expected during the progressive disaggregation of a source rock undergoing partial melting or assimilation. Plagioclase xenocrysts inherited from the source rock would continually re-equilibrate until they reached the composition of the liquidus plagioclase in equilibrium with the enclosing liquid (McBirney, 1979). Plagioclase resorption textures similar to those in the Ho<sub>rda</sub> flows have been interpreted by Sigurdsson (1968, 1977) as assimilation textures in Icelandic rhyolites thought to represent partial melts of an oceanic plagiogranite source rock. The presence in the post-glacial rhyodacites of abundant plagioclase phenocrysts of intermediate to sodic composition and bearing resorption-assimilation textures lends strong support to the argument that the post-glacial rhyodacites developed as

partial melts from crustal rocks.

The location of the basaltic vent at Le Conte Crater adjacent to the post-glacial rhyodacitic vent at Rock Mesa (Figure 26), and the relative proximity in age of the two units suggest a close relationship between the two magmas. Petrographic features of the Le Conte basalt that support this contention are listed here and discussed below:

1. The presence in the basalts of resorbed quartz xenocrysts.
2. The presence in the basalts of abundant plagioclase phenocrysts with disequilibrium features that suggest they did not crystallize initially in the magma in which they now reside.
3. The distribution of the resorbed plagioclase phenocrysts in the Le Conte basalt flow.

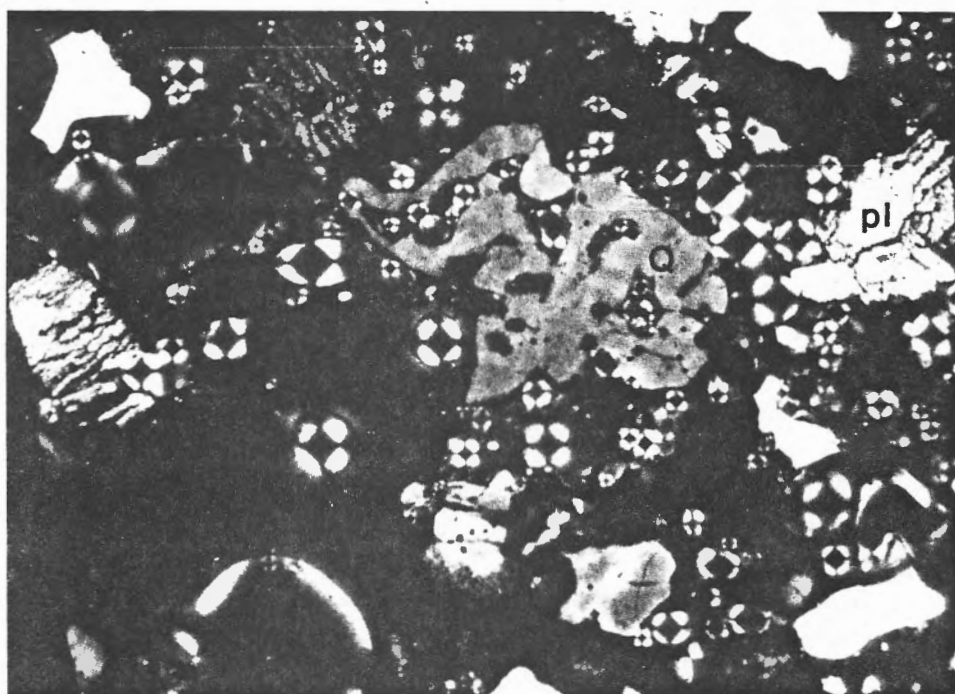
Quartz xenocrysts were found in the Le Conte basalt near Devil's Lake. The xenocrysts are strongly resorbed and have reaction coronas of clinopyroxene and glass (Figure 28). No quartz-bearing rocks are exposed at the surface in the Three Sisters area, but the early rhyodacites ( $Ps_{rda}$ ) contain nearly 30% normative quartz, and thus their hypabyssal equivalents might well be expected to have crystallized to a quartz-bearing assemblage. Outcrops of  $Ho_{rda}$  are spatially restricted to areas underlain by  $Ps_{rda}$  (Figure 26). Moreover, partially fused,

quartz-bearing plutonic rocks, probably of Tertiary age, are found in the compositionally-zoned Collier flow, immediately northwest of North Sister (Figure 33).

Unresorbed plagioclase phenocrysts and microphenocrysts from the Le Conte basalt are weakly zoned, with compositions ranging between  $An_{65}$  and  $An_{70}$ . The disequilibrium plagioclase phenocrysts have a strongly resorbed, sodic core ( $An_{50-55}$ ), an intermediate zone charged with glass inclusions, pyroxene and calcic plagioclase, and a clear, subhedral rim of more calcic composition ( $An_{65-70}$ ). Sodic cores are absent from some crystals, in which case the entire area enclosed by the calcic rim is composed of glass inclusions, pyroxene and calcic plagioclase. Representative plagioclase phenocryst textures from the Le Conte basalts were illustrated in Figures 5, 27 and 28. The compositional overlap between sodic cores of resorbed plagioclase phenocrysts in the Le Conte basalts and the most calcic of the resorbed plagioclase phenocrysts in the  $Ho_{rda}$  flows suggests at least limited interaction between the basaltic and rhyodacitic liquids and silicic crustal rocks.

The resorbed plagioclase phenocrysts in the Le Conte basalt are not distributed randomly through the flow. Plagioclase phenocryst modes for five samples of Le Conte basalt are plotted versus their distance from the vent in

Figure 33. Fused granitic xenolith from the  
Collier basalt flow - crossed nicols.



in Figure 34. If basalts at the most distal part of the flow are assumed to have been erupted first and from the uppermost part of the basaltic chamber, and basalts closest to the vent represent liquids originating from deeper levels in the chamber, then the modal abundances of resorbed and total plagioclase appear to change smoothly with depth of origin in the chamber. Using this reasoning, resorbed plagioclase is more abundant and contributes a larger proportion of total plagioclase at the assumed top of the basaltic chamber. Thus the ratio of resorbed plagioclase/total plagioclase would decrease smoothly with inferred depth in the basaltic chamber.

The above data are consistent with a model of interaction between Le Conte basaltic magma and both rhyodacitic liquid and crustal source rocks. Owing to these interactions the Le Conte basalt may represent a contaminated magma.

#### Geochemical Evidence

Petrographic data indicate that the Le Conte basalts may be hybrid liquids produced from the partial mixing of rhyodacitic liquid with basaltic liquid. I have attempted to model this process geochemically using the least-squares petrologic mixing program described by Bryan et al. (1969) and Wright and Doherty (1970). The modeling

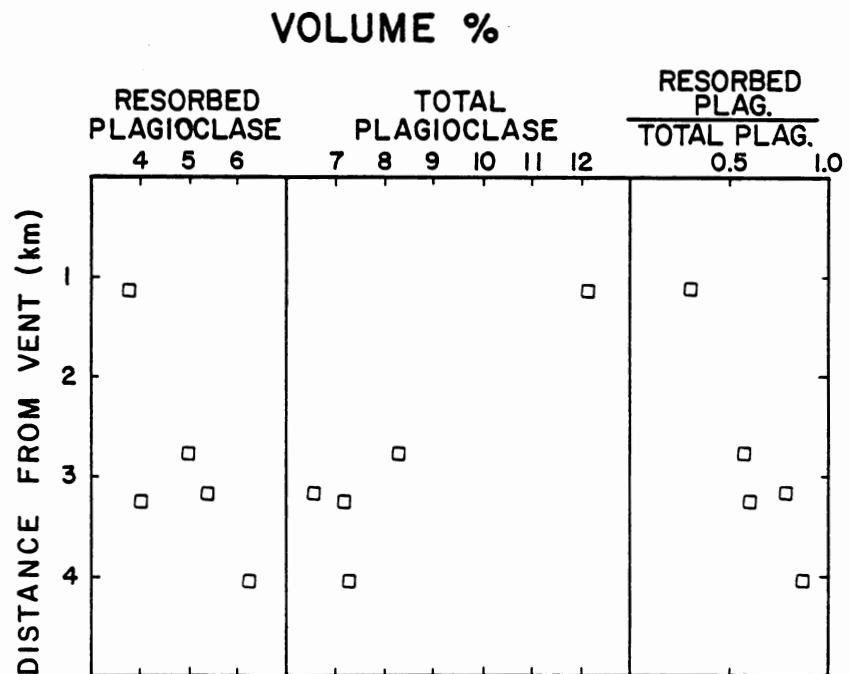


Figure 34. Proportions of resorbed and total plagioclase in the Le Conte basalt flow ( $H_{0BS}$ ) versus distance from the vent.

involves the calculation by computer of mafic and silicic end-member mixing proportions, as well as proportions of phenocrysts (olivine and plagioclase) separated from the basalt during the mixing process. The chosen parental basalt was SS-252, an olivine basalt from Cayuse Crater, and the chosen contaminant was SS-123, a rhyodacite from a  $\text{Ho}_{\text{rda}}$  dome. Olivine and plagioclase phenocrysts were included in the calculation because they occur in the basaltic rocks and may have fractionated from the basaltic liquid during the mixing-assimilation process. Sample SS-186 is the Le Conte basaltic composition that the calculations attempted to reproduce. Results of the calculations and analyses of the components appear in Table 7. The mixing model yields a marginally acceptable fit, with a  $\Sigma r^2$  value of 1.3. The model suggests that the fractionation of about 4% olivine and 4% plagioclase from uncontaminated basalt with the addition of about 15% rhyodacitic contaminant is capable of producing a hybrid basalt similar in composition to the Le Conte basalt.

Trace element abundances in parental and hybrid liquids are sensitive indicators of the validity of models calculated from major element abundances. Table 7 also lists the observed trace element abundance in Le Conte basalt (SS-186) versus those predicted from the major element mixing model. The predicted trace element abundance

TABLE 7.

MAGMA MIXING - FRACTIONATION MODEL FOR BASALTIC ROCKS  
FROM LE CONTE CRATER

SS-252 is a basalt from Cayuse Crater  
SS-123 is the assumed rhyodacitic ( $Ho_{rda}$ ) contaminant, and  
SS-186 is the hybrid basalt from Le Conte Crater

## INPUT DATA:

	<u>252</u>	<u>123</u>	<u>AN83</u>	<u>FO88</u>	<u>186</u>
SiO <sub>2</sub>	51.610	72.950	47.030	39.710	54.730
TiO <sub>2</sub>	1.150	.350	.001	.001	1.520
Al <sub>2</sub> O <sub>3</sub>	16.440	14.630	33.830	.001	16.480
Fe <sub>2</sub> O	.001	.001	.001	.001	.001
FeO	8.470	2.200	.001	11.350	8.090
MgO	8.810	.430	.001	48.680	6.190
CaO	9.430	1.750	16.850	.001	7.520
Na <sub>2</sub> O	3.080	4.540	1.860	.001	3.690
K <sub>2</sub> O	.600	3.010	.040	.001	1.210
P <sub>2</sub> O <sub>5</sub>	.220	.080	.001	.001	.370

## RESULTS:

	<u>Y OBS.</u>	<u>Y EST.</u>	<u>DIFF.</u>
SiO <sub>2</sub>	54.730	54.859	.129
TiO <sub>2</sub>	1.520	1.117	-.403
Al <sub>2</sub> O <sub>3</sub>	16.480	15.939	-.541
Fe <sub>2</sub> O	.001	.001	.001
FeO	8.090	7.692	-.398
MgO	6.190	6.178	-.012
CaO	7.520	8.275	.755
Na <sub>2</sub> O	3.690	3.441	-.249
K <sub>2</sub> O	1.210	.997	-.213
P <sub>2</sub> O <sub>5</sub>	.370	.215	-.155

AVERAGE: .29

SUM SQ: 1.3

TABLE 7. (Continued)

<u>VECTOR</u>	<u>COEFF.</u>
252	.9263
123	.1470
AN83	-.0426
FO88	-.0420
TOTAL:	.989

TRACE ELEMENTS

	<u>Predicted</u>	<u>Observed</u>
Rb	20.2	20
Sr	432	420
Zr	128	154
Ba	321	332
Ni	130	123
Cr	50	53

values are in close agreement with the observed values, except for Zr, which differs by about 19%. The data suggest that the Le Conte basalts are hybrid liquids produced during the interaction between primitive olivine basalts and rhyodacitic liquid of crustal derivation.

### Thermal Balance

The heat requirements to partially fuse crustal material and produce rhyodacitic liquids can be met if the amount of basalt available could have provided sufficient heat to fuse the necessary volume of crustal material.

The thermal balance is given by the equation:

$$\begin{array}{l} \text{cooling of} \\ \text{basalt} \end{array} + \begin{array}{l} \text{heat of} \\ \text{crystallization} \end{array} = \begin{array}{l} \text{heating of} \\ \text{crustal} \\ \text{rocks} \end{array} + \begin{array}{l} \text{heat of} \\ \text{fusion} \end{array} ,$$

$$\text{or } \rho^{bs} C_p^{bs} V^{bs} (\Delta T^{bs} + L/C_p^{bs}) = \rho^{cr} C_p^{cr} V^{cr} (\Delta T^{cr} + H/C_p^{cr}),$$

where  $\rho$  = density,  $C_p$  = specific heat,  $V$  = volume,  $L$  = latent heat of crystallization,  $H$  = heat of fusion,  $\Delta T$  = crystallization or heating interval, and the superscripts bs and cr refer to basalt and crustal rocks, respectively.

This equation can be simplified to

$$V^{cr} \leq \frac{\Delta T^{bs}}{\Delta T^{cr}} V^{bs}$$

because  $C_p$  and  $\rho$  change by only a few percent over a wide compositional range, and  $L$  and  $H$  are of similar magnitude (Myers and Marsh, 1981). The volume of crustal rocks that

can be melted is a function of the volume of basalt available, the cooling interval of that basalt, and the temperature interval over which the crustal rocks must be heated.

If we assume that the rhyodacitic liquids were segregated in situ upon crustal fusion at a depth of 9 km (3 Kb), and that the thermal gradient was  $50^{\circ}/\text{km}$ , then the crustal rocks were initially at a temperature of about  $450^{\circ}\text{C}$ . If the dry solidus of the crustal rocks was  $1000^{\circ}\text{C}$ , then  $\Delta T^{\text{cr}} = 550^{\circ}\text{C}$ . In a previous section it was shown that the basalts cooled about  $70^{\circ}$  prior to eruption ( $1220^{\circ}\text{C}$  to  $1150^{\circ}\text{C}$ ) and  $\Delta T^{\text{bs}} = 70^{\circ}$ . Using these values in the simplified thermal balance equation, the basalt could have melted approximately 13% of its volume of crustal rocks. This estimate is a maximum value and assumes no other heat loss and efficient thermal transfer from the basalt to the crustal rocks.

$30 \text{ km}^3$  of post-glacial basaltic rocks were erupted within a 10 km radius of post-glacial rhyodacitic activity at South Sister. If this figure represents half of the total basalt actually intruded, nearly  $8 \text{ km}^3$  of crustal rocks could have been melted. The volume of erupted post-glacial rhyodacite is only  $0.5 \text{ km}^3$ ; thus it appears that the volume of erupted basalt was entirely capable of producing enough heat to fuse crustal rocks and generate the rhyodacites. Because the post-glacial rhyodacites are

spatially restricted to areas underlain by the early rhyodacites, the intrusive equivalent of the early rhyodacites seems the most likely candidate as the crustal rock source for the post-glacial rhyodacites.

#### Early Bimodal Volcanism ( $Ps_{bs}$ - $Ps_{rda}$ )

The post-glacial divergent suite at South Sister was formed by interaction of mantle-derived basaltic magma with silicic crustal rocks. Similar eruptive sequences and compositions of the early and post-glacial divergent associations suggest a comparable origin for the early divergent suite. The early rhyodacites followed eruptions of large volumes of basaltic magma which form the underlying shield. It is reasonable to infer that the basaltic magmas provided an adequate heat source with which to melt older Tertiary plutonic rocks. The liquids produced from this crustal anatexis erupted as the early rhyodacites at South Sister and Obsidian Cliffs. The existence of the postulated early Tertiary plutonic source rocks at depth beneath the Three Sisters area is supported by the presence of partially fused plutonic xenoliths in the compositionally-zoned basaltic flow from Collier Cone. The post-glacial rhyodacites ( $Ho_{rda}$ ) contain plagioclase xenocrysts thought to represent solid residue from the source rocks. The apparent lack of similar xenocrysts and xenoliths in the

early rhyodacites may indicate that these rhyodacites were formed by complete melting of their crustal source rocks.

### Physical Model

Physical and petrogenetic models for the divergent suites at South Sister must be consistent with the following observations:

1. The eruption of the rhyodacites after the basalts.
2. The concentration of the rhyodacites in the center of a field of basaltic lavas.
3. The spatial restriction of post-glacial rhyodacites to terrain underlain by early rhyodacites.
4. Enrichments in incompatible trace element ratios in post-glacial rhyodacites relative to early rhyodacites.
5. Quartz xenocrysts in the Le Conte basalts.
6. Disequilibrium plagioclase phenocryst textures in post-glacial basalts and rhyodacites.
7. Apparent lack of intervening lavas of intermediate composition, and the resultant compositional gap of 16 weight percent  $\text{SiO}_2$ .

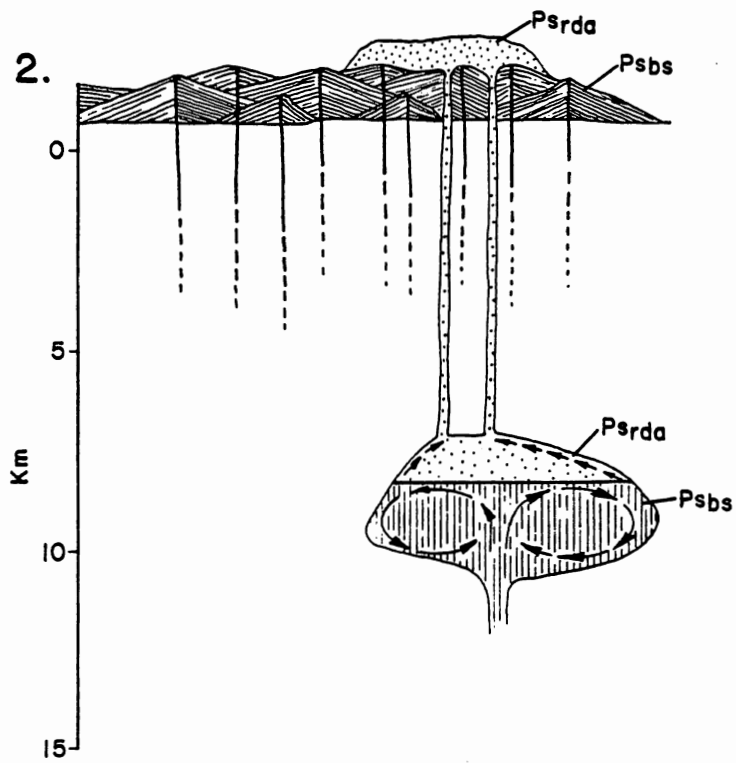
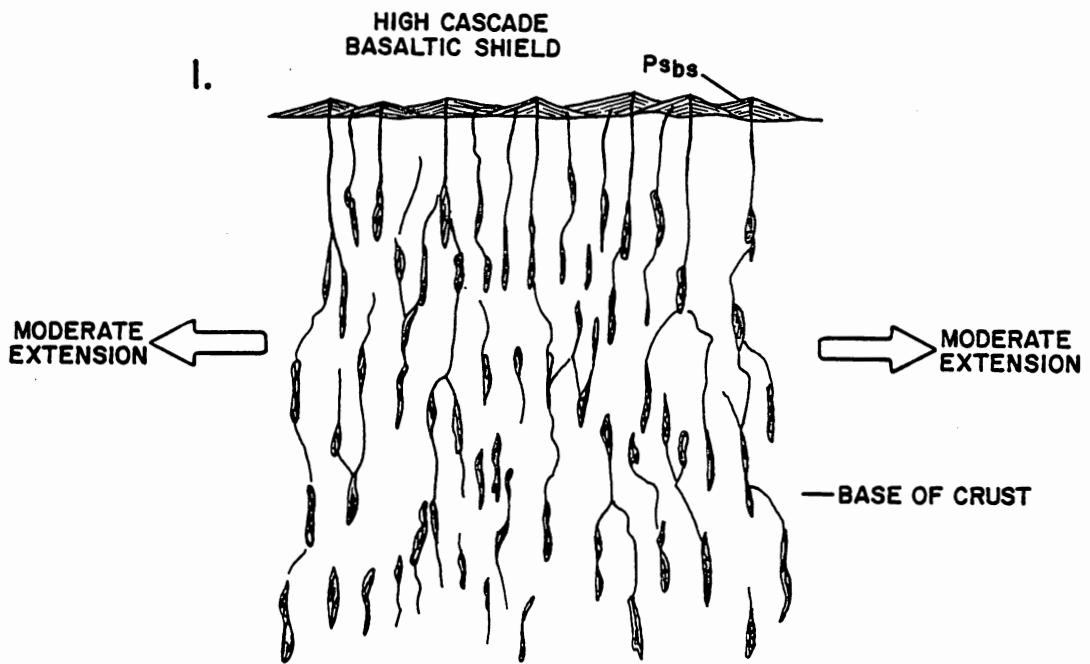
### Evolution of the Divergent Suites

Figure 35 outlines the proposed evolution of the South Sister volcanic complex in general, and the early and post-

glacial divergent suites in particular. This proposed evolution is as follows:

1. Large volumes of basaltic magma were produced by partial melting of the mantle in response to waning subduction off the Oregon coast and accelerating crustal extension in the Pacific Northwest. These basaltic magmas ascended rapidly and with little modification, as indicated by their high abundances of Ni and Cr relative to basaltic rocks from the High Cascade composite volcanoes. The basalts erupted to form an extensive platform of coalescing shield volcanoes.
2. Injection of basalt into the crust provided the heat necessary to fuse a small volume of Tertiary plutonic rocks beneath the present site of South Sister. The resultant melt was of rhyodacitic composition and, being more buoyant than the basaltic liquid, accumulated in a differentiated zone overlying the basaltic chamber. These rhyodacites erupted as the  $Ps_{rda}$  unit, which underlies the main cone sequence at South Sister.
3. A temporary lowering of the rate of crustal extension allowed the eruption of a more typical calc-alkaline sequence, the main ( $Ps_{ad}$ ) and summit ( $Ps_{ba}$ ) cone lavas. The andesites, dacites and

Figure 35. Schematic representation of the sequential geological evolution of the South Sister volcanic complex. See text for explanation.



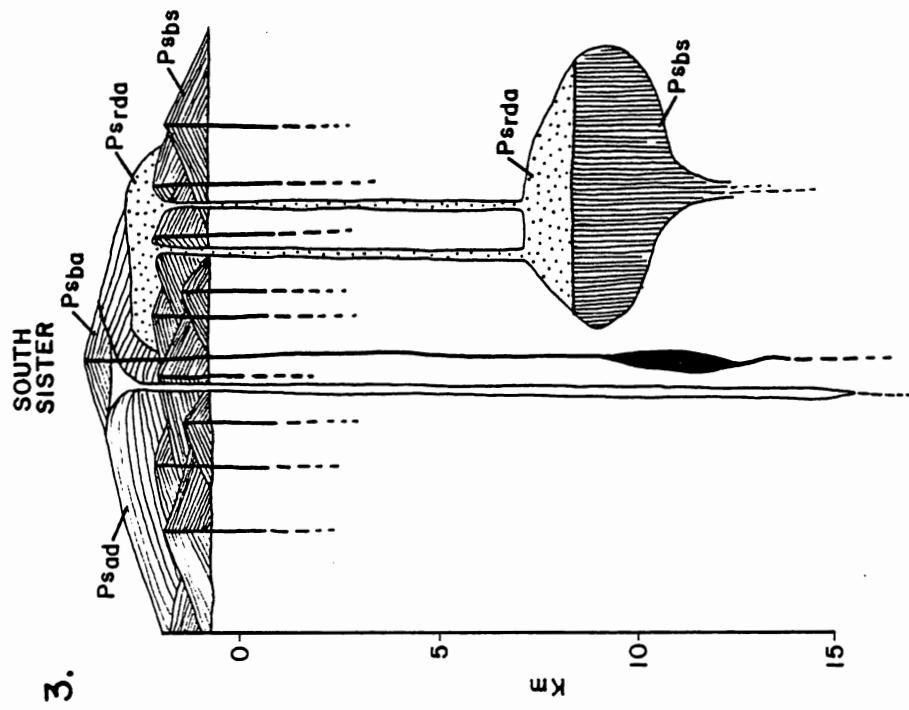
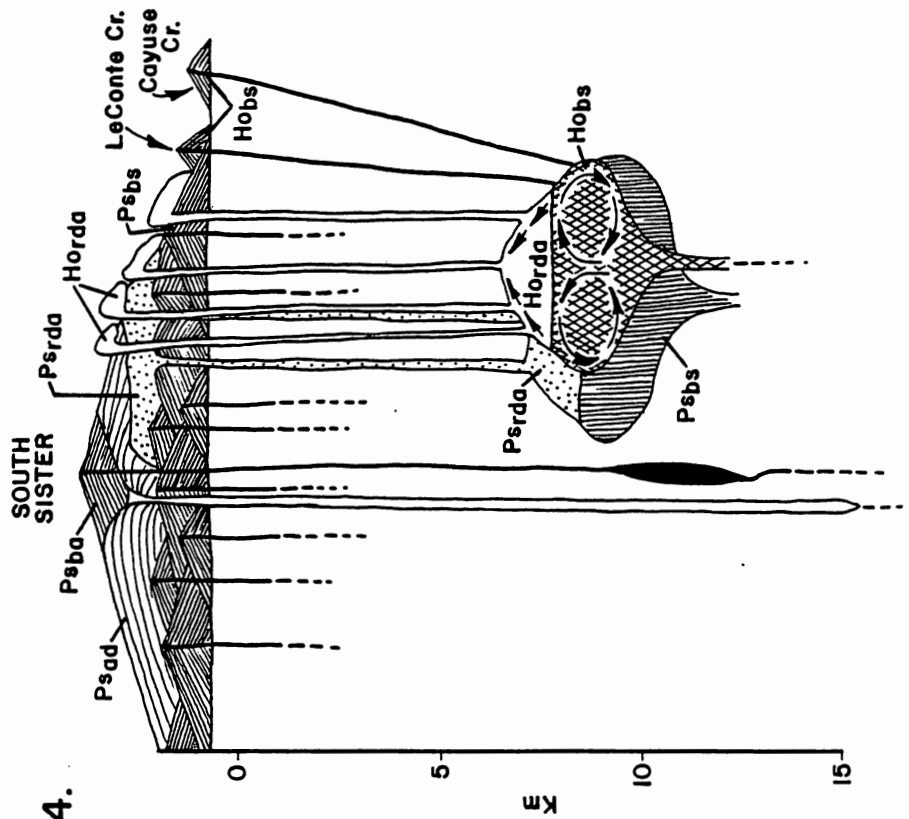


Figure 35. (Continued)

basaltic andesites apparently ascended as discrete magma batches, perhaps with some interaction with crustal rocks. Minor interbedded basaltic lavas are strongly depleted in Ni and Cr relative to the shield basalts, and have probably undergone extensive olivine fractionation upon ascent.

4. Renewed crustal extension resulted in intrusion of additional basaltic magma from the mantle beneath South Sister. The basalts ascended rapidly and preserved characteristically high Ni and Cr abundances similar to those of the shield basalts ( $Ps_{bs}$ ). Basaltic magmas ponded at shallow levels (8-10 km) beneath the South Sister complex and were emplaced in contact with the solidified intrusive equivalent of the early rhyodacites ( $Ps_{rda}$ ). Crystallization and convection within the basaltic chamber transferred heat to the silicic intrusive rocks. Partial melting of the intrusive rocks by the post-glacial basaltic magmas resulted in a stratified magma chamber in which buoyant rhyodacitic magma overlay denser basaltic magma. Limited mixing between basaltic and rhyodacitic magmas at the interface between upper and lower zones produced the hybrid Le

Conte basalts ( $Ho_{bs}$ ), which erupted along the flank of South Sister. The chamber was tapped eccentrically, and relatively unmodified basalts erupted from Cayuse Crater ( $Ho_{bs}$ ). Finally, the post-glacial rhyodacitic chamber was tapped to form domes along fissures on the south flank of the volcano.

This petrogenetic scheme for the evolution of the South Sister complex is consistent with available geological, geochemical, and petrographic data. The divergent volcanic suites at South Sister result from extensive shallow interaction between ascending basaltic magmas and silicic crustal rocks. The physical processes inherent in this model are explored in the last section.

#### Melting, Mass Transfer, and Accumulation of Silicic Liquid

Interaction between basaltic magmas and silicic crustal rocks may have produced a magma chamber stratified in both density and composition, with heavy basaltic liquid directly overlain by lighter, rhyodacitic liquid. A model for magma chamber stratification proposed by McBirney (1980) is consistent with observations at South Sister. In this model, melting of felsic wall rocks at the margins of a basaltic chamber leads to an upward migration of a light, felsic liquid in a thin boundary-layer. The

buoyant boundary-layer liquid accumulates at the apex of the chamber, where it directly overlies the dominant volume of basaltic magma. As the accumulated volume of rhyodacitic liquid increases, the interface separating the two liquids descends. The assumed domical geometry of the chamber, coupled with the density contrast and high viscosity of the silicic liquid may act to inhibit convective homogenization and result in a stably stratified upper silicic zone overlying an actively convecting basaltic lower zone of much greater volume. Alternatively, the two end-member liquids may develop independent convective cells, depending upon the physical characteristics of the magmas involved and the size and geometry of the chamber.

A rigorous, theoretical treatment of the physical and fluid dynamical processes that gave rise to the rhyodacites at South Sister is not possible owing to the complexity of evaluating competing processes. As a first approximation, however, it may prove useful to examine fluid dynamic properties estimated for divergent magmas at South Sister, in order to see how these properties might have influenced the development and behavior of the rhyodacitic upper zone.

Physical parameters, either calculated from thermodynamic data in a previous section or estimated from data on magmas similar to the South Sister rhyodacites, can be used in conjunction with the relevant equations to deter-

mine the physical behavior of the divergent magmas at South Sister. The physical and fluid dynamic properties of the South Sister post-glacial rhyodacitic magmas are tabulated in Table 8. These calculations assume that the magma chamber has a hemispherical geometry with a radius and vertical dimension of 1 kilometer ( $10^5$  cm) and a depth/diameter ratio of 0.5. The rhyodacitic chamber volume is then  $2.1 \text{ km}^3$ , a reasonable figure in view of the calculated eruptive volume of post-glacial rhyodacites of  $0.5 \text{ km}^3$ . The theoretical configuration of the magma chamber is illustrated in Figure 36. Figure 36 shows the ascending felsic boundary-layer liquid which accumulates in the upper silicic zone and the convecting basaltic lower zone. Also shown is a velocity profile relative to an arbitrary horizontal reference level. The convecting basalt provides the heat necessary for thermal ablation of the chamber walls, and the ascent of the boundary-layer into the rhyodacitic upper zone is controlled by the diffusion of components melted from the wall rock into the felsic boundary-layer. Depending upon the physical properties of the rhyodacite and the chamber dimensions, the upper zone may be stably stratified or convecting independently of the lower basaltic zone. Using the appropriate fluid dynamic properties, it is possible to calculate the width of the compositional and thermal boundary-layers at the top of

TABLE 8.

CALCULATED PHYSICAL AND FLUID DYNAMIC PROPERTIES  
FOR THE Ho<sub>rda</sub> MAGMA CHAMBER

$$\rho = 2.262 \text{ g cm}^{-3} \text{ (@875}^\circ\text{C, 3 Kb)}$$

$$\eta = 1.38 \times 10^6 \text{ poise (@ 875}^\circ\text{C)}$$

$$T \text{ (interior of Ho}_{rda} \text{ chamber)} = 875^\circ\text{C}$$

$$T \text{ (ambient in wall rocks)} = 450^\circ\text{C (9 Km x 50}^\circ\text{C/Km)}$$

$$T \text{ (@ upper contact of rda with wall rocks)} = (875 + 450)/2 \\ = 663^\circ\text{C}$$

$$T \text{ (@ basalt-rhyodacite interface)} = 1160^\circ\text{C}$$

$$Z \text{ (vertical chamber dimension)} = 10^5 \text{ cm (1 Km)}$$

$$L \text{ (chamber radius)} = 10^5 \text{ cm}$$

$$\gamma \text{ (vertical temperature gradient in } ^\circ\text{C/cm)} = 0.005^\circ\text{C/cm}$$

$$\beta \text{ (coefficient of compositional expansion)} = 5.1 \times 10^{-4} \text{ deg}^{-1}$$

$$\kappa \text{ (thermal conductivity)} = 5 \times 10^{-3} \text{ cal cm}^{-1} \text{ sec}^{-1} \text{ deg}^{-1}$$

$$K \text{ (thermal diffusivity)} = \kappa / \rho C_p \\ = 7 \times 10^{-3} \text{ cm}^2 \text{ sec}^{-1}$$

$$C_p \text{ (heat capacity)} = 0.3 \text{ cal gm}^{-1} \text{ deg}^{-1}$$

$$\alpha \text{ (coefficient of thermal expansion)} = 5 \times 10^{-5} \text{ deg}^{-1}$$

$$\nu \text{ (kinematic viscosity in stokes)} = \eta / \rho \\ = 6.1 \times 10^5 \text{ cm}^2 \text{ sec}^{-1}$$

$$D \text{ (chemical diffusivity)} \approx 10^{-7} \text{ cm}^2 \text{ sec}^{-1}$$

$$\text{Pr (Prandtl number)} = \nu / K \\ = 8.7 \times 10^7$$

$$\text{Sc (Schmidt number)} = \nu / D \\ = 6 \times 10^{12}$$

TABLE 8. (Continued)

$$\begin{aligned} \text{Gr (Grashof number)} &= g\alpha\gamma L^4/v^2 \\ &= 6.6 \times 10^4 \end{aligned}$$

$$\begin{aligned} \text{Gr}^c \text{ (compositional Grashof number)} &= g\beta\alpha L^4/v^2 \\ &= 6.7 \times 10^5 \end{aligned}$$

$$\text{Ra} = \text{Pr} \cdot \text{Gr} = 5.7 \times 10^{12}$$

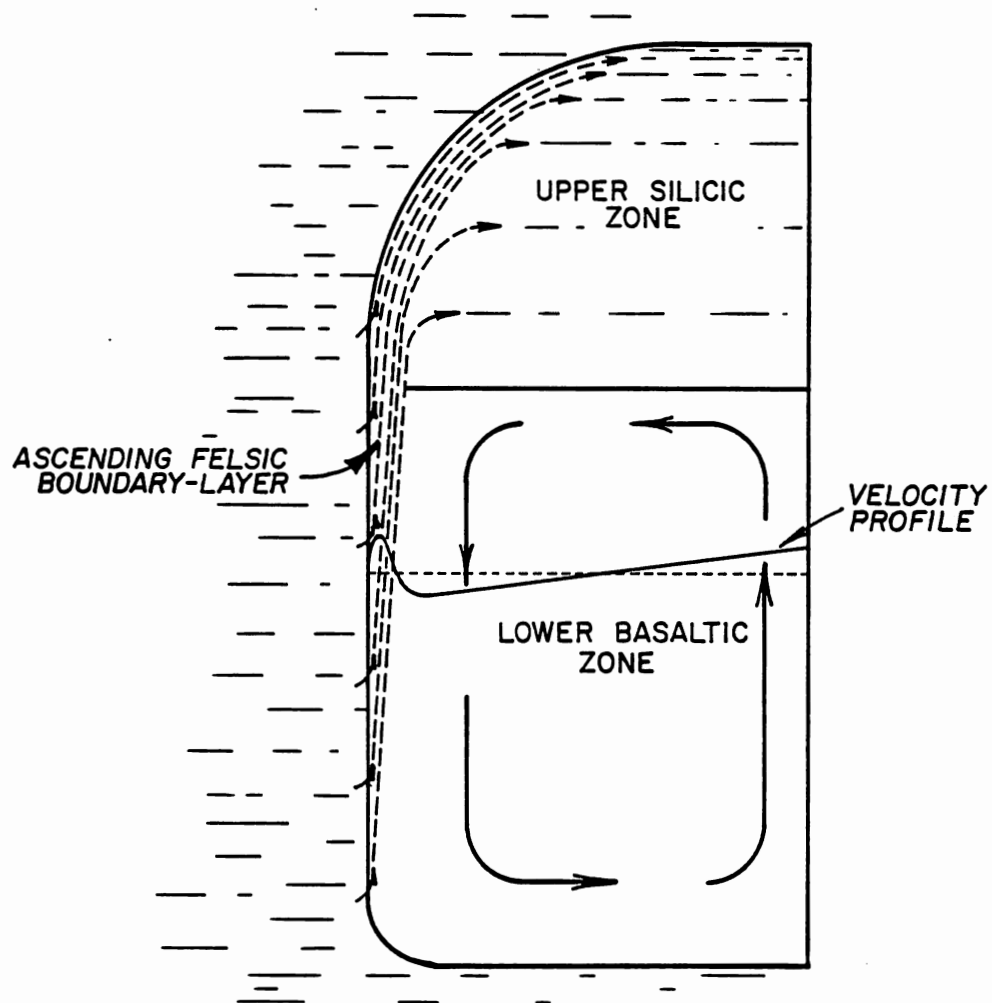


Figure 36. Schematic view of a compositionally-stratified magma chamber from which bimodal igneous associations might erupt. See text for explanation. After McBirney (unpublished manuscript).

the chamber, the convective velocity of the compositional boundary-layer, and the rate of accumulation of the rhyodacitic component in the upper zone. Laminar flow is assumed in all cases. These calculations are greatly simplified and do not take into account the changes in the above parameters as a function of time in a cooling body. The calculations do allow us, however, to see what values of these functions might be expected in a small system, such as that at South Sister. The appropriate equations are taken from Skelland (1974) and Rohsenow and Choi (1961).

The width of the compositional boundary layer is given by:

$$\delta_C = 4 (Gr')^{-\frac{1}{4}} (Sc)^{-\frac{1}{4}} \cdot Z \quad , \text{ where}$$

$Gr'$  is the compositional Grashof number,  $Sc$  is the Schmidt number, and  $Z$  is the vertical distance along the chamber wall. Using the values of  $Gr'$  and  $Sc$  from Table 8 at  $Z = 10^5$  cm, the width of the compositional boundary layer is 9 cm. Because heat diffuses faster than chemical components, the thermal boundary layer will be wider than the compositional boundary layer. The width of the thermal boundary layer is given by:

$$\delta_T = 4 (Gr)^{-\frac{1}{4}} (Pr)^{-\frac{1}{4}} \cdot Z \quad , \text{ where}$$

$Gr$  is the Grashof number and  $Pr$  is the Prandtl number.

At  $Z = 10^5$  cm, the width of the thermal boundary layer is

258 cm.

The maximum convective velocity of the compositional boundary-layer is given by the expression:

$$\mu_{\max} = 0.766 \frac{\nu}{Z} (\text{Sc})^{-\frac{1}{2}} (\text{Gr})^{\frac{1}{2}}, \text{ where}$$

$\nu$  is the kinematic viscosity, and other symbols and values are as above. At  $Z = 10^5$  cm, the convective ascent velocity of the compositional boundary-layer is  $4.9 \times 10^{-4}$  cm  $\text{sec}^{-1}$ , or about 2 cm/hr.

The accumulation rate ( $Q$ ) of rhyodacitic liquid in the upper zone in cubic centimeters per second per centimeter of chamber circumference can be calculated from the equation:

$$Q = 0.677 (\text{Gr}')^{\frac{1}{4}} (\text{Sc})^{\frac{1}{4}} \cdot D, \text{ where}$$

$\text{Gr}'$  and  $\text{Sc}$  are the compositional Grashof and Schmidt numbers, respectively, and  $D$  is the chemical diffusivity.

Using the values from Table 8, the accumulation rate of rhyodacitic liquid in the upper zone is  $3 \times 10^{-3}$   $\text{cm}^3 \text{sec}^{-1}$  per centimeter of chamber circumference, or  $3 \times 10^{-5}$   $\text{km}^3 \text{yr}^{-1}$  ( $30,000 \text{ m}^3 \text{yr}^{-1}$ ) over the entire chamber. At this rate 70,000 years would be required to generate the  $2.1 \text{ km}^3$  volume estimated for the post-glacial rhyodacitic chamber at South Sister by the boundary-layer accumulation process alone, and 16,000 years would be required to generate the observed erupted volume of post-glacial rhyodacites of  $0.5 \text{ km}^3$ . The eruption of the rhyodacites followed that of

the basalts by no more than 10,000 years, but the rates calculated are probably minimum estimates. Ascent of rhyodacitic liquid melted from stopped blocks of crustal rocks through the interior of the chamber could significantly augment the boundary-layer accumulation of silicic liquid in the upper zone. In any case, the time-scale required for these processes to generate the observed volumes of silicic liquid is of the right order of magnitude and consistent with rates estimated by Smith (1979) and Spera and Crisp (1981).

Whether the upper zone is stably stratified or convecting is dependent upon the Rayleigh number (Ra), which is given by the expression:

$$Ra = Pr \cdot Gr \quad , \text{ where}$$

Pr and Gr are the Prandtl and Grashof numbers, respectively. Using the values from Table 8, the calculated Ra is  $5.7 \times 10^{12}$ . The Rayleigh number for the South Sister post-glacial rhyodacitic chamber exceeds the threshold value of 1700, and the chamber was probably convecting. Because the laminar to turbulent flow transition in silicic magma chambers with the dimensions considered here (depth/diameter  $\approx 0.5$ ) takes place at Rayleigh numbers greater than about  $10^{13}$  (Hardee and Larson, 1977), the convective flow in the rhyodacitic chamber was probably laminar. The maximum thermal convective velocity can be estimated from the

equation:

$$\mu_{\max} = 0.766 \frac{v}{Z} (\text{Pr})^{-\frac{1}{2}} (\text{Gr})^{\frac{1}{2}} .$$

Using the appropriate values from Table 8 the convective velocity is 460 cm/hr. This convective velocity is low compared to convective velocities calculated for larger silicic systems (Ewart et al, 1975).

### Petrologic Implications

The intrusive equivalents of the early rhyodacites ( $\text{Ps}_{\text{rda}}$ ) were the most likely source rocks partially melted to generate the post-glacial rhyodacites ( $\text{Ho}_{\text{rda}}$ ). If this assumption is valid, then enrichments of excluded elements in the post-glacial rhyodacites suggest that these lavas result from 75-90% partial melting of the  $\text{Ps}_{\text{rda}}$  source rocks. Steep linear gradients with respect to Rb/K vs. Rb, Rb/Zr vs. Rb, and Rb/Ba vs. Rb suggest that successive partial melts segregated by density in the upper zone of the stratified chamber maintained their compositional integrity during their residence time in the chamber. These data are consistent with the eruption of the post-glacial rhyodacites from a stably stratified upper zone in the magma chamber. Using this reasoning, the succession of rhyodacitic domes that erupted along a north-trending fissure at between 8000 feet and 5500 feet elevation would represent liquids tapped from successive levels in the

stably stratified chamber, and trace element enrichment should show a good degree of correlation with the structural height of the domes, analagous to geochemical patterns in compositionally-zoned ignimbrite sheets (Hildreth, 1979, 1981). Plots of Rb/K, Rb/Zr, and Rb/Ba versus structural height of the rhyodacitic domes show no such correlation (Figure 37). The lavas do not appear to have tapped successive levels in a stably stratified rhyodacitic magma chamber.

However, arguments based on the calculated Rayleigh number for the post-glacial rhyodacitic chamber indicate that the chamber was convecting, though very slowly. The slow convection, coupled with low chemical diffusivities and high viscosities, enabled successive partial melts to maintain their distinctive trace element ratios in the convecting chamber. The characteristic trace element ratios are frozen in upon eruption. Liquids erupted from this convective system would be expected to show no correlation of trace element enrichment with location of the domes along the chain, which, of course, they do not.

### Conclusion

The divergent suites at South Sister developed as a result of extensive interaction between basaltic magmas and silicic crustal rocks. The post-glacial divergent magmas

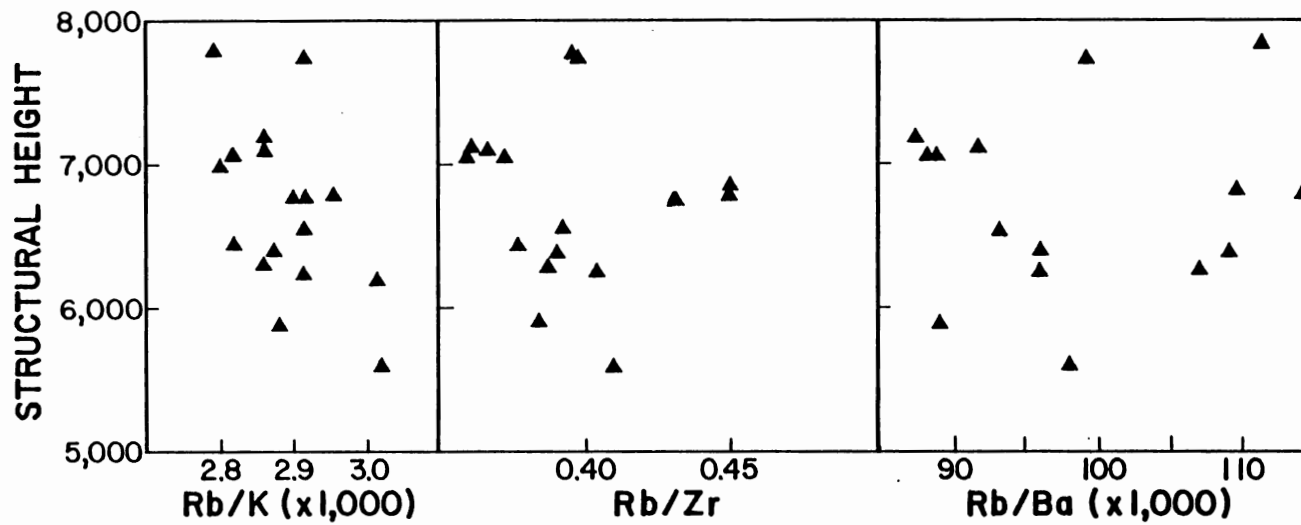


Figure 37. Variations of trace element ratios in post-glacial rhyodacitic domes ( $Ho_{rda}$ ) with structural height.

erupted from a compositionally stratified magma chamber in which dense basaltic liquid was overlain by buoyant rhyodacitic liquid produced from partial melting of the intrusive equivalent of the early rhyodacites. The lower zone convected vigorously, and the upper zone convected more slowly. The upper zone accumulated both by ascent of a buoyant, rhyodacitic boundary-layer as the chamber walls underwent thermal ablation, and by the ascent of buoyant liquid through the chamber interior from the melting of stoped crustal blocks. This model differs from the fractional crystallization model presented by Ritchey (1979, 1980) for the divergent suite at Crater Lake, Oregon. The apparent validity of both models suggests that more than one genetic process can give rise to bimodal igneous associations.

## APPENDIX A.

## MODAL ABUNDANCES OF PHENOCRYSTS IN LAVAS FROM SOUTH SISTER VOLCANO

Sample	<u>151</u>	<u>154</u>	<u>158</u>	<u>161</u>	<u>198</u>	<u>200</u>	<u>206</u>	<u>88a</u>	<u>90a</u>	<u>101</u>	<u>106</u>
plag	9.0	11.2	19.0	19.5	14.8	17.8	17.0	13.4	11.4	4.9	6.4
ol	0.1	----	0.7	----	2.7	0.2	3.4	----	----	---	---
cpx	1.7	1.8	1.2	1.4	1.1	2.8	1.0	----	----	---	---
opx	1.7	1.3	---	1.2	---	2.9	---	1.2	0.9	0.5	0.5
amph	---	---	---	---	---	---	---	0.1	---	---	---
opaques	0.3	0.7	---	0.1	---	1.5	0.2	0.6	1.0	0.4	0.2
groundmass	87.2	85.0	79.1	77.8	81.4	74.8	78.4	84.7	86.7	94.2	92.9
Total	100.0	100.0	100.0	100.0	100.0	100.0	100.0	100.0	100.0	100.0	100.0

Sample	<u>134</u>	<u>148</u>	<u>172</u>	<u>248</u>	<u>250</u>	<u>109</u>	<u>185</u>	<u>187</u>	<u>192</u>	<u>207</u>	<u>251</u>
plag	10.8	1.9	11.0	7.9	9.6	12.2	8.3	6.6	7.2	7.2	2.2
ol	----	---	----	---	---	3.9	4.0	2.1	2.4	3.3	20.3
cpx	----	---	----	---	---	---	---	---	---	---	----
opx	1.0	---	1.3	1.2	1.2	---	---	---	---	---	----
amph	---	---	0.2	---	---	---	---	---	---	---	----
opaques	0.6	---	0.7	0.5	0.4	---	---	---	---	---	----
groundmass	87.6	98.1	86.8	90.4	88.8	83.9	87.7	91.3	90.2	89.5	77.5
Total	100.0	100.0	100.0	100.0	100.0	100.0	100.0	100.0	100.0	100.0	100.0

APPENDIX A. (Continued)

Sample	<u>253</u>	<u>96</u>	<u>97</u>	<u>98</u>	<u>99</u>	<u>100</u>	<u>102</u>	<u>103</u>	<u>104</u>	<u>105</u>	<u>107</u>
plag	1.7	4.7	13.2	12.6	8.0	9.0	9.3	10.9	7.4	13.0	10.7
ol	8.8	---	----	----	---	---	---	----	---	----	----
cpx	---	---	----	----	---	---	---	----	---	----	----
opx	---	0.8	1.7	2.0	1.2	1.7	0.8	1.2	0.7	1.5	1.0
amph	---	---	---	0.1	0.1	0.1	---	---	---	---	---
opaques	---	0.4	0.7	0.9	0.7	0.6	0.7	0.6	0.5	0.8	0.8
groundmass	89.5	94.1	84.4	84.4	90.0	88.6	89.2	87.3	91.4	84.7	87.5
Total	100.0	100.0	100.0	100.0	100.0	100.0	100.0	100.0	100.0	100.0	100.0

Sample	<u>121</u>	<u>123</u>	<u>124</u>	<u>125</u>	<u>126</u>	<u>223a</u>	<u>223b</u>	<u>132</u>	<u>252</u>	<u>108b</u>
plag	8.3	9.4	10.9	8.2	7.4	15.3	5.3	11.0	1.3	7.7
ol	---	---	----	---	---	----	---	----	6.7	---
cpx	---	---	----	---	---	----	---	----	---	---
opx	1.5	1.5	1.6	1.4	1.3	1.6	0.7	0.9	---	1.5
amph	0.5	0.3	0.3	---	0.1	---	---	---	---	---
opaques	0.7	0.7	0.6	0.7	0.5	0.8	0.5	0.4	---	0.7
groundmass	89.0	88.1	86.6	89.7	90.7	82.3	93.5	87.6	92.0	90.1
Total	100.0	100.0	100.0	100.0	100.0	100.0	100.0	100.0	100.0	100.0

## APPENDIX B.

## BULK ROCK CHEMICAL ANALYSES

Analyses of major elements and most trace elements were done with a Varian (AA-175 series) atomic absorption spectrophotometer. Ferrous iron was determined by titration, and water contents of samples were measured with a Du Pont electronic moisture analyzer. Rb, Sr and Zr analyses were done by X-ray fluorescence using pressed powder pellets according to the method of Norrish and Hutton (1969). Duplicate and triplicate analyses of selected samples indicate analytical precision of better than 2% for  $\text{SiO}_2$ ,  $\text{TiO}_2$ ,  $\text{Fe}_2\text{O}_3$ ,  $\text{MgO}$ ,  $\text{CaO}$ ,  $\text{Na}_2\text{O}$ ,  $\text{K}_2\text{O}$ , Rb, Sr, and Zr; 5% for  $\text{Al}_2\text{O}_3$ , and Ni; 10% for  $\text{MnO}$ ,  $\text{P}_2\text{O}_5$ , Ba, and Cr.

APPENDIX B. (Continued)

Shield Basalts (Ps<sub>ba</sub>)

	<u>SS-1</u>	<u>SS-4</u>	<u>SS-8</u>	<u>SS-40</u>	<u>SS-47</u>
SiO <sub>2</sub>	51.15	52.12	54.74	52.09	50.41
TiO <sub>2</sub>	1.29	0.87	1.01	1.02	1.05
Al <sub>2</sub> O <sub>3</sub>	16.97	18.15	16.69	16.78	16.80
Fe <sub>2</sub> O <sub>3</sub>	5.68	3.72	3.19	4.25	6.46
FeO	3.89	4.66	4.72	5.03	3.56
MnO	0.15	0.12	0.13	0.15	0.15
MgO	5.15	6.66	5.67	6.64	7.19
CaO	9.83	9.34	8.08	9.67	9.27
Na <sub>2</sub> O	3.36	3.48	3.49	3.38	3.53
K <sub>2</sub> O	0.64	0.53	0.80	0.66	0.61
P <sub>2</sub> O <sub>5</sub>	0.33	0.13	0.30	0.32	0.28
H <sub>2</sub> O <sup>+</sup>	0.40	0.31	0.64	0.06	0.26
H <sub>2</sub> O <sup>-</sup>	0.26	0.41	0.44	0.14	0.25
Total	99.10	100.50	99.79	100.19	99.82
D.I.	-1.63	-2.13	0.00	-2.25	-2.60
Rb	5	5	9.6	7	7.5
Sr	522	627	738	533	446
Zr	132	77	162	133	114
Ba	280	196	362	269	226
Ni	97	110	146	91	146
Cr	239	144	199	153	189

APPENDIX C. (Continued)

Main Cone Andesites and Dacites (Ps<sub>ad</sub>)

	<u>SS-16</u>	<u>SS-21</u>	<u>SS-29</u>	<u>SS-30</u>	<u>SS-39</u>	<u>SS-42</u>	<u>SS-49</u>	<u>SS-50</u>
SiO <sub>2</sub>	52.56	62.58	64.59	60.48	63.51	64.28	63.70	64.31
TiO <sub>2</sub>	1.27	1.10	0.93	1.17	1.06	0.94	1.04	1.01
Al <sub>2</sub> O <sub>3</sub>	18.42	15.59	15.79	16.63	16.29	15.55	16.18	16.18
Fe <sub>2</sub> O <sub>3</sub>	2.80	1.98	2.12	2.52	2.36	1.72	1.45	1.54
FeO	6.65	3.94	3.25	4.18	3.91	3.85	4.19	4.14
MnO	0.14	0.10	0.11	0.12	0.11	0.12	0.12	0.12
MgO	5.02	1.96	1.45	2.43	1.27	1.38	1.69	1.64
CaO	8.80	4.38	3.70	4.94	4.56	3.85	4.36	4.28
Na <sub>2</sub> O	3.64	4.82	5.32	4.82	4.93	5.05	4.97	5.01
K <sub>2</sub> O	0.67	2.05	1.43	1.74	1.91	2.15	1.93	1.96
P <sub>2</sub> O <sub>5</sub>	0.23	0.26	0.32	0.28	0.29	0.32	0.30	0.30
H <sub>2</sub> O <sup>+</sup>	0.25	0.28	0.17	0.40	0.12	0.06	0.10	0.17
H <sub>2</sub> O <sup>-</sup>	0.19	0.13	0.26	0.26	0.21	0.09	0.17	0.10
Total	100.64	99.17	99.44	99.97	100.53	99.36	100.20	100.76
D.I.	-0.57	7.14	7.73	5.87	7.46	8.22	7.40	7.60
Rb	5.6	40.8	40.7	30	33.1	36.4	38	40
Sr	436	368	354	410	387	369	400	390
Zr	86	217	241	207	215	229	214	217
Ba	256	581	596	486	506	578	539	561
Ni	93	9	4	13	8	22	14	9
Cr	106	39	30	52	54	51	20	10

APPENDIX B. (Continued)

	<u>SS-51</u>	<u>SS-52</u>	<u>SS-53</u>	<u>SS-54</u>	<u>SS-55</u>	<u>SS-56</u>	<u>SS-57</u>	<u>SS-58</u>
SiO <sub>2</sub>	64.00	63.83	62.95	64.11	63.80	63.29	64.31	62.41
TiO <sub>2</sub>	1.09	1.12	1.11	1.10	1.09	0.93	1.09	0.93
Al <sub>2</sub> O <sub>3</sub>	16.57	16.13	16.67	16.23	16.79	16.62	15.74	16.67
Fe <sub>2</sub> O <sub>3</sub>	1.57	1.73	2.03	2.51	2.53	1.64	1.77	3.38
FeO	4.13	4.08	3.77	3.31	3.28	4.03	3.85	2.48
MnO	0.12	0.11	0.11	0.11	0.11	0.11	0.11	0.11
MgO	1.66	1.74	1.65	1.77	1.62	1.78	1.79	1.85
CaO	4.21	3.98	4.25	4.12	4.03	4.19	4.17	4.60
Na <sub>2</sub> O	5.06	4.99	4.96	4.87	4.88	4.90	5.01	4.95
K <sub>2</sub> O	1.99	2.03	1.94	1.95	1.97	1.98	1.97	1.95
P <sub>2</sub> O <sub>5</sub>	0.29	0.33	0.31	0.28	0.28	0.28	0.27	0.28
H <sub>2</sub> O <sup>+</sup>	0.10	0.18	0.26	0.03	0.03	0.07	0.20	0.02
H <sub>2</sub> O <sup>-</sup>	0.06	0.14	0.15	0.20	0.23	0.11	0.14	0.17
Total	100.85	100.39	100.14	99.33	100.64	100.29	100.42	99.69
D.I.	7.62	7.74	7.39	7.60	7.72	7.44	7.60	6.94
Rb	35	42	40	40	35	42	39	35
Sr	392	389	391	401	395	400	391	398
Zr	221	215	215	215	210	220	219	218
Ba	550	572	572	550	561	539	528	528
Ni	8	10	11	13	8	7	7	8
Cr	17	15	20	12	20	15	15	15

Appendix B. (Continued)

	<u>SS-59</u>	<u>SS-60</u>	<u>SS-61</u>	<u>SS-62</u>	<u>SS-63</u>	<u>SS-64</u>	<u>SS-65</u>	<u>SS-66</u>
SiO <sub>2</sub>	62.54	62.24	63.16	62.17	63.71	63.12	63.51	62.58
TiO <sub>2</sub>	1.26	1.00	1.27	1.08	0.97	1.11	0.96	1.29
Al <sub>2</sub> O <sub>3</sub>	16.78	16.72	16.62	16.88	16.57	16.57	16.06	16.42
Fe <sub>2</sub> O <sub>3</sub>	2.28	1.68	2.00	1.90	3.26	2.91	3.19	2.85
FeO	3.47	4.02	3.94	3.95	2.68	3.11	2.94	3.09
MnO	0.11	0.12	0.12	0.12	0.12	0.12	0.12	0.12
MgO	1.77	1.77	1.80	1.71	1.77	1.88	1.88	1.86
CaO	4.49	4.48	4.35	4.36	4.34	4.54	4.58	4.55
Na <sub>2</sub> O	4.90	4.81	4.93	4.87	4.96	4.89	4.89	4.85
K <sub>2</sub> O	1.94	1.91	1.93	1.90	1.87	1.83	1.87	1.79
P <sub>2</sub> O <sub>5</sub>	0.29	0.28	0.28	0.28	0.25	0.23	0.22	0.24
H <sub>2</sub> O <sup>+</sup>	0.02	0.19	0.13	0.07	0.05	0.28	0.27	0.31
H <sub>2</sub> O <sup>-</sup>	0.17	0.05	0.23	0.25	0.11	0.16	0.64	0.35
Total	100.02	99.27	100.76	99.54	100.66	100.75	101.13	100.30
D.I.	7.10	7.02	7.30	7.19	7.31	6.98	7.05	6.91
Rb	37	40	34	36	34	37	35	30
Sr	404	395	389	404	376	389	380	392
Zr	212	216	217	212	209	209	213	207
Ba	552	531	531	542	520	520	488	509
Ni	8	5	7	8	8	8	10	9
Cr	18	15	18	20	25	23	18	20

APPENDIX B. (Continued)

	<u>SS-67</u>	<u>SS-68</u>	<u>SS-69</u>	<u>SS-70</u>	<u>SS-71</u>	<u>SS-72</u>	<u>SS-73</u>
SiO <sub>2</sub>	63.46	62.36	63.87	62.94	62.91	63.32	63.48
TiO <sub>2</sub>	0.99	1.23	0.99	1.18	1.06	1.21	1.16
Al <sub>2</sub> O <sub>3</sub>	16.06	16.17	16.04	16.24	16.84	16.81	16.66
Fe <sub>2</sub> O <sub>3</sub>	2.34	2.40	1.73	1.69	2.36	3.34	3.10
FeO	3.55	3.48	4.12	4.14	3.59	2.57	2.86
MnO	0.12	0.12	0.12	0.11	0.11	0.12	0.11
MgO	1.91	1.89	1.96	1.99	1.89	1.91	1.78
CaO	4.52	4.34	4.48	4.49	4.50	4.67	4.33
Na <sub>2</sub> O	4.90	4.90	4.96	5.03	4.92	4.97	4.85
K <sub>2</sub> O	1.88	1.87	1.89	1.89	1.84	1.85	1.86
P <sub>2</sub> O <sub>5</sub>	0.23	0.23	0.22	0.23	0.22	0.24	0.23
H <sub>2</sub> O <sup>+</sup>	0.16	0.46	0.37	0.36	0.12	0.20	0.09
H <sub>2</sub> O <sup>-</sup>	0.22	0.19	0.23	0.21	0.17	0.19	0.21
Total	100.34	99.64	100.98	100.50	100.53	99.49	100.72
D.I.	7.07	7.03	7.12	6.97	7.06	6.92	7.27
Rb	35	35	38	36	31	36	31
Sr	385	371	382	384	407	394	383
Zr	206	214	214	206	208	211	207
Ba	498	531	509	498	488	498	498
Ni	10	8	6	7	7	8	9
Cr	23	18	16	20	24	22	24

APPENDIX B. (Continued)

	<u>SS-74</u>	<u>SS-80</u>	<u>SS-85</u>	<u>SS-86</u>	<u>SS-149</u>	<u>SS-151</u>	<u>SS-153</u>
SiO <sub>2</sub>	63.46	64.44	58.62	63.48	56.67	63.39	63.39
TiO <sub>2</sub>	0.81	0.89	0.98	1.03	1.57	0.97	1.15
Al <sub>2</sub> O <sub>3</sub>	15.61	15.98	16.90	16.42	17.59	16.05	16.06
Fe <sub>2</sub> O <sub>3</sub>	2.87	3.15	2.22	2.24	2.68	3.03	2.03
FeO	3.09	2.72	4.81	3.61	4.95	2.60	3.78
MnO	0.11	0.11	0.12	0.12	0.14	0.11	0.11
MgO	1.60	1.57	2.63	1.72	3.89	2.29	2.15
CaO	4.22	4.30	5.94	4.29	6.83	3.60	4.08
Na <sub>2</sub> O	4.77	4.78	4.23	4.98	4.38	4.57	4.70
K <sub>2</sub> O	1.95	1.99	1.31	1.89	1.11	1.85	1.97
P <sub>2</sub> O <sub>5</sub>	0.22	0.22	0.22	0.24	0.30	0.22	0.27
H <sub>2</sub> O <sup>+</sup>	0.12	0.07	0.10	0.14	0.13	0.17	0.17
H <sub>2</sub> O <sup>-</sup>	0.12	0.14	0.17	0.21	0.19	0.23	0.21
Total	98.95	100.36	98.25	100.37	100.43	99.08	99.97
D.I.	7.52	7.67	4.39	7.37	2.53	7.46	7.30
Rb	36	38	25	36	18	35	39
Sr	385	406	470	379	502	366	368
Zr	206	199	165	209	149	195	202
Ba	519	512	388	509	376	562	579
Ni	10	8	20	10	30	13	13
Cr	63	59	63	27	40	7	6

APPENDIX B. (Continued)

	<u>SS-154</u>	<u>SS-155</u>	<u>SS-156</u>	<u>SS-157</u>	<u>SS-158</u>	<u>SS-159</u>
SiO <sub>2</sub>	63.70	62.16	59.63	59.61	52.19	52.04
TiO <sub>2</sub>	1.11	0.97	1.41	1.52	1.61	1.27
Al <sub>2</sub> O <sub>3</sub>	15.94	16.70	16.94	16.56	18.83	18.89
Fe <sub>2</sub> O <sub>3</sub>	1.93	2.70	2.82	2.41	2.67	3.02
FeO	3.90	3.48	4.48	4.84	5.60	4.80
MnO	0.11	0.12	0.13	0.13	0.15	0.14
MgO	2.30	2.44	3.15	3.07	4.48	4.47
CaO	4.63	4.70	5.76	5.98	9.77	9.85
Na <sub>2</sub> O	4.52	4.49	4.46	4.46	3.70	3.64
K <sub>2</sub> O	1.86	1.80	1.49	1.47	0.55	0.67
P <sub>2</sub> O <sub>5</sub>	0.22	0.22	0.32	0.28	0.28	0.30
H <sub>2</sub> O <sup>+</sup>	0.18	0.30	0.11	0.15	0.45	0.14
H <sub>2</sub> O <sup>-</sup>	0.29	0.35	0.17	0.20	0.56	0.20
Total	100.69	100.43	100.87	100.68	100.84	99.43
D.I.	6.78	6.35	4.51	4.39	-1.09	-1.07
Rb	34	33	28	28	6	7
Sr	371	383	440	453	682	691
Zr	196	187	178	171	107	98
Ba	548	610	502	500	312	264
Ni	7	15	18	17	20	22
Cr	7	7	25	15	61	53

APPENDIX B. (Continued)

	<u>SS-160</u>	<u>SS-161</u>	<u>SS-189</u>	<u>SS-190</u>	<u>SS-191</u>	<u>SS-244</u>
SiO <sub>2</sub>	52.22	58.70	63.45	63.42	64.08	65.00
TiO <sub>2</sub>	1.33	1.54	1.21	1.21	1.02	0.33
Al <sub>2</sub> O <sub>3</sub>	19.06	16.50	15.79	16.18	16.50	16.06
Fe <sub>2</sub> O <sub>3</sub>	2.84	2.04	1.75	2.20	2.03	2.08
FeO	4.98	5.34	3.86	3.88	3.62	2.99
MnO	0.14	0.13	0.12	0.12	0.11	0.10
MgO	4.42	3.13	1.46	1.67	1.56	1.46
CaO	9.92	6.11	3.92	4.17	3.94	3.86
Na <sub>2</sub> O	3.66	4.51	5.28	5.13	5.19	5.01
K <sub>2</sub> O	0.68	1.46	2.05	1.92	2.06	2.20
P <sub>2</sub> O <sub>5</sub>	0.28	0.29	0.33	0.31	0.31	0.31
H <sub>2</sub> O <sup>+</sup>	0.15	0.56	0.37	0.30	0.17	0.18
H <sub>2</sub> O <sup>-</sup>	0.28	0.48	0.17	0.41	0.32	0.20
Total	99.96	100.79	99.76	100.92	100.91	99.78
D.I.	-1.05	4.11	7.91	7.49	7.94	8.31
Rb	7	28	39	33	40	43
Sr	702	441	362	386	359	344
Zr	97	179	241	217	228	228
Ba	283	491	545	545	552	557
Ni	24	18	10	15	8	9
Cr	68	14	11	11	10	21

## APPENDIX B. (Continued)

Summit Cone Basaltic Andesites (Ps<sub>ba</sub>)

	<u>SS-198</u>	<u>SS-199a</u>	<u>SS-200</u>	<u>SS-201</u>	<u>SS-202</u>	<u>SS-203</u>	<u>SS-204</u>
SiO <sub>2</sub>	54.00	58.08	65.00	55.94	56.71	60.16	58.08
TiO <sub>2</sub>	1.39	1.26	0.85	1.24	1.41	1.33	1.15
Al <sub>2</sub> O <sub>3</sub>	17.44	16.73	16.00	17.72	17.25	15.83	17.20
Fe <sub>2</sub> O <sub>3</sub>	2.45	2.18	2.20	2.73	2.48	2.42	2.11
FeO	6.20	5.39	2.95	5.38	5.21	4.69	5.27
MnO	0.15	0.13	0.09	0.14	0.13	0.13	0.13
MgO	4.36	3.21	1.53	4.20	4.04	2.88	3.51
CaO	8.43	6.68	3.85	8.23	7.64	5.99	6.81
Na <sub>2</sub> O	4.05	4.33	4.93	4.22	4.16	4.68	4.51
K <sub>2</sub> O	0.79	1.57	2.22	0.91	0.97	1.44	1.24
P <sub>2</sub> O <sub>5</sub>	0.21	0.24	0.18	0.27	0.25	0.29	0.25
H <sub>2</sub> O <sup>+</sup>	0.30	0.86	0.71	0.49	0.62	0.83	0.06
H <sub>2</sub> O <sup>-</sup>	0.21	0.15	0.27	0.38	0.26	9.32	0.12
Total	99.98	100.81	100.78	101.85	101.13	100.06	100.44
D.I.	0.42	3.65	8.30	1.05	1.75	4.55	3.10
Rb	5	23	48	13	12	28	22
Sr	506	442	333	523	508	436	474
Zr	106	153	231	145	139	178	163
Ba	252	364	591	309	313	394	338
Ni	40	20	12	35	37	19	21
Cr	67	27	15	54	49	23	36

## APPENDIX B. (Continued)

	<u>Post-glacial Basalts (Ho<sub>bs</sub>)</u>					
	<u>SS-205</u>	<u>SS-206</u>	<u>SS-109</u>	<u>SS-111</u>	<u>SS-186</u>	<u>SS-188</u>
SiO <sub>2</sub>	56.47	56.93	54.81	55.05	54.63	53.75
TiO <sub>2</sub>	1.32	1.22	1.33	1.33	1.52	1.57
Al <sub>2</sub> O <sub>3</sub>	17.75	17.59	16.66	16.47	16.45	16.65
Fe <sub>2</sub> O <sub>3</sub>	2.40	2.67	1.53	2.33	1.49	1.41
FeO	5.21	5.03	6.20	5.58	6.59	6.47
MnO	0.14	0.14	0.14	0.14	0.15	0.14
MgO	4.12	3.94	6.11	5.80	6.18	6.23
CaO	7.40	7.36	7.53	7.64	7.51	7.43
Na <sub>2</sub> O	4.35	4.39	3.53	3.60	3.68	3.67
K <sub>2</sub> O	1.07	1.08	1.08	1.16	1.21	1.17
P <sub>2</sub> O <sub>5</sub>	0.24	0.24	0.26	0.31	0.37	0.32
H <sub>2</sub> O <sup>+</sup>	0.14	0.15	0.59	0.76	0.63	0.52
H <sub>2</sub> O <sup>-</sup>	0.16	0.16	0.18	0.31	0.28	0.12
Total	100.77	100.90	99.95	100.48	100.69	99.43
D.I.	1.92	2.13	0.37	0.59	0.42	0.28
Rb	21	21	21	24	20	21
Sr	497	493	428	413	418	428
Zr	150	159	145	162	155	155
Ba	338	331	342	353	391	389
Ni	40	40	107	103	123	122
Cr	75	73	238	250	226	160

APPENDIX B. (Continued)

	<u>SS-192</u>	<u>SS-207</u>	<u>SS-212</u>	<u>SS-251</u>	<u>SS-252</u>	<u>SS-253</u>
SiO <sub>2</sub>	54.00	54.40	52.10	50.93	51.73	51.73
TiO <sub>2</sub>	1.37	1.36	1.37	1.01	1.15	1.11
Al <sub>2</sub> O <sub>3</sub>	16.95	16.59	17.05	16.32	16.48	16.50
Fe <sub>2</sub> O <sub>3</sub>	2.25	2.43	2.60	2.52	2.80	2.50
FeO	5.67	5.74	5.86	6.12	5.80	6.07
MnO	0.14	0.14	0.15	0.16	0.16	0.16
MgO	5.76	6.08	6.50	8.97	8.83	8.84
CaO	7.68	7.91	9.05	9.77	9.45	9.51
Na <sub>2</sub> O	3.75	3.75	3.55	3.13	3.09	3.15
K <sub>2</sub> O	1.26	1.16	1.04	0.63	0.60	0.62
P <sub>2</sub> O <sub>5</sub>	0.34	0.34	0.33	0.19	0.22	0.21
H <sub>2</sub> O <sup>+</sup>	0.71	0.53	0.52	0.33	0.36	0.32
H <sub>2</sub> O <sup>-</sup>	0.22	0.14	0.19	0.13	0.20	0.22
Total	100.10	100.57	100.31	100.21	100.87	100.94
D.I.	0.50	0.12	-1.31	-3.93	-3.52	-3.55
Rb	27	20	19	11	7	5
Sr	407	432	447	449	449	441
Zr	161	163	161	100	99	101
Ba	342	358	352	211	220	223
Ni	113	123	137	153	158	160
Cr	243	253	308	559	573	587

## APPENDIX B. (Continued)

Early Rhyodacites (Ps<sub>rda</sub>)

	<u>SS-88</u>	<u>SS-90a</u>	<u>SS-91</u>	<u>SS-101</u>	<u>SS-106</u>	<u>SS-132</u>	<u>SS-134</u>	<u>SS-147</u>
SiO <sub>2</sub>	72.36	72.43	72.49	73.60	72.49	72.96	72.59	73.70
TiO <sub>2</sub>	0.35	0.39	0.37	0.35	0.36	0.31	0.30	0.29
Al <sub>2</sub> O <sub>3</sub>	14.79	14.38	14.54	13.99	13.79	14.68	13.42	14.41
Fe <sub>2</sub> O <sub>3</sub>	0.94	1.04	0.80	0.74	0.62	0.95	0.49	0.73
FeO	1.34	1.16	1.39	1.29	1.23	0.99	1.31	1.07
MnO	0.06	0.06	0.06	0.05	0.05	0.05	0.05	0.05
MgO	0.49	0.44	0.47	0.43	0.40	0.22	0.21	0.17
CaO	1.75	1.66	1.77	1.41	1.31	1.38	1.29	1.34
Na <sub>2</sub> O	4.90	4.85	4.77	4.55	4.51	4.64	4.70	4.59
K <sub>2</sub> O	3.00	3.10	3.06	3.21	3.32	3.00	3.12	3.10
P <sub>2</sub> O <sub>5</sub>	0.04	0.03	0.03	0.02	0.09	0.05	0.06	0.05
H <sub>2</sub> O <sup>+</sup>	0.36	0.25	0.36	0.32	0.65	0.99	1.70	0.09
H <sub>2</sub> O <sup>-</sup>	0.15	0.26	0.17	0.19	0.23	0.25	0.24	0.17
Total	100.69	99.46	100.38	100.15	99.05	100.47	99.48	99.76
D.I.	12.26	12.41	12.37	12.86	12.87	12.74	13.18	12.92
Rb	61	61	64	67	72	69	71	72
Sr	206	177	195	183	166	172	173	166
Zr	249	249	250	214	208	217	207	190
Ba	694	694	673	713	730	817	824	828
Ni	6	3	4	1	1	5	5	4
Cr	4	9	6	7	6	10	10	5

APPENDIX B. (Continued)

	<u>SS-148</u>	<u>SS-172</u>	<u>SS-211</u>	<u>SS-216</u>	<u>SS-222</u>	<u>SS-242</u>	<u>SS-248</u>	<u>SS-250</u>
SiO <sub>2</sub>	73.75	71.07	73.03	73.18	72.73	73.79	72.73	73.56
TiO <sub>2</sub>	0.28	0.37	0.31	0.35	0.35	0.30	0.31	0.29
Al <sub>2</sub> O <sub>3</sub>	14.20	14.00	14.19	13.87	14.43	14.06	13.71	13.72
Fe <sub>2</sub> O <sub>3</sub>	0.95	1.48	1.23	0.78	0.62	1.15	0.78	0.71
FeO	0.92	3.69	0.77	1.30	1.46	0.83	1.14	1.17
MnO	0.05	0.06	0.05	0.05	0.05	0.05	0.05	0.05
MgO	0.19	0.36	0.21	0.24	0.29	0.13	0.31	0.30
CaO	1.19	1.45	1.64	1.56	1.55	1.51	1.51	1.54
Na <sub>2</sub> O	4.68	4.89	4.81	4.74	4.79	4.60	4.71	4.71
K <sub>2</sub> O	3.09	3.01	3.15	3.11	3.11	3.05	3.08	3.12
P <sub>2</sub> O <sub>5</sub>	0.05	0.05	0.09	0.06	0.12	0.05	0.04	0.04
H <sub>2</sub> O <sup>+</sup>	0.16	0.33	0.15	0.25	0.35	0.31	1.74	0.35
H <sub>2</sub> O <sup>-</sup>	0.21	0.20	0.18	0.12	0.12	0.44	0.42	0.18
Total	99.27	100.96	99.81	99.61	99.97	100.27	100.53	99.71
D. I.	13.10	12.34	12.70	12.73	12.64	12.88	12.63	12.77
Rb	66	63	69	71	68	79	66	69
Sr	166	202	167	183	186	167	171	169
Zr	185	257	211	234	233	197	219	218
Ba	828	741	718	735	747	700	666	697
Ni	5	4	13	9	9	8	9	8
Cr	5	6	9	8	8	8	10	10

APPENDIX B. (Continued)

1 IS SOUTHERNMOST  
DOME IN S.S.  
CHAIN

	NEWBERRY OBSIDIAN	Post-glacial Rhyodacites (Hordá)						DOME CHAIN 1B	DOME CHAIN 1A
	SS-96	DOME 5 SS-98	DOME 5 SS-99	DOME 5 SS-100	DOME 4 SS-102	DOME 3 SS-103	DOME 2 SS-104	SS-105	SS-107
SiO <sub>2</sub>	72.33	71.86	71.55	72.63	72.30	73.03	72.19	72.53	72.81
TiO <sub>2</sub>	0.44	0.37	0.33	0.37	0.39	0.37	0.35	0.39	0.33
Al <sub>2</sub> O <sub>3</sub>	13.83	14.54	14.54	14.33	14.03	13.84	14.31	13.59	14.21
Fe <sub>2</sub> O <sub>3</sub>	0.69	0.66	0.82	0.87	0.83	0.76	0.88	0.72	0.65
FeO	1.47	1.56	1.44	1.43	1.40	1.49	1.38	1.42	1.48
MnO	0.05	0.05	0.05	0.05	0.06	0.05	0.05	0.05	0.05
MgO	0.55	0.60	0.57	0.52	0.53	0.52	0.45	0.40	0.30
CaO	1.79	1.98	2.02	1.97	1.83	1.82	1.82	1.76	1.66
Na <sub>2</sub> O	4.31	4.48	4.48	4.47	4.49	4.46	4.47	4.46	4.44
K <sub>2</sub> O	3.28	3.07	3.07	3.07	3.07	3.10	3.08	3.09	3.07
P <sub>2</sub> O <sub>5</sub>	0.04	0.03	0.04	0.05	0.09	0.10	0.07	0.07	0.06
H <sub>2</sub> O <sup>+</sup>	0.64	0.36	0.88	0.24	0.40	0.48	0.72	0.76	0.48
H <sub>2</sub> O <sup>-</sup>	0.20	0.15	0.27	0.14	0.40	0.15	0.18	0.26	0.14
Total	99.62	99.71	100.06	100.62	99.82	100.17	99.95	99.50	99.68
D.I.	12.38	12.13	11.91	11.91	12.19	12.21	12.24	12.56	12.53
Rb	76	72	73	74	74	74	77	74	77
Sr	223	231	227	225	228	224	228	229	229
Zr	190	191	190	188	188	189	190	193	188
Ba	691	662	662	683	795	767	795	828	779
Ni	1	4	4	7	5	5	6	8	3
Cr	7	1	4	1	10	9	10	12	11

Sanna magma chamber

APPENDIX B. (Continued)

	Rock mesa	Newberry	DOME CHAIN G	DOME CHAIN G	DOME CHAIN G	DOME CHAIN G	DOME NE OF P.M.	DOME NE OF P.M.
	SS-108b	SS-121	SS-123	SS-124	SS-125	SS-126	SS-223a	SS-223b
SiO <sub>2</sub>	72.52	73.28	72.41	72.88	71.91	72.46	73.09	72.78
TiO <sub>2</sub>	0.32	0.40	0.35	0.37	0.40	0.35	0.32	0.33
Al <sub>2</sub> O <sub>3</sub>	14.25	14.31	14.52	13.74	14.15	13.97	13.68	12.98
Fe <sub>2</sub> O <sub>3</sub>	0.60	0.52	0.81	0.85	0.60	0.71	0.69	0.55
FeO	1.43	1.58	1.39	1.31	1.48	1.44	1.28	1.46
MnO	0.05	0.05	0.06	0.05	0.05	0.06	0.05	0.05
MgO	0.18	0.32	0.43	0.40	0.43	0.34	0.33	0.23
CaO	1.60	1.79	1.74	1.74	1.77	1.81	1.68	1.77
Na <sub>2</sub> O	4.29	4.53	4.51	4.50	4.49	4.50	4.38	4.25
K <sub>2</sub> O	3.35	3.11	2.99	2.99	3.07	3.03	3.31	3.27
P <sub>2</sub> O <sub>5</sub>	0.07	0.12	0.08	0.15	0.12	0.07	0.09	0.17
H <sub>2</sub> O <sup>+</sup>	0.71	0.29	0.48	0.48	0.76	0.69	0.60	1.30
H <sub>2</sub> O <sup>-</sup>	0.11	0.12	0.56	0.31	0.28	0.19	0.16	0.38
Total	99.48	100.42	100.33	99.67	99.06	99.62	99.66	99.52
D. I.	13.02	12.53	12.11	12.36	12.42	12.31	12.74	12.93
Rb	81	75	71	71	72	70	81	79
Sr	198	228	230	230	225	228	198	197
Zr	181	192	194	194	195	193	180	181
Ba	804	758	809	772	820	790	739	689
Ni	4	3	5	5	6	5	9	8
Cr	10	13	10	10	11	11	10	8

Rock mesa and dome NE of Rock mesa  
n=3  
Rb Sr Zr  
x 80.3 197.7 180.7  
s.d. 1.15 0.57 0.57  
c.v. 1% <1% <1%

Dome chain and Newberry flow  
n=14

Rb Sr Zr  
x 73.6 227.5 191.1  
s.d. 2.2 2.4 2.4  
c.v. 2% 1% 1%

## APPENDIX C.

## MINERAL ANALYSES

Individual mineral compositions in lavas from South Sister volcano were determined on an automated ARL-EMX microprobe at the University of Washington, Seattle, Washington. Operating conditions were 15 kv accelerating potential and 15 na sample current, and E. A. Mathez provided assistance. Total iron abundances were determined as ferrous iron (FeO). Analyses have been corrected according to the method of Bence and Albee (1968) with the  $\alpha$ -factors of Albee and Ray (1970). Oxide analyses were recast according to Carmichael (1967).

APPENDIX C. (Continued)

Plagioclase

	<u>154-1,1C</u>	<u>154-1,1R</u>	<u>154-2,1</u>	<u>154-2,2</u>	<u>154-3,1</u>	<u>158-3,1</u>	<u>158-1,2</u>	<u>158-1,3</u>
SiO <sub>2</sub>	54.82	55.38	54.71	52.34	55.14	47.18	47.08	47.94
TiO <sub>2</sub>								
Al <sub>2</sub> O <sub>3</sub>	27.09	26.79	27.22	27.85	26.90	32.58	32.20	31.73
FeO								
MnO								
MgO								
CaO	10.51	10.21	10.34	11.25	10.21	16.54	16.30	15.56
Na <sub>2</sub> O	5.36	5.58	5.51	4.83	5.51	2.01	2.05	2.66
K <sub>2</sub> O	0.20	0.22	0.19	0.14	0.21	0.03	0.04	0.10
Total	97.99	98.18	97.97	96.41	97.97	98.34	97.68	97.99
AN	51.4	49.6	50.4	55.8	50.0	81.9	81.3	75.9
AB	47.4	49.1	48.6	43.3	48.9	17.9	18.6	23.5
OR	1.2	1.3	1.0	0.9	1.1	0.2	0.1	0.6

APPENDIX C. (Continued)

	<u>185-1,1</u>	<u>158-1,2</u>	<u>185-2,1</u>	<u>200-1,1C</u>	<u>200-1,1R</u>	<u>200-4,1</u>	<u>200-4,2</u>	<u>200-4,3</u>
SiO <sub>2</sub>	46.69	47.96	46.69	54.19	56.44	57.27	58.40	57.76
TiO <sub>2</sub>								
Al <sub>2</sub> O <sub>3</sub>	31.85	30.71	32.05	28.33	25.98	25.56	24.25	24.94
FeO								
MnO								
MgO								
CaO	16.31	15.79	15.77	11.49	9.02	9.10	8.00	7.97
Na <sub>2</sub> O	2.14	2.38	2.15	4.94	6.22	6.37	6.72	6.70
K <sub>2</sub> O	0.05	0.05	0.07	0.18	0.29	0.32	0.37	0.37
Total	97.05	96.88	96.73	99.14	97.94	98.62	97.74	97.73
AN	80.6	78.3	79.9	55.7	43.7	43.3	38.8	38.9
AB	19.1	21.4	19.7	43.3	54.6	54.8	59.0	59.1
OR	0.3	0.3	0.4	1.0	1.7	1.9	2.2	2.0

APPENDIX C. (Continued)

	<u>206-1,1C</u>	<u>206-1,1R</u>	<u>206-1,2</u>	<u>206-2,1</u>	<u>206-2,2</u>	<u>206-2,3</u>	<u>109-1,2C</u>	<u>109-1,3C</u>
SiO <sub>2</sub>	54.07	55.30	54.40	54.61	55.20	57.61	54.21	53.68
TiO <sub>2</sub>								
Al <sub>2</sub> O <sub>3</sub>	27.70	26.45	27.02	27.34	26.31	25.24	26.82	28.50
FeO								
MnO								
MgO								
CaO	10.98	10.16	10.48	10.33	10.05	8.08	11.10	10.97
Na <sub>2</sub> O	5.24	5.58	5.43	5.39	5.72	6.70	4.50	5.02
K <sub>2</sub> O	0.20	0.24	0.22	0.21	0.25	0.41	0.55	0.21
Total	98.19	97.72	97.55	97.87	97.52	98.03	97.19	98.37
AN	53.0	49.5	51.0	50.8	48.5	39.0	55.8	54.1
AB	45.8	49.2	47.7	48.0	50.00	58.6	40.9	44.7
OR	1.2	1.3	1.3	1.2	1.5	2.4	3.3	1.2

APPENDIX C. (Continued)

	<u>109-1,3R</u>	<u>109-1,4C</u>	<u>109-1,4R</u>	<u>109-1,5</u>	<u>109-1,6</u>	<u>109-1,7</u>	<u>102-1,1</u>	<u>102-1,2</u>
SiO <sub>2</sub>	49.29	54.74	50.79	50.63	49.65	49.06	57.67	55.27
TiO <sub>2</sub>								
Al <sub>2</sub> O <sub>3</sub>	31.24	27.83	30.10	28.02	30.94	31.42	26.38	27.95
FeO								
MnO								
MgO								
CaO	14.11	10.41	13.33	12.86	13.91	14.25	8.55	10.57
Na <sub>2</sub> O	3.32	5.41	3.72	3.93	3.58	3.24	6.41	5.28
K <sub>2</sub> O	0.11	0.26	0.15	0.18	0.11	0.11	0.34	0.22
Total	98.07	98.65	98.08	95.61	98.19	98.08	99.35	99.29
AN	69.7	50.8	65.8	63.7	67.8	70.4	41.6	51.8
AB	29.7	47.8	33.3	35.2	31.6	29.0	56.5	46.9
OR	0.6	1.4	0.9	1.1	0.6	0.6	1.9	1.3

APPENDIX C. (Continued)

	<u>102-1,3C</u>	<u>102-1,4</u>	<u>102-1,6C</u>	<u>102-1,6R</u>	<u>102-2,1</u>	<u>102-2,2C</u>	<u>102-2,2R</u>	<u>102-3,1C</u>
SiO <sub>2</sub>	57.11	56.85	58.93	58.57	57.96	57.81	57.17	59.28
TiO <sub>2</sub>								
Al <sub>2</sub> O <sub>3</sub>	26.36	26.83	24.50	24.85	25.66	25.60	25.93	24.24
FeO								
MnO								
MgO								
CaO	8.69	8.91	7.62	7.71	8.55	8.40	8.45	7.25
Na <sub>2</sub> O	6.49	6.26	6.89	6.92	6.43	6.57	6.40	7.11
K <sub>2</sub> O	0.30	0.29	0.37	0.37	0.31	0.31	0.30	0.42
Total	98.94	99.14	98.32	98.41	98.91	98.70	98.25	98.29
AN	41.8	43.3	37.1	37.3	41.6	40.6	41.5	35.2
AB	56.5	55.0	60.8	60.6	56.6	57.6	56.7	62.4
OR	1.7	1.7	2.1	2.1	1.8	1.8	1.8	2.4

APPENDIX C. (Continued)

	<u>102-3,1R</u>	<u>102-3,2</u>	<u>102-3,3C</u>	<u>102-3,3R</u>	<u>102-4,1C</u>	<u>102-4,1R</u>	<u>123-1,1C</u>	<u>123-1,1R</u>
SiO <sub>2</sub>	59.46	56.86	57.27	56.95	59.45	57.64	60.08	58.25
TiO <sub>2</sub>								
Al <sub>2</sub> O <sub>3</sub>	24.92	25.46	26.31	25.79	24.17	25.41	24.50	24.71
FeO								
MnO								
MgO								
CaO	7.14	8.97	9.14	8.81	7.04	8.44	6.85	8.16
Na <sub>2</sub> O	7.18	6.32	6.14	6.35	7.27	6.52	7.27	6.40
K <sub>2</sub> O	0.44	0.25	0.29	0.30	0.42	0.30	0.40	0.44
Total	99.14	97.85	99.15	98.19	98.35	98.31	99.11	97.95
AN	34.6	43.4	44.4	42.6	34.0	41.0	33.5	40.3
AB	62.9	55.3	53.9	55.6	63.6	57.3	64.2	57.1
OR	2.5	1.4	1.7	1.8	2.4	1.8	2.3	2.6

APPENDIX C. (Continued)

	<u>123-1,2</u>	<u>123-1,3C</u>	<u>123-1,3R</u>	<u>123-1,4</u>	<u>123-2,1</u>	<u>123-2,2</u>	<u>123-3,1</u>	<u>123-3,2</u>
SiO <sub>2</sub>	56.73	57.55	58.71	57.21	55.35	58.66	57.38	56.68
TiO <sub>2</sub>								
Al <sub>2</sub> O <sub>3</sub>	25.70	25.52	24.42	25.63	27.44	24.86	24.95	26.36
FeO								
MnO								
MgO								
CaO	8.74	8.71	7.25	8.49	10.12	7.54	7.88	9.18
Na <sub>2</sub> O	6.29	6.36	6.82	6.39	5.68	6.62	6.59	6.06
K <sub>2</sub> O	0.28	0.32	0.43	0.31	0.18	0.47	0.27	0.26
Total	97.73	98.46	97.62	98.03	98.77	98.16	97.07	98.55
AN	42.7	42.4	36.1	41.5	49.1	37.5	39.1	44.8
AB	55.7	55.8	61.3	56.7	49.9	59.7	59.3	53.7
OR	1.6	1.8	2.5	1.8	1.0	2.8	1.6	1.5

APPENDIX C. (Continued)

	<u>123-3,3</u>	<u>134-1,1</u>	<u>134-1,2</u>	<u>134-1,3</u>	<u>134-2,1</u>	<u>134-2,2</u>	<u>134-3,1</u>
SiO <sub>2</sub>	59.42	60.23	60.74	60.30	60.51	58.90	61.00
TiO <sub>2</sub>							
Al <sub>2</sub> O <sub>3</sub>	24.06	23.93	24.05	23.60	24.19	24.89	23.96
FeO							
MnO							
MgO							
CaO	7.75	6.19	5.72	6.09	5.83	7.44	5.34
Na <sub>2</sub> O	6.11	7.85	7.98	7.92	7.98	7.11	8.14
K <sub>2</sub> O	0.59	0.45	0.50	0.48	0.45	0.34	0.53
Total	97.94	98.65	98.99	98.39	98.96	98.68	98.96
AN	39.7	29.6	27.5	29.0	28.0	35.9	25.8
AB	56.7	67.9	69.6	68.3	69.4	62.1	71.2
OR	3.6	2.6	2.9	2.8	2.6	2.0	3.0

APPENDIX C. (Continued)

Clinopyroxene

	<u>154-1,1C</u>	<u>154-1,1R</u>	<u>158-3,1</u>	<u>158-1,1C</u>	<u>185-1,1R</u>	<u>185-2,1C</u>
SiO <sub>2</sub>	51.73	51.89	50.19	50.88	50.24	50.23
TiO <sub>2</sub>	0.71	0.36	0.74	0.77	0.77	0.91
Al <sub>2</sub> O <sub>3</sub>	1.80	1.01	3.24	3.28	3.38	2.70
FeO	9.45	13.07	6.95	7.00	6.62	8.42
MnO	0.28	0.50	0.14	0.19	0.16	0.38
MgO	14.16	12.72	15.05	14.97	14.94	14.86
CaO	19.81	18.78	20.91	20.90	21.05	19.86
Na <sub>2</sub> O	0.41	0.47	0.35	0.36	0.38	0.38
K <sub>2</sub> O	0.03	0.04	0.04	0.01	0.03	0.02
Total	98.03	98.82	97.61	98.36	97.56	97.74
EN	42.0	37.9	44.3	44.1	44.2	43.9
FS	15.7	21.9	11.5	11.6	11.0	14.0
WO	42.3	40.2	44.2	44.3	44.8	42.2

APPENDIX C. (Continued)

	<u>158-2,1R</u>	<u>185-2,2</u>	<u>200-1,1</u>	<u>200-1,2</u>	<u>200-2,1C</u>	<u>200-2,1R</u>
SiO <sub>2</sub>	50.94	50.68	50.79	51.06	51.83	51.30
TiO <sub>2</sub>	0.68	0.67	0.73	0.62	0.51	0.38
Al <sub>2</sub> O <sub>3</sub>	3.37	3.31	2.58	2.06	1.38	1.19
FeO	5.59	7.17	9.89	9.98	10.14	11.29
MnO	0.15	0.17	0.37	0.38	0.37	0.45
MgO	15.48	14.94	13.69	13.73	14.13	13.36
CaO	21.42	20.51	19.46	19.85	19.41	19.49
Na <sub>2</sub> O	0.36	0.37	0.43	0.47	0.37	0.40
K <sub>2</sub> O	0.02	0.03	0.03	0.06	0.05	0.06
Total	98.01	97.83	97.97	98.19	98.17	97.89
EN	45.5	44.3	41.2	40.9	41.8	39.7
FS	9.2	11.9	16.7	16.7	16.8	18.7
WO	45.3	43.8	42.1	42.5	41.3	41.6

APPENDIX C. (Continued)

	<u>200-3,1C</u>	<u>200-3,1R</u>	<u>206-1,1C</u>	<u>206-1,1R</u>	<u>206-1,2C</u>	<u>206-1,2R</u>
SiO <sub>2</sub>	51.17	50.94	51.08	51.19	51.34	50.94
TiO <sub>2</sub>	0.64	0.65	0.67	0.66	0.54	0.47
Al <sub>2</sub> O <sub>3</sub>	1.90	1.87	2.32	1.35	1.91	1.59
FeO	9.11	9.83	10.04	12.06	9.68	11.03
MnO	0.29	0.23	0.36	0.34	0.34	0.45
MgO	17.28	15.17	14.34	13.46	14.63	14.01
CaO	17.30	19.18	18.92	18.47	19.44	19.00
Na <sub>2</sub> O	0.41	0.40	0.39	0.41	0.35	0.04
K <sub>2</sub> O	0.04	0.04	0.02	0.04	0.04	0.01
Total	98.13	98.31	98.14	97.98	98.26	97.54
EN	49.6	44.0	42.7	40.2	43.0	41.4
FS	14.7	16.0	16.8	20.2	16.0	18.3
WO	35.7	40.0	40.5	39.6	41.0	40.3

APPENDIX C. (Continued)

Orthopyroxene

	<u>154-2,1C</u>	<u>154-2,1R</u>	<u>154-3,1C</u>	<u>154-3,2C</u>	<u>200-1,1C</u>	<u>200-2,1</u>	<u>200-4,1</u>	<u>102-1,1</u>
SiO <sub>2</sub>	52.68	52.80	53.23	52.74	52.32	51.65	51.86	52.44
TiO <sub>2</sub>	0.41	0.40	0.33	0.42	0.66	0.48	0.32	0.12
Al <sub>2</sub> O <sub>3</sub>	1.13	0.72	0.79	0.99	1.71	0.63	0.67	0.49
FeO	18.16	17.68	18.57	17.78	17.16	24.08	23.29	24.45
MnO	0.42	0.45	0.59	0.47	0.31	0.34	0.87	0.91
MgO	24.16	24.70	24.43	24.42	25.01	20.07	20.86	20.31
CaO	1.80	1.71	1.58	1.83	1.67	1.41	1.47	0.85
Na <sub>2</sub> O	0.06	0.05	0.05	0.06	0.42	0.45	0.03	0.03
K <sub>2</sub> O	0.02	0.03	0.02	0.01	0.02	0.38	0.04	0.06
Total	98.84	98.51	99.59	98.72	99.26	99.49	99.39	99.66
EN	67.8	68.9	67.9	68.4	69.8	58.0	59.6	58.6
FS	28.6	27.7	29.0	27.9	26.9	39.1	37.4	39.6
WO	3.6	3.4	3.1	3.7	3.3	2.9	3.0	1.8

APPENDIX C. (Continued)

	<u>102-2,1</u>	<u>102-3,1C</u>	<u>102-3,1R</u>	<u>123-2,1</u>	<u>123-3,1C</u>	<u>123-3,1R</u>	<u>123-4,1C</u>	<u>123-4,1R</u>
SiO <sub>2</sub>	52.76	52.96	52.22	52.34	51.16	51.61	51.88	52.06
TiO <sub>2</sub>	0.15	0.31	0.19	0.13	0.17	0.19	0.23	0.20
Al <sub>2</sub> O <sub>3</sub>	0.60	0.73	0.94	1.12	0.66	0.84	0.58	0.73
FeO	22.29	22.33	22.25	22.06	22.74	22.66	24.54	22.49
MnO	0.77	0.78	1.02	0.05	0.96	0.77	0.74	0.79
MgO	22.24	22.24	21.89	22.02	20.82	21.48	20.54	21.51
CaO	0.96	0.89	1.07	1.19	1.01	1.02	0.69	1.06
Na <sub>2</sub> O	0.03	0.04	0.02	0.41	0.04	0.04	0.05	0.04
K <sub>2</sub> O	0.02	0.04	0.04	0.25	0.03	0.05	0.03	0.03
Total	99.82	100.31	99.65	99.57	97.57	98.65	99.27	98.91
EN	62.7	62.8	62.3	62.5	60.7	61.5	59.0	61.7
FS	35.3	35.4	35.5	35.1	3.72	36.4	39.6	36.2
WO	2.0	1.8	2.2	2.4	2.1	2.1	1.4	2.1

APPENDIX C. (Continued)

Olivine

	<u>158-1C</u>	<u>158-1R</u>	<u>158-2</u>	<u>185-3C</u>	<u>158-3R</u>	<u>158-4C</u>	<u>158-4R</u>	<u>158-5C</u>	<u>158-6C</u>
SiO <sub>2</sub>	38.33	36.52	38.16	37.77	36.55	37.81	37.82	38.00	38.05
TiO <sub>2</sub>									
Al <sub>2</sub> O <sub>3</sub>									
FeO	21.66	29.40	21.73	21.81	28.07	18.29	18.23	17.29	20.13
MnO									
MgO						41.24	41.38	42.05	39.97
CaO									
Na <sub>2</sub> O									
K <sub>2</sub> O									
Ni	0.01	0.04	0.01	0.03	0.05	0.05	0.07	0.08	0.05
Total	99.10	98.55	98.57	98.16	97.63	97.39	97.50	97.42	98.20
FO	76.3	66.4	76.0	75.9	67.7	80.1	80.2	81.2	78.0
FA	23.7	33.6	24.0	24.1	32.3	19.9	19.8	18.8	22.0

APPENDIX C. (Continued)

	<u>158-6R</u>	<u>206-1C</u>	<u>206-1R</u>	<u>206-2C</u>	<u>206-2R</u>	<u>109-1C</u>	<u>109-3C</u>	<u>109-6C</u>
SiO <sub>2</sub>	35.97	38.45	37.06	37.93	36.36	37.06	37.29	37.18
TiO <sub>2</sub>								
Al <sub>2</sub> O <sub>3</sub>								
FeO	29.91	17.68	26.50	18.24	25.45	22.22	20.58	23.48
MnO								
MgO	31.99	41.39	34.12	41.33	35.26	38.62	39.76	37.03
CaO								
Na <sub>2</sub> O								
K <sub>2</sub> O								
Ni	0.04	0.18	0.11	0.14	0.08	0.06	0.08	0.06
Total	97.91	97.70	97.79	97.64	97.15	97.98	97.73	97.77
FO	65.6	80.7	69.6	80.1	71.2	75.6	77.5	73.8
FA	34.4	19.3	30.4	19.9	28.8	24.4	22.5	26.2

APPENDIX C. (Continued)

	<u>253-1C</u>	<u>253-2C</u>	<u>253-2R</u>	<u>253-3C</u>	<u>253-4C</u>	<u>253-5C</u>	<u>253-6C</u>	<u>253-7C</u>
SiO <sub>2</sub>	38.66	38.99	37.51	39.14	38.98	37.30	38.97	38.54
TiO <sub>2</sub>								
Al <sub>2</sub> O <sub>3</sub>								
FeO	13.21	11.14	18.61	11.21	12.53	18.39	13.34	13.61
MnO								
MgO	45.98	47.79	41.54	47.62	46.10	41.85	45.71	45.70
CaO								
Na <sub>2</sub> O								
K <sub>2</sub> O								
Ni	0.11	0.20	0.08	0.19	0.16	0.07	0.16	0.14
Total	97.99	98.18	97.76	98.21	97.82	97.63	98.22	98.03
FO	86.1	88.4	79.9	88.3	86.8	80.2	85.9	85.7
FA	13.9	11.6	20.1	11.7	13.2	19.8	14.1	14.3

APPENDIX C. (Continued)

Ilmenite

	<u>102-1</u>	<u>102-2</u>	<u>108-1</u>	<u>108-2</u>	<u>108-3</u>	<u>108-4</u>	<u>108-5</u>
SiO <sub>2</sub>	0.46	0.29	0.28	0.23	0.22	0.22	0.22
TiO <sub>2</sub>	42.68	42.63	44.53	43.92	45.10	44.47	44.89
Al <sub>2</sub> O <sub>3</sub>	0.22	0.23	0.45	0.36	0.43	0.54	0.43
FeO	50.66	52.38	49.40	49.76	49.21	49.12	49.00
MnO	0.58	0.63	0.45	0.59	0.54	0.54	0.54
MgO	1.63	1.72	2.73	2.50	2.59	2.91	2.80
CaO	0.05	0.03	0.01	0.01	0.01	0.01	0.01
Na <sub>2</sub> O							
K <sub>2</sub> O							
Total	96.28	97.91	97.85	97.37	98.10	97.81	97.89
HM	17.5	19.6	16.6	17.4	15.6	17.0	16.1
ILM	82.5	80.4	83.4	82.6	84.4	83.0	83.9

APPENDIX C. (Continued)

	<u>Hornblende</u>				<u>Magnetite</u>				
	<u>123-1,1</u>	<u>123-2,1</u>	<u>123-3,1</u>	<u>123-3,2</u>	<u>102-1</u>	<u>102-2</u>	<u>102-3</u>	<u>108-1</u>	<u>108-2</u>
SiO <sub>2</sub>	44.16	43.33	42.92	41.86	0.33	0.27	0.46	0.25	0.24
TiO <sub>2</sub>	1.88	2.70	3.60	2.73	8.63	8.85	8.41	9.57	9.66
Al <sub>2</sub> O <sub>3</sub>	8.90	8.99	9.26	9.19	1.99	1.96	1.86	2.48	2.31
FeO	13.35	14.69	16.72	14.95	81.55	81.99	81.64	82.18	81.68
MnO	0.29	0.35	0.37	0.33	0.47	0.48	0.54	0.22	0.55
MgO	13.39	12.28	10.74	11.88	1.14	1.15	0.87	1.47	1.65
CaO	10.47	10.51	10.35	10.57	0.03	0.05	0.16	0.01	0.01
Na <sub>2</sub> O	2.12	2.40	2.96	2.47					
K <sub>2</sub> O	0.35	0.46	0.54	0.45					
Total	94.89	95.72	97.46	94.42	94.14	94.75	93.94	96.18	96.10
				MT	74.4	74.2	74.5	72.4	72.6
				ULVO	25.6	25.8	25.5	27.6	27.4

## REFERENCES

- Albee, A. L. and Ray, L., 1970. Correction factors for electron probe microanalysis of silicates, oxides, carbonates, phosphates, and sulfates. Anal. Chem., 42, 1408-1414.
- Allegre, C. J. and Minster, J. F., 1978. Quantitative models of trace element behavior in magmatic processes. Earth Planet Sci. Lett., 38, 1-25.
- Allen, J. E. and Beaulieu, J. D., 1976. Plate tectonic structures in Oregon. The Ore Bin, 38(6), 87-99.
- Anderson, A. T., 1976. Magma mixing: petrological process and volcanological tool. J. Volcan. Geotherm. Res., 1, 3-33.
- Anderson, C. A., 1941. Volcanoes of the Medicine Lake Highland, California. Univ. Calif. Pub. Geol. Sci., 25, 347-422.
- Arth, J. G., 1976. Behavior of trace elements during magmatic processes - A summary of theoretical models and their applications. J. Res. U. S. Geol. Surv., 4, 41-47.
- Bacon, C. R. and Duffield, W. A., 1981. Late Cenozoic rhyolites from the Kern Plateau, southern Sierra Nevada, California. Amer. J. Sci., 281, 1-34.
- Baitis, H. W., and Lindstrom, M. M., 1980. Geology, petrography, and petrology of Pinzon Island, Galapagos Archipelago. Contrib. Mineral. Petrol., 72, 367-386.

- Baker, B. H., 1978. A note on the behavior of incompatible trace elements in alkaline magmas. In Newmann, E. R. and Rambert, I. B., eds., Petrology and Geochemistry of Continental Rifts, Dordrecht, Holland, Reidel Pub. Co., 15-25.
- Baker, B. H., Goles, G. G., Leeman, W. P. and Lindstrom, M. M., 1977. Geochemistry and petrogenesis of a basalt-benmoreite-trachyte suite from the southern part of the Gregory Rift, Kenya. Contr. Mineral. Petrol., 64, 303-332.
- Barnes, C. B., 1982. Geology and petrology of the Wooley Creek batholith, Klamath Mountains, northern California. Ph.D. Dissertation, Univ. of Oregon, 214 p.
- Bence, A. E. and Albee, A. D., 1968. Empirical correction factors for the electron microanalysis of silicates and oxides. J. Geology, 76, 382-403.
- Beyer, R. L., 1973. Magma differentiation at Newberry crater in central Oregon. Ph.D. Dissertation, Univ. of Oregon, 84 p.
- Bottinga, Y. and Weill, D. F., 1970. Densities of liquid silicate systems calculated from partial molar volumes of oxide components. Amer. J. Sci., 269, 169-182.
- Bryan, W. B., Finger, L. W. and Chayes, F., 1979. Estimating proportions in petrographic mixing equations by least-squares approximation. Science, 163, 926-927.
- Buddington, A. F. and Lindsley, D. H., 1964. Iron-titanium oxide minerals and synthetic equivalents. J. Petrology, 5, 310-357.
- Burnham, C. W. and Davis, N. F., 1974. The role of H<sub>2</sub>O in silicate melts: II. Thermodynamic and phase relations in the system NaAlSi<sub>3</sub>O<sub>8</sub>-H<sub>2</sub>O to 10 kilobars, 700° to 1100°C. Amer. J. Sci., 274, 902-940.
- Carmichael, I. S. E., 1967. The iron-titanium oxides of salic volcanic rocks and their associated ferromagnesian silicates. Contr. Mineral. Petrol., 14, 36-64.

- Condie, K. C. and Hayslip, D. L., 1975. Young bimodal volcanism at Medicine Lake volcanic center, northern California. Geochim. Cosmochim. Acta, 39, 1165-1178.
- Couch, R., Gemperle, M. and Connard, G., 1978. Total field aeromagnetic anomaly map, Cascade Mountain Range, central Oregon. Oregon Dept. Geol. Min. Ind. Geol. Map Series GMS-9.
- De Paolo, D. J., 1981. Trace element and isotopic effects of combined wallrock assimilation and fractional crystallization. Earth Planet. Sci. Lett., 53, 189-202.
- Eggler, D. H., 1972. Amphibole stability in H<sub>2</sub>O-undersaturated calc-alkaline melts. Earth Planet. Sci. Lett., 15, 28-34.
- Einstein, A., 1906. "Eine neue Bestimmung der Molekuldimensionen." Ann. Phys. (Leipzig), 19, 289-306.
- Evans, B. W. and Frost, B. R., 1975. Chrome-spinel in progressive metamorphism - a preliminary analysis. Geochim. Cosmochim. Acta, 39, 959-972.
- Ewart, A. and Stipp, J. J., 1968. Petrogenesis of the volcanic rocks of the Central North Island, New Zealand, as indicated by a study of Sr<sup>87</sup>/Sr<sup>86</sup> ratios, and Sr, Rb, K, U, and Th abundances. Geochim. Cosmochim. Acta, 32, 699-736.
- Gill, J. B., 1978. Role of trace element partition coefficients in models of andesite genesis. Geochim. Cosmochim. Acta, 42, 709-724.
- Green, T. H., Gree, D. H. and Ringwood, A. E., 1967. The origin of high-alumina basalts and their relationships to quartz tholeiites and alkali basalts. Earth Planet. Sci. Lett., 2, 41-51.
- Hamilton, W. and Myers, W. G., 1966. Cenozoic tectonics of the western United States. Rev. Geophysics, 4, 509-549.
- Hanson, G. N., 1978. The application of trace elements to the petrogenesis of igneous rocks of granitic composition. Earth Planet. Sci. Lett., 38, 26-43.

- Hardee, H. C. and Larson, D. W., 1977. The extraction of heat from magmas based on heat transfer mechanisms. J. Volcan. Geotherm. Res., 2, 113-144.
- Heiken, G. and Eichelberger, J. C., 1980. Eruptions at Chaos Crags, Lassen Volcanic National Park, California. J. Volcanol. Geotherm Res., 7, 443-481.
- Helz, R. T., 1976. Phase relations of basalts in their melting ranges at  $P_{H_2O} = 5 \text{ Kb}$ . Part II. Melt compositions. J. Petrology, 17 139-193.
- Hering, C. W., 1981. Geology and petrology of the Yamsay Mountain complex, south-central Oregon: A study of bimodal volcanism. Ph.D. Dissertation, Univ. of Oregon, 194 p.
- Higgins, M. W., 1973. Petrology of Newberry volcano, central Oregon. Geol. Soc. Amer. Bull., 84, 455-488.
- Hildreth, W., 1979. The Bishop Tuff: Evidence for the origin of compositional zonation in silicic magma chambers. In: Chapin, C. E. and Elston, W. E. (eds.) Ash-Flow Tuffs. Spec. Pap. Geol. Soc. Amer., 180, 43-75.
- Hildreth, W., 1981. Gradients in silicic magma chambers: Implications for lithospheric magmatism. J. Geophys. Res., 86, 10153-10192.
- Holmes, A., 1931. The problem of the association of acid and basic rocks in central complexes. Geol. Mag., 68, 241-255.
- Irvine, T. N. and Baragar, W. R. A., 1971. A guide to the chemical classification of the common volcanic rocks. Can. J. Earth Sci., 8, 523-548.
- Jakes, P. and White, A. J. R., 1972. Major and trace element abundances in volcanic rocks of orogenic areas. Geol. Soc. Amer. Bull., 83, 29-40.
- Jamieson, B. G., 1970. Phase relations in some tholeiitic lavas illustrated by the system  $R_2O_3 - XO - YO - ZO_2$ . Mineralog. Mag., 37, 537-551.

- Johnson, S. H. and Couch, R. W., 1970. Crustal structure in the North Cascade mountains of Washington and British Columbia from seismic reflection measurements. Bull. Seismol. Soc. Amer., 60, 1259-1269.
- Kudo, A. M. and Weill, D. F., 1970. An igneous plagioclase geothermometer. Contr. Mineral. Petr., 25, 52-65.
- Kushiro, I., 1972. Effect of water on the composition of magmas formed at high pressures. J. Petrol., 13, 311-334.
- Kushiro, I., 1974. Melting of hydrous upper mantle and possible generation of andesitic magma: an approach from synthetic systems. Earth Planet Sci. Lett., 22, 294-299.
- Kushiro, I., 1979. Fractional crystallization of basaltic magma. In: Yoder, H. S., ed., The Evolution of the Igneous Rocks, Fiftieth Anniversary Perspectives, Princeton University Press, 171-203.
- Kushiro, I., Shimizu, N., Nakamura, Y., and Akimoto, S., 1972. Compositions of coexisting liquid and solid phases formed upon melting of natural garnet and spinel lherzolites at high pressures: A preliminary report. Earth Planet. Sci. Lett., 14, 19-25.
- Kushiro, I. and Thompson, R. H., 1972. Origin of some abyssal tholeiites from the Mid-Atlantic Ridge. Carnegie Inst. Wash. Yearbook, 71, 403-406.
- Kushiro, I., Yoder, H. S. and Mysen, B. O., 1976. Viscosities of basalt and andesite melts at high pressures. J. Geophys. Res., 81, 6351-6356.
- Lachenbruch, A. H. and Sass, J. H., 1978. Models of an extending lithosphere and heat flow in the Basin and Range province. Geol. Soc. Amer. Mem., 152, 209-250.
- Larson, E. E., 1965. The structure, stratigraphy, and paleomagnetism of the Plush area, southeastern Lake County, Oregon. Ph. D. Dissertation, Univ. of Colorado, 166 p.

- Lawrence, R. D., 1976. Strike-slip faulting terminates the Basin and Range province in Oregon. Geol. Soc. Amer. Bull., 87, 846-850.
- Luhr, J. F. and Carmichael, I. S. E., 1980. The Colima volcanic complex, Mexico. Contrib. Mineral. Petrol., 71, 343-372.
- MacLeod, N. S., Sherrod, D. R., Chitwood, L. S. and McKee, E. H., 1981. Newberry volcano, Oregon. U. S. Geol. Surv. Circular 838, 85-103.
- Martin, R. F. and Piwinski, A. J., 1972. Magmatism and tectonic settings. J. Geophys. Res., 77, 4966-4976.
- McBirney, A. R., 1968. Petrochemistry of the Cascade andesite volcanoes. Oregon Dept. Geol. Min. Ind. Bull., 62, 101-107.
- McBirney, A. R., 1978. Volcanic evolution of the Cascade range. Ann. Rev. Earth Planet. Sci., 6, 437-456.
- McBirney, A. R., 1979. Effects of assimilation. In: Yoder, H. S., ed., The Evolution of the Igneous Rocks, Fiftieth Anniversary Perspectives, Princeton University Press, 307-338.
- McBirney, A. R., 1980. Mixing and unmixing of magmas. J. Volcan. Geotherm. Res., 7, 357-371.
- McBirney, A. R. and Noyes, R. M., 1979. Crystallization and layering of the Skaergaard Intrusion. J. Petrol. 20 (3), 487-554.
- Mertzman, S. A., Jr., 1977. The petrology and geochemistry of the Medicine Lake volcano, California. Contrib. Mineral. Petrol., 62, 221-247.
- Mertzman, S. A. and Williams, R. J., 1981. Genesis of Recent silicic magmatism in the Medicine Lake Highland, California: evidence from cognate inclusions found at Little Glass Mountain. Geochim. Cosmochim. Acta, 45, 1463-1478.
- Murase, T. and McBirney, A. R., 1973. Properties of some common igneous rocks and their melts at high temperatures. Bull. Geol. Soc. Amer., 84, 3563-3592.

- Myers, D. J. and Marsh, B. D., 1981. Geology and petrogenesis of the Edgcumbe volcanic field, SE Alaska: The interaction of basalt and sialic crust. Contrib. Mineral. Petrol., 77, 272-287.
- Mysen, B. O. and Boettcher, A. L., 1975. Melting of a hydrous mantle: II, Geochemistry of crystals and liquids formed by anatexis of mantle peridotite at high pressures and high temperatures as a function of controlled activities of water, hydrogen and carbon dioxide. J. Petrol., 16, 549-600.
- Norrish, K. and Hutton, J. T., 1969. An accurate X-ray spectrographic method for the analysis of a wide range of geologic samples. Geochim. Cosmochim. Acta, 33, 431-454.
- O'Hara, M. J., 1976. Data reduction and projection schemes for complex compositions. Natural Environ. Res. Council Pub., Series D, No. 6, 103-126.
- O'Hara, M. J., 1977. Geochemical evolution during fractional crystallization of a periodically re-filled magma chamber. Nature, 266, 503-507.
- Osborn, E. F., 1959. Role of oxygen pressure in the crystallization and differentiation of basaltic magma. Amer. J. Sci., 257, 609-647.
- Pearce, J. A. and Norry, M. J., 1979. Petrogenetic implications of Ti, Zr, Y, and Nb variations in volcanic rocks. Contrib. Mineral. Petrol., 69, 33-47.
- Pease, R. W., 1969. Normal faulting and lateral shear in northeastern California. Geol. Soc. Amer. Bull., 80, 715-720.
- Peck, D. L., Griggs, A. B., Schlicker, H. G., Wells, F. G. and Dole, H. M., 1964. Geology of the central and northern parts of the Western Cascade range in Oregon. U. S. Geol. Surv. Prof. Pap. 449, 56 p.
- Philpotts, A. R., 1976. Silicate liquid immiscibility: Its probable extent and petrogenetic significance. Amer. J. Sci., 276, 1147-1177.

- Pitts, A. and Couch, R., 1978. Complete Bouguer gravity anomaly map, Cascade Mountain Range, central Oregon. Oregon Dept. Geol. Min. Ind. Geol. Map. Series, GMS-8.
- Ritchey, J. L., 1979. Origin of divergent magmas at Crater Lake, Oregon. Ph.D. Thesis, University of Oregon, 209 p.
- Ritchey, J. L., 1980. Divergent magmas at Crater Lake, Oregon: Products of fractional crystallization and vertical zonation in a shallow, water-under-saturated chamber. J. Volcan. Geotherm. Res., 7, 373-386.
- Robyn, T. L., 1977. Geology and petrology of the Strawberry volcanics, NE Oregon, Ph.D. Dissertaion, Univ. of Oregon, 197 p.
- Roeder, P. L. and Emslie, R. F., 1970. Olivine-liquid equilibrium, Contr. Mineral. Petrol., 29, 275-289.
- Rohsenow, W. M. and Choi, H. Y., 1961. Heat, Mass and Momentum Transfer., Prentice-Hall, New Jersey, 537 p.
- Ryerson, F. J. and Hess, P. C. 1978. Implications of liquid-liquid distribution coefficients to mineral-liquid partitioning. Geochim. Cosmochim. Acta, 42 (A6), 921-932.
- Shaw, H. R., 1972. Viscosities of magmatic silicate liquids: an empirical method of prediction. Amer. J. Sci., 272, 870-893.
- Sigurdsson, H., 1968, Petrology of acid xenoliths from Surtsey. Geol. Mag., 105, 440-453.
- Sigurdsson, H., 1977. Generation of Icelandic rhyolites by melting of plagiogranites in the oceanic layer. Nature, 269, 25-28.
- Skelland, A. H. P., 1974. Diffusional Mass Transfer. John Wiley, New York, 510 p.
- Smith, A. L. and Carmichael, I. S. E., 1968. Quaternary lavas from the southern Cascades, western U. S. A. Contrib. Mineral. Petrol., 19, 212-238.

- Smith, R. L., 1979. Ash-flow magmatism. Geol. Soc. Amer. Spec. Pap. 180, 5-28.
- Spera, F. J. and Crisp, J. A., 1981. Eruption volume, periodicity, and caldera area: Relationships and inferences on development of compositional zonation in silicic magma chambers. J. Volcanol. Geotherm. Res., 11, 169-187.
- Steinborn, T. L., 1972. Trace element geochemistry of several volcanic centers in the High Cascades. M. S. Thesis, Univ. of Oregon.
- Stewart, J. H., 1978. Basin-range structure in western North America: A review. Geol. Soc. Amer. Spec. Pap. 152, 1-31.
- Taylor, E. M., 1978. Field geology of S. W. Broken Top quadrangle, Oregon. Oregon Dept. Geol. Min. Ind. Spec. Pap. 2, 50 p.
- Thayer, T. P., 1937. Petrology of later Tertiary and Quaternary rocks of the north-central Cascade Mountains in Oregon, with notes on similar rocks in western Nevada. Geol. Soc. Amer. Bull. , 48, 1161-1652.
- Treuil, M., 1973. Criteres petrologiques, geochemique, et structuraux de la genese et de la differenciation des magmas basaltique: exemples de l'Afar, These, Orleans.
- Treuil, M. and Joron, J. M., 1975. Utilisation des elements hygromagmatophiles pour la simplifacation de la modelisation quantitative des processus magmatiques: exemples de l'Afar, et de la dorsade medioatlantique. Soc. It. Mineral. Petrol., 31, 125.
- Waters, A. C., 1962. Basalt magma types and their tectonic associations: Pacific Northwest of the United States. In The Crust of the Pacific Basin, Amer. Geophys. Mon. No. 6, 158-170.
- Watson, E. B., 1976. Two liquid partition coefficients: experimental data and geochemical implications. Contrib. Mineral. Petrol., 56, 119-134.

- Watson, E. G., 1979. Zircon saturation in felsic liquids: Experimental results and application to trace element geochemistry. Contrib. Mineral. Petrol., 70, 407-419.
- Weaver, D. S., Seal, J. S. C. and Gibson, I. L., 1972. Trace element data relevant to the origin of trachytic and pantelleritic lavas in the East African Rift system. Contrib. Mineral. Petrol., 36, 181-194.
- Wells, P. R. A., 1977. Pyroxene thermometry in simple and complex systems. Contr. Mineral. Petrol., 62, 129-139.
- Wells, R. E., 1975. The geology of the Drake Peak rhyolite complex and the surrounding area, Lake County, Oregon. M. S. Thesis, Univ. of Oregon, 130 p.
- White, C. M., 1980a. Geology and geochemistry of volcanic rocks in the Detroit area, Western Cascade Range, Oregon. Ph.D. Dissertation, Univ. of Oregon, 178 p.
- White, C. M., 1980b. Geology and geochemistry of Mt. Hood volcano. Oregon Dept. Geol. and Min. Ind. Spec. Paper #8, 26 p.
- White, C. M. and McBirney, A. R., 1979. Some quantitative aspects of orogenic volcanism in the Oregon Cascades. Geol. Soc. Amer. Mem. 152, 369-388.
- Wilcox, R. E., 1954. Petrology of Paricutin volcano, Mexico. U. S. Geol. Surv. Bull., 965C, 281-353.
- Williams, H., 1942. The geology of Crater Lake National Park, Oregon. Carnegie Inst. Wash. Pub., 540, 162 p.
- Williams, H., 1944. Volcanoes of the Three Sisters region, Oregon, Cascades. Univ. of Calif. Dept. Geol. Sci. Bull., 27(3), 37-84.
- Williams, R. J., 1971. Reaction constants in the system FeO - MgO - SiO<sub>2</sub> - O<sub>2</sub> at 1 atm. between 900° and 1300°C: Experimental results. Amer. J. Sci., 270, 334-360.

- Wright, T. L. and Doherty, P. C., 1970. A linear programming and least squares computer method for solving petrologic mixing problems. Geol. Soc. Amer. Bull., 81, 1995-2008.
- Yoder, H. S., Jr., 1969. Calc-alkalic andesites: Experimental data bearing on the origin of their assumed characteristics. Oregon Dept. Geol. Min. Ind. Bull., 65, 77-89.
- Yoder, H. S., Jr., 1973. Contemporaneous basaltic and rhyolitic magmas. Amer. Mineral., 58, 153-171.
- Yoder, H. S., Jr. and Tilley, C. E., 1962. Origin of basalt magmas: An experimental study of natural and synthetic rock systems. J. Petrol., 3(3), 342-532.